1-30-2017 12:00 AM

Aerodynamic Optimization and Wind Load Evaluation Framework for Tall Buildings

Ahmed Elshaer, *The University of Western Ontario*

Supervisor: Dr. Girma Bitsuamlak, *The University of Western Ontario*
Joint Supervisor: Dr. Ashraf El Damatty, *The University of Western Ontario*
A thesis submitted in partial fulfillment of the requirements for the Doctor of Philosophy degree in Civil and Environmental Engineering

Abstract

Wind is the governing load case for majority of tall buildings, thus requiring a wind responsive design approach to control and assess wind-induced loads and responses. The building shape is one of the main parameters that affects the aerodynamics that creates a unique opportunity to control the wind load and consequently building cost without affecting the structural elements. Therefore, aerodynamic mitigation has triggered many researchers to investigate various building shapes that can be categorized into local (e.g. corners) and global mitigations (e.g. twisting). Majority of previous studies compare different types of mitigations based on a single set of dimensions for each mitigation types. However, each mitigation can produce a wide range of aerodynamic performances by changing the dimensions. Thus, the first objective of this thesis is developing an aerodynamic optimization procedure (AOP) to reduce the wind load by coupling Genetic Algorithm, Computational Fluid Dynamics (CFD) and an Artificial Neural Network surrogate model. The proposed procedure is adopted to optimize building corners (i.e. local) using three-dimensional CFD simulations of a two-dimensional turbulent flow. The AOP is then extended to examine global mitigations (i.e. twisting and opening) by conducting CFD simulations of three dimensional turbulent wind flow. The procedure is examined in single- and multi-objective optimization problems by comparing the aerodynamic performance of optimal shapes to less optimal ones. The second objective is to develop accurate numerical wind load evaluation model to validate the performance of the optimized shapes. This is primarily achieved through the development of a robust inflow generation technique, called the Consistent Discrete Random Flow Generation (CDRFG). The technique is capable of generating a flow field that matches the target velocity and turbulence profiles in addition to, maintaining the coherency and the continuity of the flow. The technique is validated for a standalone building and for a building located at a city center by comparing the wind pressure distributions and building responses with experimental results (wind tunnel tests). In general, the research accomplished in this thesis provides an advancement in numerical climate responsive design techniques, which enhances the resiliency and sustainability of the urban built environment.

Keywords

Tall building, Wind Load, Optimization, Computational Fluid Dynamics (CFD), Large Eddy Simulation (LES), Building Vibration, Turbulence, Aerodynamics, Genetic Algorithm, Artificial Neural Networks, Numerical Technique, Atmospheric boundary layer (ABL), Wind Spectra, Wind profile, Turbulent Intensity, Length Scales, Coherency, Peak Factor, Gust Factor, Dynamic Response.

Co-Authorship Statement

This thesis has been prepared in accordance with the regulations for an Integrated-Article format thesis stipulated by the Faculty of Graduate Studies at Western University and has been co-authored as:

Chapter 2: Consistent inflow turbulent generator for LES evaluation of wind-induced responses for tall buildings

Development and application of the numerical simulations in this chapter was conducted by A. Elshaer under close supervision of Dr. H. Aboshosha, Dr. G. Bitsuamlak and Dr. A. El Damatty. A. Elshaer conducted all the CFD modelling and developed the analytical integration of the inflow generation technique with the CFD solver. The development of the inflow technique and was resulted from the collaboration of all the authors. A paper co-authored by H. Aboshosha, A. Elshaer, G. Bitsuamlak and A. El Damatty is published at (Journal of Wind Engineering and Industrial Aerodynamics. 142, 198-216).

Chapter 3: LES evaluation of wind-induced responses for an isolated and a surrounded tall building

Development and application of the numerical simulations in this chapter was conducted by A. Elshaer and under close supervision of Dr. H. Aboshosha, Dr. G. Bitsuamlak and Dr. A. El Damatty. A. Elshaer conducted all the CFD analyses and performed the validation with the experimental results, and in collaboration with Dr A. Dagnew. The comparison between different study cases was a collaborative work between all the authors. A paper co-authored by A. Elshaer, H. Aboshosha, G. Bitsuamlak and A. El Damatty, A. Dagnew was publish at (Engineering Structures Journal115, 179-195).

Chapter 4: Enhancing wind performance of tall buildings using corner aerodynamic optimization

Development and application of the numerical simulations in this chapter was conducted by A. Elshaer under close supervision of Dr. G. Bitsuamlak and Dr. A. El Damatty. A paper co-authored by A. Elshaer, G. Bitsuamlak and A. El Damatty was submitted to (Engineering structures journal, accepted).

Chapter 5: Aerodynamic shape optimization of tall buildings using twisting and corner modifications

Development and application of the numerical simulations in this chapter was conducted by A. Elshaer under close supervision of Dr. G. Bitsuamlak and Dr. A. El Damatty. A paper co-authored by A. Elshaer, G. Bitsuamlak and A. El Damatty was published at (8th International Colloquium on Bluff Body Aerodynamics and Applications, Boston, USA).

Chapter 6: Multi-objective optimization of tall building vents for wind-induced loads reduction

Development and application of the numerical simulations in this chapter was conducted by A. Elshaer under close supervision of Dr. G. Bitsuamlak and Dr. A. El Damatty. A paper co-authored by A. Elshaer, G. Bitsuamlak and A. El Damatty was submitted to (ASCE, Journal of Structural Engineering).

Acknowledgments

As modest as this work is, I can't be grateful enough to Allah (the almighty) for his countless blessings. I pray that he accepts me to serve him and to be a true follower of Prophet Mohammed who taught us to strive for knowledge, peace and helping others by telling us: "Allah is helping the servant as long as the servant is helping his brother".

I would like to express my unlimited gratitude to Dr. Girma Bitsuamlak. He was like an elder brother or a friend during this enjoyable doctoral journey. His continuing inspiration to me and my colleagues and his amazing effort to secure the best possible working environment are really admirable. Personally, I learned a lot from him not only academically but socially as well.

I am very grateful to Dr. Ashraf El Damatty for his confidence in me and his continuous support. I always try to learn from him how to build a clear vision in research and life, and to exert the ultimate effort to achieve goals. I wish one day to reach a similar success in academic life and solid scientific background.

From the deep of my heart, I would like to thank my true life mentors and the greatest parents ever "Yasser" and "Lamyaa". Many thanks to my wonderful and faithful wife "Maryam"; and my beloved daughters "Mawadda" and "Rokaya" for filling my life with great happiness and for their great sacrifices and care. I remember seeing Mawadda's first picture after 10 days from arriving Canada, and now she is a little girl who can hold my PhD thesis in her hands. Many thanks to my whole family with a special thanks to the best brother "Ammar", the most wonderful sister "Alaa", my loving grandparents "Salwa" and "Khalaf", my dear parents-in-law "Hassan" and "Dalia", and my brother-in-law "Ali". I would like to acknowledge my delightful aunt "Prof. Randa" who always has been my academic mentor and the backbone of academic career. I am also so thankful to my greatest teacher "Dr. Ali Haseeb" and my M.Sc. supervisors "Prof. Hatem Moustafa" and "Prof. Hamed Hadhoud".

Many thanks go to Western and everybody at Western engineering. You are the unsung heroes of this educational process. Special thanks to Dr. Haitham Aboshosha for being a sincere friend and a valuable collaborator. My deep gratitude goes to research group colleagues (Zoheb, Tibebu, Anwar, Meseret, A. Elatar, Anant, Matiyas Barilelo, Kimberley, Abiy, M. Delavar, Christopher), my friends at Western (M. Abosharkh, A. Musa, A. Abdel Kader, A. Ibrahim, A. El Ansary, M. Aboutabikh, I. Ibrahim, M. Ajan Elhadid, O. Elhawary, A. Hegazy, A. Hamade, A. Hamada, M. Hamada, A. Elawady, M. Mansour, Abdo, A. Shehata, F. Elezaby, Safwat, M. Elsawy, M. Kasem, M. Askar) and my old friends from Egypt (M. Abogalila, A. Abdelaziz, M. Karam, I. Ehab, E. Mahmoud, M. Elhayawan, O. Ehab, Mohamed Ali, M. Yassin, Mahmoud Ali, Ahmed Sayed, Amr Sayed). You have all contributed greatly to my life and to this work and I will always remember you fondly.

Finally, I would like to dedicate this work to the memory of my grandparents "Lotfy" and "Samira", uncle "Sayed Riad", aunt "Mona Abdlhady", my friends (M. Abdulzaher, A. Abdelaziz, I. Khafagy), and all the innocent people who died due to the absence of justice.

Table of Contents

List of Tables

List of Figures

Chapter 1

1 Introduction

1.1 Background

New generations of tall buildings are becoming increasingly taller, flexible and slender primarily driven by novel developments in design methods and new construction materials and techniques. This in turn makes tall buildings more sensitive to lateral loads such as wind. In addition, there is a need to lower the building weight in order to decrease the gravity loads to control the inertial forces developed by earthquake. This further contributes to an increase in the wind-induced forces and motions. As a result, wind-induced loads and motions typically govern the design of the lateral load resisting systems in tall buildings. The outer shape of the building is one of the main parameters that affect these loads and responses. The dependence of the wind load on the building shape makes the generalizations of wind load for tall buildings almost impossible, because every complex shape and surroundings produce a unique set of design wind loads. On the other hand, this dependency on the shape provides a unique opportunity to reduce the wind load through outer shape modifications.

In general, controlling wind-induced loads and vibrations can be achieved through three approaches that include: (1) utilizing sufficient structural components and external damping systems, (2) introducing aerodynamic mitigations for the outer shape of a building, or (3) combining the previous two approaches by improving both structural components and aerodynamic performances of the building. The first approach sacrifices additional resources (e.g. higher strength for structural elements and damping systems) to avoid changing the building outer shape. The second approach saves these expenses by reducing the applied wind load through aerodynamic mitigation. It should be noted that, in many cases, meeting the strength and serviceability requirements cannot be satisfied unless both structural and aerodynamic improvements (third approach) are used. For this reason, almost all recently built super tall buildings have applied aerodynamic mitigations either locally (at the corner shapes) or globally (along the height of the building). Many researchers have reported that careful modification of the shape of the corners can provide better aerodynamic performance (Kwok 1988, Kareem et al. 1999, Tamura and Miyagi 1999, Carassale et al. 2014). "Local Shape Mitigation" of tall buildings focuses on the change of the corner shapes to enhance the aerodynamic performance (Figure 1-1). The main advantage of this type of mitigation is that the effect on the architectural and structural concept of the structure is limited. Detailed literature on "Local Shape Mitigation" is provided in Chapter 4 of this thesis. In contrast, "Global Shape Mitigation" has a considerable effect on the architectural and structural design because the mitigations affect the whole height and width of the building (e.g. twisting, tapering and opening) rather than being localized at the corners (Figure 1-2). This scale of mitigation can enhance the aerodynamic performance because a wider variety of changes is applied. "Global Shape Mitigation" is further discussed in Chapters 5 and 6 of this thesis.

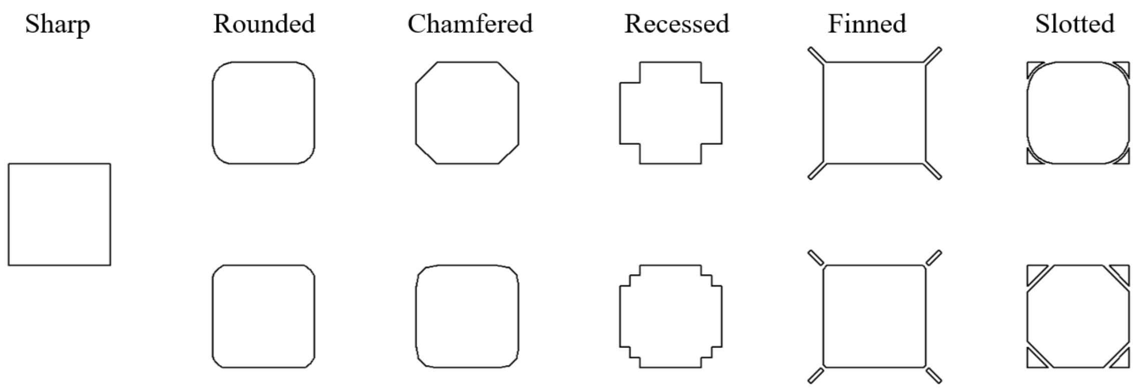

Figure 1-1 Examples of tall building local (corner) mitigations

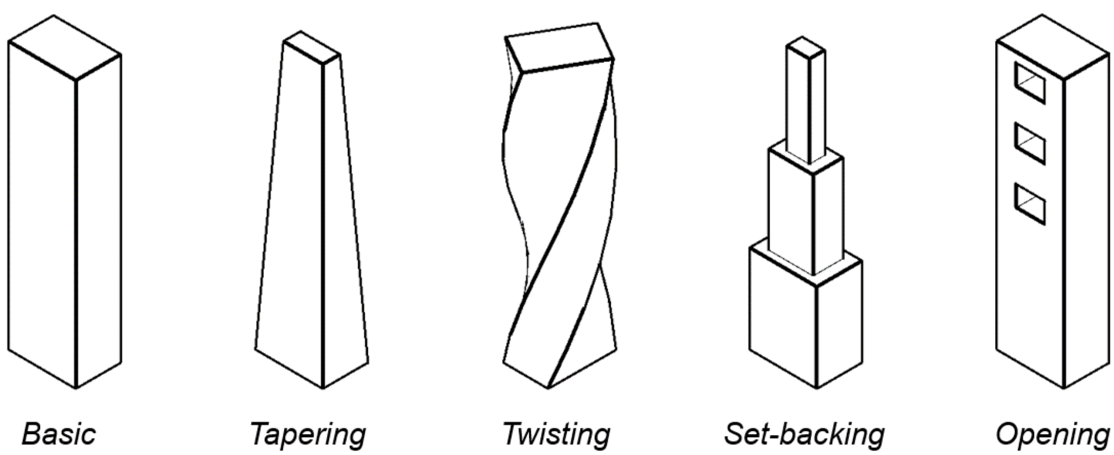

Figure 1-2 Examples of tall buildings global mitigations

It can be noticed that many previous studies compared different types of mitigations based on a single set of dimensions for each mitigation family. However, each family (of a specific shape mitigation) can produce a wide range of aerodynamic performances based on the selection of a different combination of mitigation dimensions. Consequently, a wider search space (i.e. more building shape alternatives) can be explored by integrating an optimization algorithm to the aerodynamic assessment procedure (Kareem et al. 2013).

Kareem et al. (2013a, b and 2014) introduced an approach for tall building corner optimization to reduce drag and lift by adopting two-dimensional CFD models. This approach is useful to overcome the computational cost associated with the iterative procedure required for optimization. Bernardini et al. 2015 investigated the efficiency of utilizing Kriging model as a surrogate model for the objective function evaluation. The utilization of a surrogate model reduced the computational time. In these studies, Unsteady Reynolds-Averaged Navier–Stokes (URANS) equations were used. Although these studies developed a very promising and useful approach for building aerodynamic optimizations, some limitations are observed. For example, (i) wind directionality effect is not considered, (ii) low-order CFD models are used to evaluate shape alternatives, although wind performance assessment usually requires the use of high accuracy CFD- or BLWT-based evaluations (iii) only two-dimensional flow was used to assess various cross-sections. Using these novel approaches, it is possible to infer the relative performance of the various geometric alternatives (i.e. comparing alternatives) adopting the reduced order 2D simulations. A similar conclusion was also reported by Tamura and Miyagi 1999. Thus, adopting a simplified low order simulation can significantly reduce the analysis accuracy that may affect the conclusions observed under such simplified scenarios. Particularly when simulating the turbulent atmospheric boundary layer (ABL) flow and its interaction with a tall building. These complex interactions can be realistically captured through LES as reported by Nozawa and Tamura (2002), Dagnew and Bitsuamlak (2013 and 2014).

It is to be noted that the accuracy of LES depends on the proper selection of the inflow boundary conditions (Davenport 1993; Tamura 2010a, b; Tominaga et al. 2008). According to the Keating et al. (2004) inflow boundary condition (IBC) can be generated using three methods (i) precursor database (Bitsuamlak and Simiu 2010, Liu and Pletcher 2006), (ii) recycling method (Lund et al. 1998; Nozawa and Tamura 2002, Aboshosha et al. 2015), and (iii) synthesizing the turbulence (Kondo et al. 1997; Huang et al. 2010; Smirnov et al. 2001). The first two methods require prior simulations to generate the inflow which can be computationally expensive compared to the synthesizing the turbulence method. Huang et al. (2010) suggested the discrete random flow generation (DRFG) method to produce turbulent velocity field that has turbulent spectra close to the target ABL flow characteristics that forms also the basis for current study. Castro et al. (2011) proposed a modification to the DRFG method to obtain velocity field that had a better match with the target spectra. Generally, the DRFG method is able to generate turbulent spectra that is close to the target, maintain the spatial correlation among the resulting velocities, and can easily be implemented in parallel computing environment. However, there are other additional important conditions that needs to be satisfied by the generated inflow for wind engineering applications such as maintaining the continuity equation and the proper coherence among the velocities (Davenport 1993). This include maintaining proper correlations among the turbulent velocities within different frequencies as indicated by Davenport (1993) and Kijewski and Kareem (1998). Another important condition is modeling the turbulent spectra to be exactly similar as the target flow. A further detailed review about inflow generation techniques is presented in Chapter 2 of this thesis.

1.2 Research Gap

As discussed earlier, a significant improvement in the aerodynamic performance can be achieved by modifying the outer shape of a tall building. Majority of previous studies compare shape alternatives based on one geometry for each mitigation family leading to an ad hoc solution rather than an optimal solution. Thus, for further aerodynamic improvement, the aerodynamic assessment method (i.e. Wind Tunnel or CFD) needs to be coupled with an optimization technique. This will result in exploring wider search space (examining more building shapes) and introducing an automated technique that converges towards the optimal building shape. It is also required that the optimization process to be computationally affordable to overcome the computationally expensive CFD analyses without affecting the accuracy of the numerical modelling. Finally, since the accuracy of the CFD analysis depends on the proper matching to the target inflow profiles and statistics, a more accurate inflow technique needs to be developed that satisfy the coherency among velocities and the continuity equation (i.e. diversion-free).

1.3 Scope of Thesis

The thesis aims to address the research gaps mentioned in the above section. As such, the objectives of the thesis are:

1. Developing an aerodynamic optimization procedure that is capable of identifying the optimal building shape for a selected mitigation type.

2. Examining the proposed optimization procedure for “Local Shape Mitigations” and “Global Shape Mitigations”.

3. Adopting the proposed optimization procedure to conduct single-objective and multi-objective optimization problems.

4. Developing accurate numerical models to evaluate wind loads though LES and novel inflow generation technique that satisfy the target velocity and turbulence profiles in addition to other flow statistics such as coherency and continuity.

5. Validating the numerical wind load evaluation using experimental work from wind tunnel test and other numerical studies.

1.4 Organization of thesis

This thesis has been prepared in an “Integrated-Article” format. In Chapter 1, a review of the studies and approaches related to aerodynamic mitigations and wind load evaluation using CFD is provided. These objectives are addressed in detail in the following five chapters.

1.4.1 Consistent inflow turbulent generator for LES evaluation of wind-induced responses for tall buildings

This chapter discusses a new turbulent inflow generator technique that can be used as inflow boundary condition for LES based on synthesizing random divergent-free turbulent velocities. The accuracy of the proposed technique to produce turbulent velocities with proper spectra and coherency function is assessed in comparison with typical ABL flow characteristics obtained from literature. Further, its appropriateness to evaluate wind-induced response for tall building is assessed by employing the proposed technique as inlet boundary condition for LES of the ABL flow around a typical tall building that was previously tested in a boundary layer wind tunnel.

1.4.2 LES evaluation of wind-induced responses for an isolated and a surrounded tall building

In this chapter, the aerodynamic response of a standard tall building (commonly known as the CAARC model) is investigated using LES. The LES employs the Consistent Discrete Random Flow Generation (CDRFG) technique to generate the inflow boundary condition. The building aerodynamic behavior is investigated for two configurations (an isolated building and a building with complex surrounding buildings) and the results are compared with a previous wind tunnel test.

1.4.3 Enhancing wind performance of tall buildings using corner aerodynamic optimization

This chapter presents building corner aerodynamic optimization procedure (AOP) to reduce the wind load, by coupling an optimization algorithm, Large Eddy Simulation (LES) and an artificial neural network (ANN) based surrogate model. Two aerodynamic optimization examples focusing on drag and lift minimization that consider wind directionality and turbulence are presented. Since this study focuses on “Local Shape

Mitigations", two-dimensional inflow is utilized in examining different building cross-sections. The aerodynamic performance of optimal shapes is compared to other near optimal shapes to elaborate the improvement achieved throughout the optimization process.

1.4.4 Aerodynamic shape optimization of tall buildings using twisting and corner modifications

In this chapter, improving the aerodynamic performance of tall buildings is conducted by adopting the AOP to reduce the along-wind base moment by helical twisting and corner modifications of a tall building. Three-dimensional LES of a synoptic inflow is used to assess different shape alternatives during the optimization process.

1.4.5 Multi-objective optimization of tall building vents for wind-induced loads reduction

This chapter discusses the utilization of the AOP to conduct multi-objective optimization problem (considering more than one objective function) by optimizing the introduction of three openings to a standard tall building named the Commonwealth Advisory Aeronautical Research Council (CAARC). The optimization process aims to reduce both wind-induced base moments by changing the aspect ratio of the openings and the distances between successive openings.

1.5 References

Aboshosha H, Bitsuamlak G, El Damatty A. LES of ABL flow in the built-environment using roughness modeled by fractal surfaces. Sustainable Cities and Societies 2015; 19, 46-60.

Bernardini E, Spence S, Wei D, Kareem A. Aerodynamic shape optimization of civil structures: A CFD-enabled Kriging-based approach, Journal of Wind Engineering and Industrial Aerodynamics 2015; 144, 154-164.

Bitsuamlak GT, Simiu E. CFD's potential applications: wind engineering perspective. The fifth International Symposium on Computational Wind Engineering 2010; Chapel hill, NC.

Carassale L, Freda A, Marrè-Brunenghi M. Experimental investigation on the aerodynamic behavior of square cylinders with rounded corners. Journal of Fluids and Structures 2014; 44, 195-204.

Castro, G.H., Paz, R.R., Sonzogni, V.E. 2011. Generation of turbulent inlet velocity conditions for large eddy simulations. Mecánica Computacional, 2275-2288.

Dagnew A, Bitsuamlak GT. Computational evaluation of wind loads on buildings: a review, Wind and Structures 2013; 16(6), 629-660.

Dagnew A, Bitsuamlak GT. Computational evaluation of wind loads on standard tall building using a large eddy simulation, Wind & Structures 2014; 18(5), 567-598.

Davenport, A.G.1993.How can we simplify and generalize wind loads? Presented at the Third Asia-Pacific Symposium on Wind Engineering, Keynote Lecture, December13–15, Hong Kong.

Huang S, Li Q, Wu J. A general inflow turbulence generator for large eddy simulation. Journal of Wind Engineering and Industrial Aerodynamics 2010; 98, 600-617.

Kareem A, Spence SMJ, Bernardini E, Bobby S, Wei D. Using computational fluid dynamics to optimize tall building design. CTBUHJ. (III) 2013a; 38-42.

Kareem A, Bernardini E, Spence SMJ. Control of the Wind Induced Response of Structures. Springer, Tokyo, Japan 2013b, 377-410 (Chapter14).

Kareem A, Bobby S, Spence SMJ, Bernardini E. Optimizing the form of tall buildings to urban environments. In: CTBUH 2014 International Conference 2014.

Kareem A, Kijewski T, Tamura Y. Mitigation of motions of tall buildings with specific examples of recent applications. Wind and structures 1999; 2(3), 201-251.

Keating A, Piomelli U, Balaras E, Kaltenbach HJ. A priori and a posteriori tests of inflow conditions for large-eddy simulation. Physics of Fluids 2004; 16, 4696.

Kijewski T., Kareem A. 1998. Dynamic wind effects: a comparative study of provisions in codes and standards with wind tunnel data. Wind and Structures, 1(1), 77-109.

Kondo K, Murakami S, Mochida A. Generation of velocity fluctuations for inflow boundary condition of LES. Journal of Wind Engineering and Industrial Aerodynamics 1997; 67-68, 51-64.

Kwok KCS. Effects of building shape on wind-induced response of tall buildings. Journal of Wind Engineering and Industrial Aerodynamics 1988; 28, 381-90.

Liu KL, Pletcher RH. Inflow conditions for the large eddy simulation of turbulent boundary layers: a dynamic recycling procedure. Journal of Computational Physics 2006; 219 (1), 1-6.

Lund TS, Wu X, Squires KD. Generation of turbulent inflow data for spatially developing boundary layer simulations. Journal of Computational Physics 1998; 140, 233-258.

Nozawa K, Tamura T. Large eddy simulation of the flow around a low-rise building immersed in a rough-wall turbulent boundary layer. Journal of Wind Engineering and Industrial Aerodynamics 2002; 90, 1151-1162.

Smirnov R, Shi S, Celik I. Random flow generation technique for large eddy simulations and particle-dynamics modeling. Journal of Fluids Engineering 2001; 123, 359-371.

Tamura T, Miyagi T. The effect of turbulence on aerodynamic forces on a square cylinder with various corner shapes. Journal of Wind Engineering and Industrial Aerodynamics 1999; 83, 135-145.

Tamura, T. 2010a. Application of LES-based model to wind engineering- Implementation of meteorological effects. The Fifth International Symposium on Computational Wind Engineering, Chapel hill, NC, May 23-27.

Tamura, T. 2010b. LES for aerodynamic characteristics of a tall building inside a dense city district", The Fifth International Symposium on Computational Wind Engineering, Chapel hill, NC, May 23- 27.

Tominaga, Y., Mochida, A., Yoshiec, R., Kataokad, H., Nozu, T., Masaru Yoshikawa, M., Shirasawa, T. 2008. AIJ guidelines for practical applications of CFD to pedestrian wind environment around buildings. Journal of Wind Engineering and Industrial Aerodynamics, 96(10-11), 1749–1761.

Chapter 2

2 Consistent inflow turbulent generator for LES evaluation of wind-induced responses for tall buildings

2.1 Introduction

With encouraging development trends, both in software and hardware technology, the cost of conducting Large Eddy Simulation (LES) for wind engineering applications is becoming computationally affordable. This is also reflected through an increased number of publication that uses LES for variety of wind engineering applications. To give few examples, recently Dagnew and Bitsuamlak (2014) and Daniels *et al.* (2013) applied LES to evaluate wind load on standard tall buildings. Nozu et al. (2008), Tamura (2010a, b), Huang and Li (2010), Lim *et al.* (2009) employed LES to study building aerodynamics. Aboshosha *et al.* (2015) used LES to characterize the turbulence structure of downburst. Abdi and Bitsuamlak (2014) used LES among other turbulence models to characterize flow over topography. Tominaga and Stathopoulos (2010, 2011) used LES to study the pollution dispersion around a building and street canyon, respectively, Gousseau *et al.* (2013) used LES to study pollution dispersion in a city center, and Jiang *et al.* (2013) used LES to study natural ventilation.

The importance of defining proper inflow boundary condition (i.e. turbulence) while using LES was extensively discussed by various researchers (Sagaut *et al.* 2003; Tutar and Celik 2007; Xie and Castro 2008; Tominaga *et al*. 2008; Dagnew and Bitsuamlak 2013). The inflow condition should satisfy specific spectra, correlations and magnitudes. To this end, several techniques are available in the literature (Kondo *et al.* 1997; Smirnov *et al.* 2001; Jarrin *et al.* 2006; Tamura 2000). Keating *et al.* (2004) classified the techniques used to generate inflow turbulence for LES into three categories, which are (i) precursor database, (ii) recycling method and (iii) synthetic turbulence. Liu and Pletcher (2006) provided a review on the precursor database and recycling method. In the precursor database, simulation of the flow around a targeted zone is conducted in two stages. In the first stage, a parent simulation for the incoming wind upstream to the zone of interest is conducted to obtain incoming temporal and spatial turbulent velocities. These turbulent velocities are saved in a database and used for the second simulation stage, where the flow is focused on the zone of interest. Although this method is employed previously in wind engineering application, it is computationally costly and not preferable unless the first simulation stage already exists and turbulent velocity database is available (Bitsuamlak and Simiu 2010). Lund *et al.* (1998) used the recycling method to generate inflow velocities for smooth terrains. Nozawa and Tamura (2002) extended Lund's method and employed it with rough terrains. Similar to precursor database method, computational domain is divided into two in the recycling method: (i) the driver domain and (ii) the calculation domain. In the driver domain, the flow is recycled over a short domain until the flow becomes statistically stable. Flow characteristics on a mapping plane is stored and used as the inflow condition for the calculation domain as illustrated in Figure 2-1. The main drawback of the recycling method is that resulting inflow characteristics are dependent on the roughness elements used at the floor of the driver domain. Unless shape and distribution of the roughness elements leading to targeted flow characteristics (i.e. terrain exposure) are known, this method cannot be used (Tamura 2008). Aboshosha (2014) suggested a technique suitable for recycling method that allows for simulating any targeted terrain exposure through the usage of fractal surfaces. This technique has been utilized by Aboshosha *et al.* (2015) while studying downburst flows for various terrain exposures. The drawback associated with all recycling methods is the requirement for a parent simulation using a driver domain that makes the turbulent inflow generation time consuming compared with other methods such as synthesizing inflow turbulence (Tamura 2008). Synthesizing inflow turbulence does not require costly prior simulations, making it a more robust approach provided that the target flow statistics are met satisfactorily.

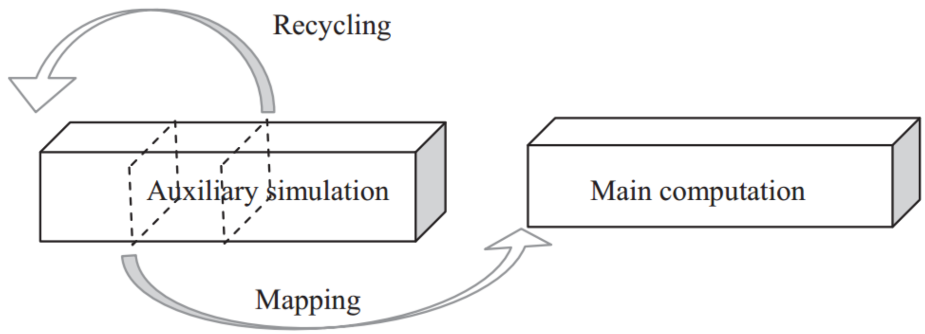

Figure 2-1 Recycling technique (Lund et al. 1998)

According to Huang et al. (2010), synthesizing inflow turbulence techniques can be classified into two main groups. The first group include the work of Hoshiya (1972), Iwatani (1982), Maruyama and Morikawa (1994), and Kondo et al. (1997). This group uses a weighted amplitude wave superposition method (WAWS) which results in a turbulent velocity field that satisfies both the targeted power and cross spectra.

The drawback of this method is that resulting turbulent field is not dependent on the computational grid used, thus, does not satisfy the continuity condition of the flow (i.e. divergence free is not guaranteed). This would require enormous effort from the solver to correct the assigned flow field and enforce the continuity (Tamura 2008). Kondo et al. (1997) employed the method originally developed by Shirani et al. (1981) to make the generated inflow divergent free. However, the step involved to maintain the divergence free criterion alters the targeted statistical characteristics. Kim et al. (2013) suggested to introduce the turbulent field on a vertical plane near (rather than at) the inlet and relied on the pressure-correction to maintain the divergence free criterion. This reduced degradation of the statistical characteristics compared to when the field is introduced right at the inlet. Daniels et al. (2014) employed this method to estimate peak pressures on a typical tall building and reported that the method is rapid and led to encouraging results. The second group include the work of Kraichnan (1970), Li et al. (1994), Bechara et al. (1994), Fung et al. (1992), Smirnov et al. (2001), Klein et al. (2003), and Batten et al. (2004). This group generates divergent-free velocity field with Gaussian spectra and is usually referred as random flow generation (RFG) method. This approach is also implemented in many commercial CFD software. Unfortunately, turbulent spectra in the atmospheric boundary layer (ABL) is different from Gaussian spectra (Lumley and Panofsky 1964), thus making RFG method not suitable for wind engineering application. Huang et al. (2010) suggested the discrete random flow generation (DRFG) method to produce turbulent velocity field that has turbulent spectra close to the target ABL flow characteristics that forms also the basis for current study. Castro et al. (2011) proposed a modification to the DRFG method to obtain velocity field that had a better match with the target spectra. Generally, the DRFG method is able to generate turbulent spectra that is close to the target, maintain the spatial correlation among the resulting velocities, and can easily be implemented in parallel computing environment. Table 2-1 summarizes the methods available in the literature to generate the inflow condition.

Table 2-1 Inflow generation methods

Group/ Subgroup		Study	Comments
Precursor database		Bitsuamlak and Simiu 2010	Two steps (i) parent simulation for the incoming wind upstream and, (ii) second simulation for the targeted zone
Recycling method		Lund *et al.* (1998)	Generate inflow for smooth terrains
		Nozawa and Tamura (2002)	Generate inflow for rough terrains
		Aboshosha (2014)	Simulated any targeted terrain exposure through the usage of fractal surfaces
Synthetic turbulence	WAWS	Hoshiya (1972), Iwatani (1982), Maruyama and Morikawa (1994), Kondo et al. (1997)	Turbulent field is not dependent on the computational grid, thus, does not satisfy the continuity condition
		Kondo et al. (1997), Kim et al. (2013)	Suggested methods to satisfy the divergence free criterion but affects the targeted statistical properties, coherency among the velocities is not maintained
	RFG	Kraichnan (1970), Li et al. (1994), Bechara et al. (1994), Fung et al. (1992), Smirnov et al. (2001), Klein et al. (2003), Batten et al. (2004)	Gaussian spectra, which is not compatible with the spectra in the ABL
		Huang et al. (2010) and Castro et al. (2011)	Turbulent spectra that is close to the target, maintain the spatial correlation among the resulting velocities, easily be implemented in

parallel computing environment, coherency among the velocities is not maintained.

However, there are other additional important conditions that needs to be satisfied by the generated inflow for wind engineering applications such as maintaining the proper coherence among the velocities (Davenport 1993). This include maintaining proper correlations among the turbulent velocities within different frequencies as indicated by Davenport (1993) and Kijewski and Kareem (1998). Another important condition is modeling the turbulent spectra to be exactly similar as the target flow. Unfortunately, these conditions are not met by the DRFG method, as will be illustrated in the following section. The current study focuses on modifying the DRFG method to maintain the proper coherency among the resulting turbulent velocities. The modified method is named consistent DRFG (or CDRFG) method. In the following sections of the paper presents brief discussion on the original DRFG method as suggested by Huang *et al.* (2010) and highlights the rational that led to the need to improve the spectra and coherency function of inflow turbulence to better fit the target flow characteristics (section 2). Proposed modifications to the DRFG technique (CDRFG technique) enabled robust modeling of the spectra and the coherency function and are presented in section 3. In section 4, both the new CDRFG and the original DRFEG techniques are applied as inflow boundary conditions of LES to evaluate wind-induced responses of a typical tall building. The numerical results are then compared with aerodynamic data obtained from a boundary layer wind tunnel test for assessing their respective performance.

2.2 Discrete random inflow generation

As mentioned earlier, Huang *et al.* (2010) proposed the discrete random flow generation (DSRG) technique to generate turbulent velocity field that satisfies the targeted turbulent spectra and spatial correlations. The technique is based on discretizing power spectra of velocities into *M* number of segments and generate wind field within each of these segments using the original random flow generation (RFG) technique (Kraichnan 1971 and Smirnov 2001), but with some modifications to allow for modeling a spectrum with arbitrary distribution. According to Huang *et al.* (2010), turbulent velocity field, $u_i(x_j,t)$ can be generated using Equation 2-1Equation 6-1.

$$u_i(x_j,t) = \sum_{m=1}^{M}\sum_{n=1}^{N} p_i^{m,n}\cos\left(k_j^{m,n}.x_j^{\ m} + 2.\pi f_{n,m}t\right) + q_i^{m,n}\sin\left(k_j^{m,n}.x_j^{\ m} + 2.\pi f_{n,m}t\right) \quad \text{Equation 2-1}$$

where u_i represent longitudinal *u*, transverse *v*, and vertical *w* velocities, respectively; j=1, 2 and 3 represent x, y and z directions, respectively; *M* is the number of spectral segments; *N* is the number of random frequencies within each segment; $p_i^{m,n}$ and $q_i^{m,n}$ are parameters defined in Equation 2-2; $f_{n,m}$ is a normally distributed random number with 0 mean and f_m standard deviation; $k_j^{m,n}$ are coordinates of a uniformly distributed points on a sphere with a unit radius that satisfy Equation 2-3 to maintain the divergence free condition; $x_j^{\ m}$ is a non-dimensional location coordinate where the velocity is being generated and is defined by Equation 2-4, where x_j is the location coordinate in the *j* direction.

$$p_i^{m,n} = sign\left(r_i^{m,n}\right)\cdot 2\cdot\sqrt{\frac{1}{N}S_{ui}(f_m).\Delta f\ \frac{\left(r_i^{m,n}\right)^2}{1+\left(r_i^{m,n}\right)^2}}$$

$$q_i^{m,n} = sign\left(r_i^{m,n}\right)\cdot 2\cdot\sqrt{\frac{1}{N}S_{ui}(f_m).\Delta f\ \frac{1}{1+\left(r_i^{m,n}\right)^2}} \quad \text{Equation 2-2}$$

where $S_{ui}(f_m)$ is the spectra in the direction *i* at the frequency f_m and $r_i^{m,n}$ is a normally distributed random number with zero mean and unit standard deviation, Δf_m. is bandwidth defining the spectra segment.

$$\begin{bmatrix} p_x^{\ m,n} & p_y^{\ m,n} & p_z^{\ m,n} \\ q_x^{\ m,n} & q_y^{\ m,n} & q_z^{\ m,n} \\ k_x^{\ m.n} & k_y^{\ m.n} & k_z^{\ m.n} \end{bmatrix}\begin{Bmatrix} k_x^{\ m.n} \\ k_y^{\ m.n} \\ k_z^{\ m.n} \end{Bmatrix} = \begin{Bmatrix} 0 \\ 0 \\ 1 \end{Bmatrix} \quad \text{Equation 2-3}$$

$$x_j^{\,m} = \frac{x_j}{L_j^{\,m}} \qquad \text{Equation 2-4}$$

The parameter $L_j^{\,m}$ in Equation 2-4 characterizes the spatial correlations between the generated velocity field. Huang *et al.* (2010) suggested to relate the parameter $L_j^{\,m}$ to the integral length scale of turbulence $C_L.L_{uj}$, where C_L is a factor ranging between 1 and 2, with an average value of 1.5. They compared the spatial correlation of the generated velocity vectors with the target and found that a value of 1.5 L_{uj} leads to a good agreement. It should be mentioned that Huang *et al.* (2010) uses a frequency independent parameter $L_j^{\,m}$, which is expected to result in a frequency independent correlation (i.e. same correlation for all frequencies). This contradicts with the fact that large eddies (with low frequencies) have higher correlations than small eddies (with high frequencies) (Davenport 1967 and 1993). It is to be noted that maintaining proper frequency-dependent correlations is very important while estimating wind-induced responses of flexible structures such as tall buildings and long span bridges (Davenport 1993). Another disadvantage of DRFG technique is that spectra of the resulting turbulent deviates from the target ABL flow statistics (Castro *et al*. 2011). To explain these limitations more specifically, DRFG technique (Equations 1-4) is used to generate turbulent velocity field for an urban terrain defined by using $L_j^{\,m}$ = 1.5 L_{ui} and parameters summarized in Table 2-2. These parameters are chosen to match the urban exposure used in the boundary layer wind tunnel experiments reported by Kijewski and Kareem (1998) and Zhou *et al.* (2003). More specifically mean velocity, turbulent intensity and longitudinal integral scale of turbulence were adopted from Zhou *et al.* (2003). The target coherency function (expression given in Table 2-1) is adopted from Davenport (1993). Other parameters (listed in Table 2-1) that are required for the inflow generation are adopted from ESDU (2001) for urban terrain exposure.

Table 2-2 Parameters used for generating velocity field for urban terrain exposure

Parameter	Definition/ Value
Exposure	Urban
Mean velocity U_{av}	$U_{av} = U_{avref}\left(\frac{z}{z_{ref}}\right)^{\alpha}$, U_{avref} =10 m/s, z_{ref}= 0.364 m, α=0.326
Turbulent intensity I	$I_j = I_{refj}\left(\frac{z}{z_{ref}}\right)^{-dj}$ where I_{refj} = 0.208, 0.182, 0.152 and d_j = 0.191, 0.123, 0.005 in the *u*, *v* and *w* directions, respectively. (Zhou *et al.* 2003; ESDU 2001)
von Karman turbulent spectra S_u, S_v, S_w	$S_u = \frac{4(I_u U_{av})^2 (L_u / U_{av})}{\left(1+70.8(fL_u/U_{av})^2\right)^{5/6}}$ $S_v = \frac{4(I_v U_{av})^2 (L_v / U_{av})\left(1+188.4(2fL_v/U_{av})^2\right)}{\left(1+70.8(2fL_v/U_{av})^2\right)^{11/6}}$ $S_w = \frac{4(I_w U_{av})^2 (L_w / U_{av})\left(1+188.4(2fL_w/U_{av})^2\right)}{\left(1+70.8(2fL_w/U_{av})^2\right)^{11/6}}$ where $L_j = L_{refj}\left(\frac{z}{z_{refL}}\right)^{\varepsilon_j}$, L_{refJ} = 0.302, 0.0815, 0.0326 m, ε_j = 0.473, 0.881, 1.539, in x, y, z directions respectively; z_{refL} =0.254 m
Coherency function	$Coh(f_m) = \exp\left(-\frac{C_j f_m dx_j}{U_{av}}\right)$ (Davenport 1993) where C_j is coherency decay constant.
Other parameters	$f_{m\,min}$=1.0 hz, $f_{m\,max}$= 100 hz, Δ_f=1.0 hz, M=100, N=50

Figure 2-2 shows the coherency function between resulting two velocities vectors at heights of 0.1 m and 0.3 m from ground. The resulting coherency function is compared with the targeted coherency function suggested by Davenport (1993) (given in Table 2-1) using a coherency decay constant, C_j, of 10 (Davenport 1993, Kijewski and Kareem 1998).

As shown in Figure 2-2, the coherency produced by adopting the DRFG technique is frequency independent and fails to capture the decaying distribution with the frequency increase. This leads, for example, to an overestimation of the forces acting on structures that has fundamental frequency greater than f_{int}, shown in Figure 2-2.

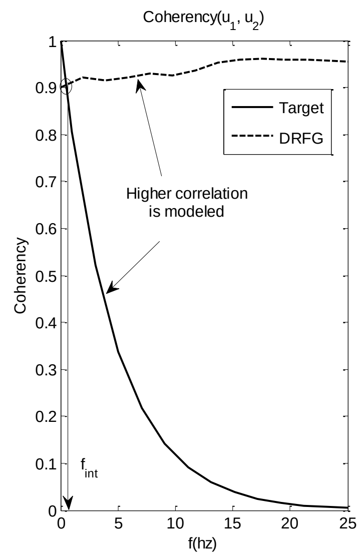

Figure 2-2 coherency function between velocities at points 1 and 2 resulting from the DRFG technique

Figure 2-3 shows the velocity and the spectra plots at point 2 (located at a height of 0.3 m from ground), in the longitudinal, transverse and vertical directions compared with von Karman spectra. The same figure also includes the smoothed spectra of the resulting velocities (i.e. after applying a moving average) which allows for an easier comparison with the target spectra. As indicated from the figure, the resulting spectra from DRFG do not match the target spectra at low frequencies. Similar observation was also reported by Castro *et al.* (2011). Such a discrepancy in the resulting spectra can lead to erroneous wind-induced structural responses, especially if this discrepancy occurs close to the natural frequencies of the structure. In the following section, proposed solutions to address the discrepancies both in the coherency and the spectra produced while using DRFG technique are presented.

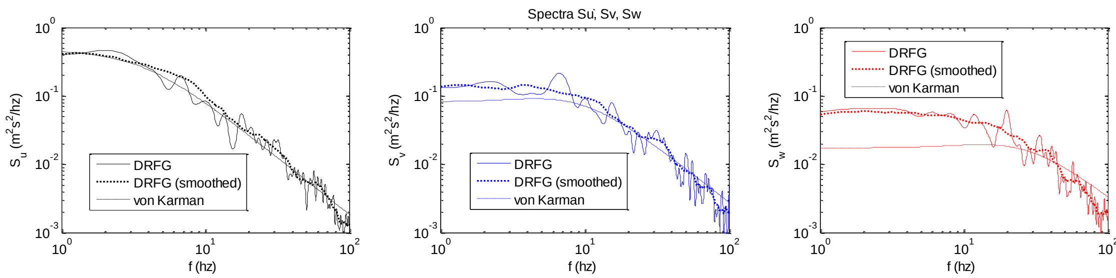

Figure 2-3 Sample velocity time history resulting from the DRFG (Huang *et al.* 2010) and their spectral plots

2.3 Consistent discrete random inflow generation (CDRFG)

As illustrated in the previous section, turbulent velocities generated using DRFG technique have some coherency and spectra discrepancies compared to the target flow statistics observed in ABL flows. These limitations shall be addressed while using the technique to evaluate wind-induced response of structures. Proposed enhancements to DRFG technique are presented in this section. The proposed solutions to correct the inflow spectra are presented first, followed by the proposed enhancements for producing consistent coherency in the velocity field. From here after the modified technique will be referred as consistent discrete random flow generation (CDRFG) technique, as it generates consistent turbulent velocities (i.e. having spectra and coherency function that match the ABL flow statistics) as will be shown later in this section.

2.3.1 Consistent wind spectra

According to Huang *et al.* (2010), turbulent velocity resulting from DRFG technique corresponding to a frequency f_m, $u_i(x_j, t, f_m)$, can be generated using Equation 2-5, where the frequency $f_{n,m}$ is a random frequency with zero mean and f_m standard deviation. Figure 2-4 illustrates the velocity records resulting from Equation 2-5using f_m = 20 Hz for the urban exposure parameters summarized in Table 2-2.

$$u_i(x_j, t, f_m) = \sum_{n=1}^{N} p_i^{m,n} \cos\left(k_j^{m,n}.x_j^{\ m} + 2.\pi f_{n,m} t\right) + q_i^{m,n} \sin\left(k_j^{m,n}.x_j^{\ m} + 2.\pi f_{n,m} t\right)$$ Equation 2-5

As shown in Figure 4, the resulting spectra have multiple peaks in the frequency band ranging approximately between 0 and 3 f_m. This means that DRFG technique distributes the energy spectra for the frequency f_m over a band of frequencies 0-3 f_m, as opposed to focusing the energy close to f_m. This is believed to be the main reason for the spectral discrepancy shown in Figure 2-4.

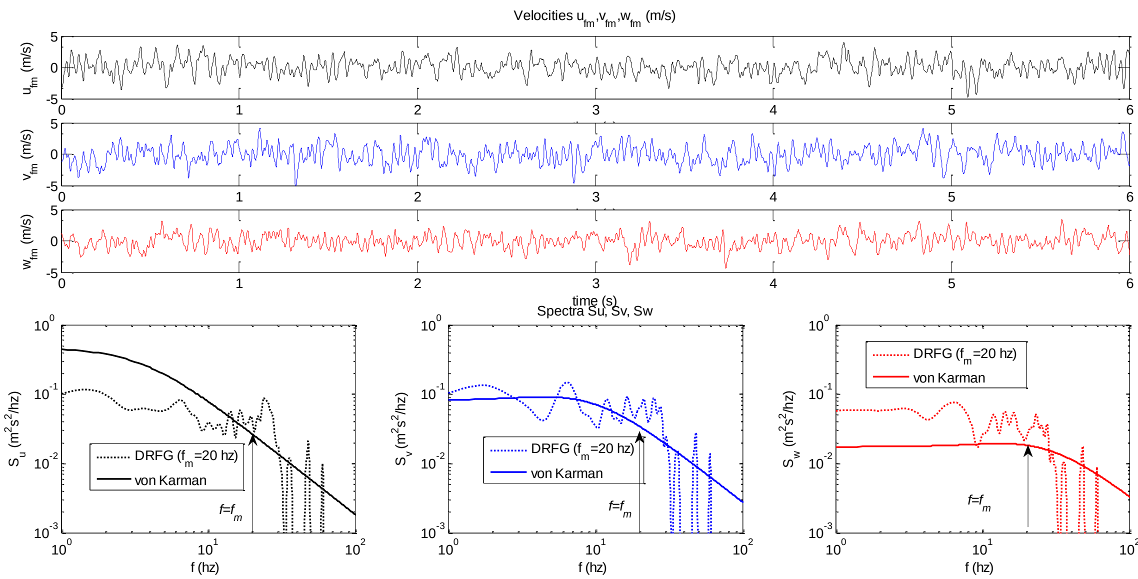

Figure 2-4 Velocity time history resulting from DRFG using a single f_m of 20 Hz and their spectral plots

In order to correct the discrepancy in the resulting spectra, it is suggested to use random frequencies fn,m that are more focused near the frequency fm. Random frequencies fn,m are chosen here to have a mean value of fm and a standard deviation of Δ_f, where Δ_f is frequency step used to represent the target spectra. The magnitude of the factors $p^i_{m,n}$ and $q^i_{m,n}$ is halved according to Equation 2-6 in order to compensate for the new utilized values of frequencies $f_{n,m}$. The resulting velocity and spectra obtained using the updated expressions for $f_{n,m}$, $p^i_{m,n}$ and $q^i_{m,n}$ expressions, and employing Δ_f =1.0 Hz, are shown in

Figure 2-5. As shown in Figure 2-5, the resulting spectra are more focused around the frequency $f_{n,m}$ and closer to the targeted value.

$$p_i^{m,n} = sign\left(r_i^{m,n}\right)\sqrt{\frac{1}{N}S_{ui}{}^{m}.\Delta f\,\frac{\left(r_i^{m,n}\right)^2}{1+\left(r_i^{m,n}\right)^2}}$$

Equation 2-6

$$q_i^{m,n} = sign\left(r_i^{m,n}\right)\sqrt{\frac{1}{N}S_{ui}{}^{m}.\Delta f\,\frac{1}{1+\left(r_i^{m,n}\right)^2}}$$

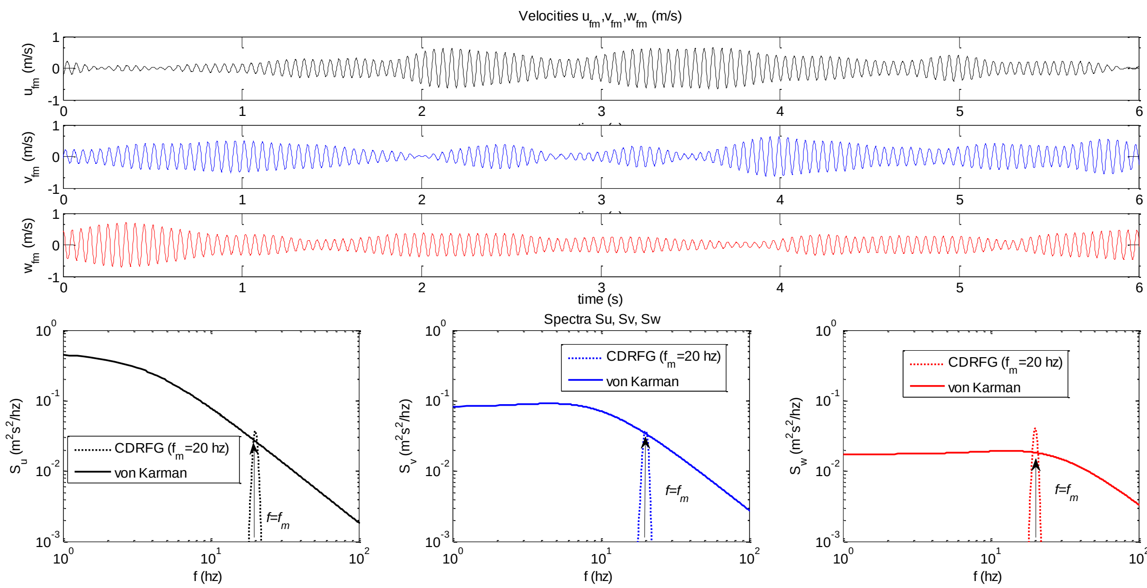

Figure 2-5 Velocity time history resulting from CDRFG and their spectral plots using one fm = 20 Hz (Equation 6 using updated fn,m, pim,n and qim,n expressions)

The new expressions for $f_{n,m}$, $p_i^{m,n}$, and $q_i^{m,n}$ are used with Equation 1 to generate turbulent velocities that has entire turbulent spectra. The resulting turbulent velocities and spectra are shown in Figure 2-6 for a point located at height of 0.3 m. By comparing the resulting spectra using the new expressions for $f_{n,m}$, $p_i^{m,n}$ and $q_i^{m,n}$ with von Karman spectra, it can be noticed from Figure 2-6 that the new expressions generated flow statistics very close to the target.

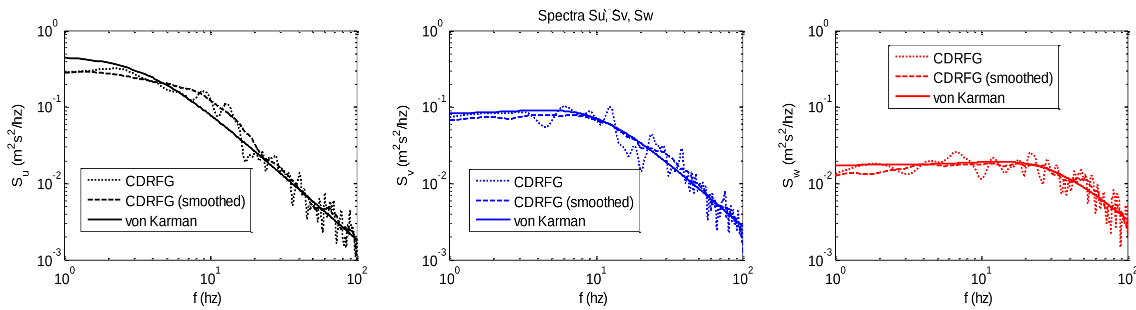

Figure 2-6 Sample velocity time history resulting from CDRFG and their spectral plots

2.3.2 Correction for the coherency function

As discussed earlier, the DRFG technique leads to unrealistic coherency function that is frequency independent. To address this shortcoming, it is proposed to relate the parameter L_j^m, which characterizes the correlations to the frequency, f_m, in accordance with Equation 2-7.

$$L_j^m = \frac{U_{av}}{\gamma . C_j . f_m} \quad \text{Equation 2-7}$$

where U_{av} is the mean velocity, f_m is the frequency at segment m, γ is a tuning factor, C_j is the coherency decay constant and j=1, 2, and 3 represents longitudinal, transverse and vertical directions, respectively.

The expression given by Equation 2-7 requires the tuning factor γ to be defined. This tuning factor is estimated from the non-dimensional length scale, $\beta = CD / L_u$, where $L_u(z)$ is the longitudinal length scale of turbulence, D is a characteristic distance chosen to tune the correlations, and C is the coherency decay constant. The characteristic distance D is function of the problem being solved. Estimating the tuning factor γ from the non-dimensional length scale β is conducted in three steps. In the first step, an expression for coherency function resulting from the DRFG (Equation 2-1) technique using the new definition for L_j^m (Equation 2-7) is obtained. The coherence is a function of the tuning factor γ. In the second step, target coherency function reported by Davenport (1993) (see Table 2-1) is fitted with the resulting coherency function from the first step using γ as the fitting parameter. It is observed that depending on the area under the coherency curve (i.e. correlation in the wide frequency band, R_{u1u2}^{*}), different values of the tuning factor γ are obtained. This leads to a relationship between γ and R_{u1u2}^{*}. In the third step, an expression for R_{u1u2}^{*} is obtained as a function of the non-dimensional length scale β, which is used to obtain the relationship between γ and β. All the mathematical expressions employed at each step to relate γ and β are given below.

Step 1: Coherence resulting from CDRFG

Coherency function based on the new definition of L_j^m (Equation 2-7) can be calculated as the cross correlation between velocities generated by Equation 2-5 close to the frequency f_m. Derivation for resulting coherency function is given in Equation 2-8

$$
\begin{aligned}
&Coh_{u_1,u_2}(f_m) = \frac{\left|\sigma_{u_1u_2}\right|}{\sigma_{u_1}\sigma_{u_2}} \\
&u_1(f_m) = \sum_{n=1}^{N} p_{i1}^{m,n}\cos\left(k_j^{m,n} x_{1j}^{m} + 2\pi f_{n,m}t\right) + q_{i1}^{m,n}\sin\left(k_j^{m,n}.x_{1j}^{m} + 2\pi f_{n,m}t\right) \\
&u_2(f_m) = \sum_{n=1}^{N} p_{i2}^{m,n}\cos\left(k_j^{m,n} x_{2j}^{m} + 2\pi f_{n,m}t\right) + q_{i2}^{m,n}\sin\left(k_j^{m,n} x_{2j}^{m} + 2\pi f_{n,m}t\right) \\
&\sigma_{u_1u_2} = \frac{1}{T}\int_0^T \sum_{n=1}^{N}\left(p_{i1}^{m,n} p_{i2}^{m,n}\right)\cos\left(k_j^{m,n} x_{1j}^{m} + 2\pi f_{n,m}t\right)\cos\left(k_j^{m,n} x_{2j}^{m} + 2\pi f_{n,m}t\right) + \\
&\qquad \frac{1}{T}\int_0^T \sum_{n=1}^{N}\left(q_{i1}^{m,n}.q_{i2}^{m,n}\right)\sin\left(k_j^{m,n}.x_{1j}^{m} + 2\pi f_{n,m}t\right)\sin\left(k_j^{m,n}.x_{2j}^{m} + 2\pi f_{n,m}t\right)
\end{aligned}
\qquad \text{Equation 2-8}
$$

$$\sigma_{u_1u_2} = \sum_{n=1}^{N} \frac{\left(p_{i1}{}^{m,n}.p_{i2}{}^{m,n}\right)}{2} \cos\left(k_j{}^{m,n}\left(x_{1\,j}{}^{m} - x_{2\,j}{}^{m}\right)\right) + \sum_{n=1}^{N} \frac{\left(q_{i1}{}^{m,n}.q_{i2}{}^{m,n}\right)}{2} \cos\left(k_j{}^{m,n}\left(x_{1\,j}{}^{m} - x_{2\,j}{}^{m}\right)\right)$$

$$\sigma_{u_1u_2} = \sqrt{S_{u_1}(f_m)S_{u_2}(f_m)}\Delta_f \sum_{n=1}^{N} \cos\left(k_j{}^{m,n}\left(x_{1\,j}{}^{m} - x_{2\,j}{}^{m}\right)\right)$$

$$\sigma_{u_1} = S_{u_1}(f_m)\Delta_f, \sigma_{u_2} = S_{u_2}(f_m)\Delta_f$$

$$Coh_{u_1,u_2}(f_m) = \sum_{n=1}^{N} \cos\left(k_j{}^{m,n}\left(x_{1\,j}{}^{m} - x_{2\,j}{}^{m}\right)\right)$$

$$Coh_{u_1,u_2}(f_m) = \sum_{n=1}^{N} \cos\left(\gamma k_j{}^{m,n} C_f\right)$$

where $C_f = C \cdot f \cdot d / U_{av}$, C is coherency decay constant, and d is the distance between points 1 and 2.

Step 2: Relationship between γ and $R_{u1u2}{}^{*}$

As indicated from Equation 2-8, resulting coherency function from CDRFG technique is dependent on tuning factor γ and non-dimensional frequency C_f. This resulting coherency function needs to be equal to targeted coherency (given in Table 1). By fitting the resulting coherency function (Equation 2-8)with targeted coherency function (given in Table 1), factor γ is obtained as the fitting parameter. Depending on the area under the coherency curve (i.e. cross correlation in the wide frequency band, $R_{u1u2}{}^{*}$), different values of γ are found as shown in Figures 7(a), (b) and (c). The cross correlation in the wide frequency band, $R_{u1u2}{}^{*}$, can be expressed by Equation 2-9 and is shown in Figure 2-7(a), (b) and (c).

$$R_{u1u2}{}^{*} = \frac{\int_0^{f\max} Coh(f).df}{\int_0^{f\max} df} \qquad \text{Equation 2-9}$$

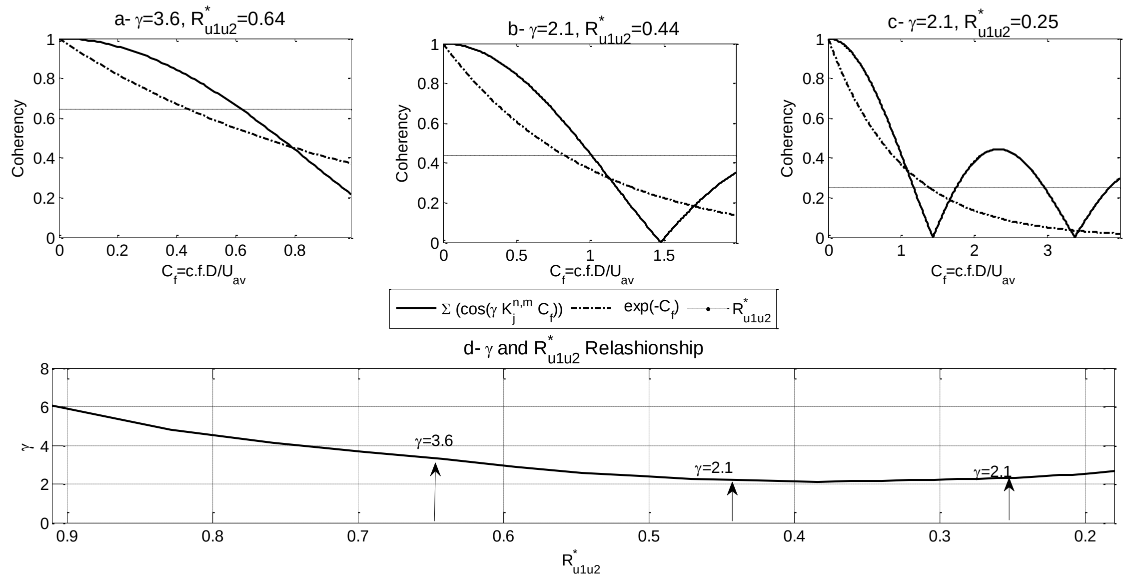

Figure 2-7 Fitting process for coherency function resulting from CDRFG technique for different Ru1u2* values (a) to (c) , and (d) relationship between Ru1u2* and γ

Figure 2-7(d) shows the relationship between γ and R_{u1u2}^*. This relationship allows for estimating γ provided that R_{u1u2}^* is known. In the next step, R_{u1u2}^* is related to the non-dimensional length scale, β, and then a relationship between γ and β is obtained.

Step 3: Relationship between γ and β

Cross-correlation between velocities u_1 and u_2, R_{u1u2}^*, is calculated as the ratio between velocity covariance $\sigma_{u_1u_2}{}^*$ and rms velocities $\sigma_{u_1}{}^*$ and $\sigma_{u_2}{}^*$, as expressed by Equation 2-10. By using von Karman spectra to model the distribution of the turbulent energy, R_{u1u2}^* is obtained as a function of $\beta = CD / L_u$ and plotted in Figure 2-8(a).

$$R_{u1u2}{}^{*} = \frac{\sigma_{u_1u_2}{}^{*}}{\sigma_{u_1}{}^{*}\sigma_{u_2}{}^{*}} = \frac{\int_0^\infty \sqrt{S_{u1}.S_{u2}}.e^{-\frac{cfD}{U_{av}}}df}{\sqrt{\int_0^\infty S_{u1}df}\sqrt{\int_0^\infty S_{u2}df}}$$

$$S_{u1} = \frac{\sigma_{u1}{}^{*2}4\left(L_u/U_{av}\right)}{\left(1+70.8n^2\right)^{5/6}}$$

Equation 2-10

$$S_{u2} = \frac{\sigma_{u2}{}^{*2}4\left(L_u/U_{av}\right)}{\left(1+70.8n^2\right)^{5/6}}$$

$$n = fL_u/U_{av}$$

$$R^{*}_{u1u2} = \int_0^\infty \frac{4}{\left(1+70.8n^2\right)^{5/6}}.e^{-\beta n}dn = f\left(\beta\right)$$

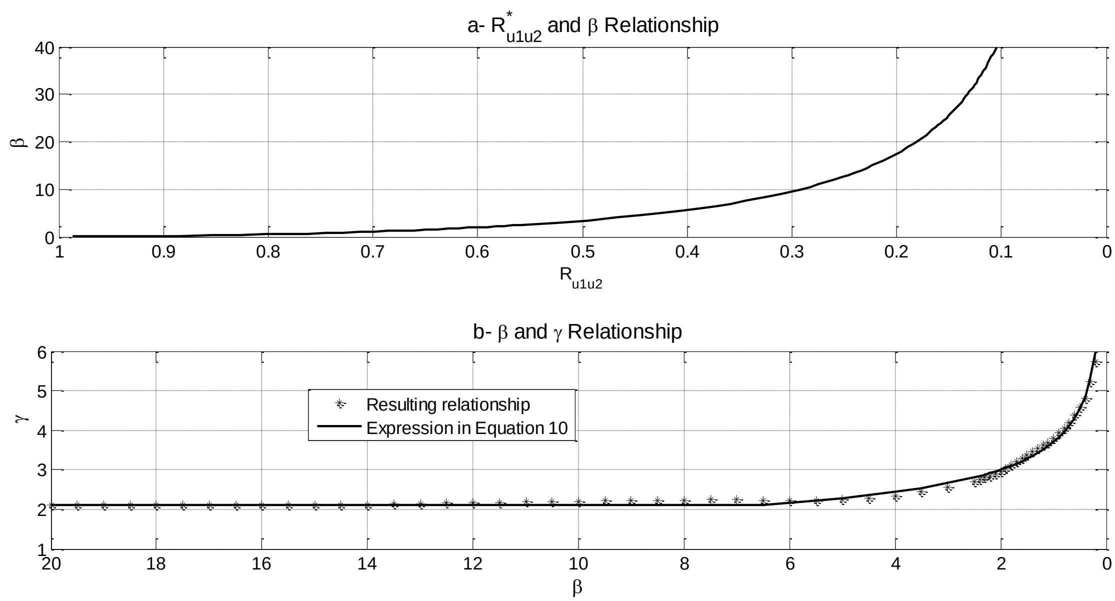

Figure 2-8 Relationship between Ru1u2*, β and γ

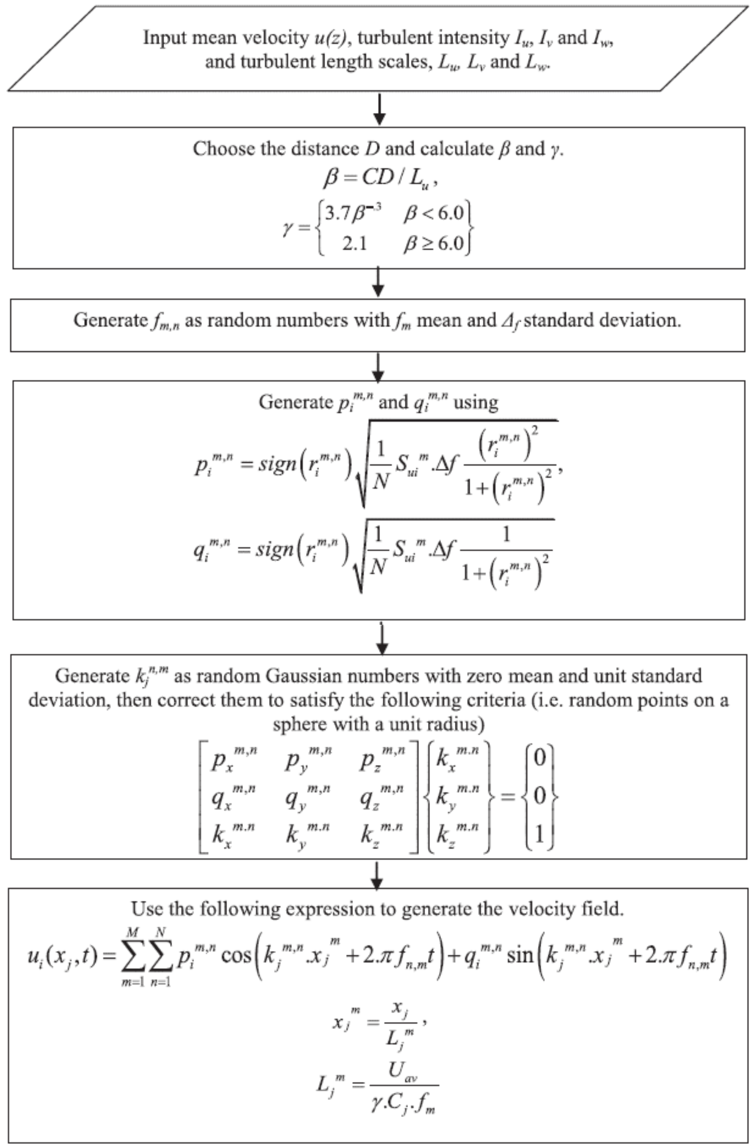

Figure 2-9 CDRFG technique flow chart

As shown in Figure 2-7(d), R_{u1u2}^{*} is also a function of γ. By equating R_{u1u2}^{*} from Figure 2-7 (d) and from Figure 2-8(a), a relationship between γ and β is obtained, as shown in Figure 2-8(b). This relationship can be expressed by Equation 2-11, which is also plotted in Figure 2-8 (b).

$$\gamma = \begin{Bmatrix} 3.7\beta^{-.3} & \beta < 6.0 \\ 2.1 & \beta \geq 6.0 \end{Bmatrix}$$ Equation 2-11

The flowchart shown in Figure 2-9 summarizes all the steps involved in the CDRFG technique. A MATLAB code is developed to conduct the velocity turbulent generation using CDRFG. Figure 2-9 shows that the user needs to choose the distance *D* to tune the correlations. This distance shall be related to the problem being solved. For instance, *D* shall be taken in the order of 0.5-1.0 *h*, for a tall building with a height *h* to maintain the proper correlation along the building height. It is worth mentioning that values of *D* making β = CD/ L_u, greater than 6, would result in a tuning factor γ independent of *D*, as indicated from Figure 8(b).

The accuracy of the CDRFG technique described in Figure 2-9 to model the proper coherency function is assessed by generating velocity vectors for the urban boundary layer with the parameters summarized in Table 2-2. A value of the distance *D* equal to 0.2 m ($\beta=6.7$) is chosen to tune the correlation. The resulting velocities at point 1 (at 0.1 m height) and point 2 (at 0.3 m height) are plotted in Figure 2-10. In the same figure, the resulting coherency function between the two velocities is compared with the targeted coherency (Equation 5). Figure 2-11 shows coherency functions between velocities with separation distances, d=0.1 and 0.3 m. As indicated from these figures, it is fair to conclude that CDRFG technique is able to maintain the proper coherency among resulting turbulent velocities.

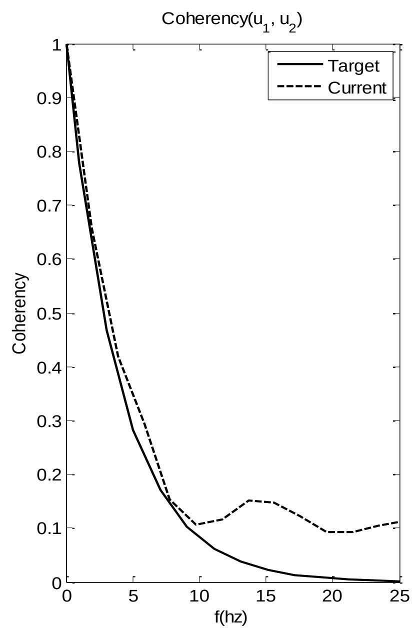

Figure 2-10 Velocity time histories and coherency functions at points 1 and 2 resulting from the CDRFG technique

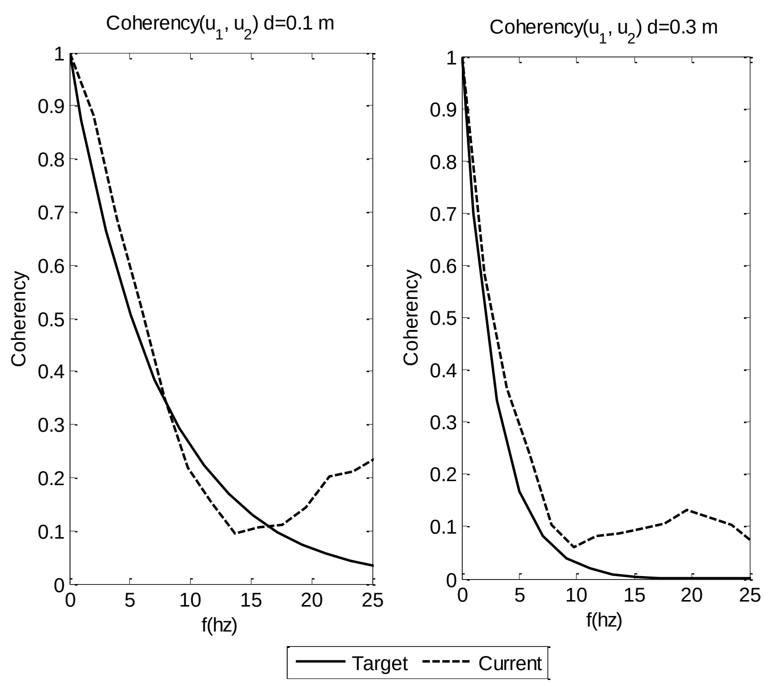

Figure 2-11 Target and resulting coherency functions for different separation distances

In the next section, CDRFG technique is employed to evaluate the dynamic response of a tall building that was previously tested in a boundary layer wind tunnel (Kijewski and

Kareem 1998, Zhou *et al*. 2003). Its efficacy is examined through comparison of the numerical aerodynamic data with those obtained from boundary layer wind tunnel.

2.4 Application of CDRFG to evaluate wind load on a tall building

2.4.1 Numerical model description

LES of flow around a tall building placed in an urban boundary layer is conducted to examine efficiency of the developed technique. Properties of the boundary layer and the building are summarized in Table 2-1Table 2-2, respectively. Inflow field generated by using both the CDRFG and DRFG techniques are employed to test the applicability of both techniques to evaluate the building dynamic response. This is achieved by comparing the building's dynamic responses using the two inflow techniques with those obtained from the boundary layer wind tunnel experiment (Kijewski and Kareem 1998, Zhou *et al.* 2003). The simulations are conducted using a length scale of 1:500 and a velocity at the building top equal to 10 m/s.

Table 2-3 Properties of the examined building

Property	Value
Height H_s, Width W_s, Depth D_s	182.2, 30.48, 30.48 m
Natural Frequency	0.15 (along wind), 0.15 (across wind), 0.3 (torsional)
Damping ratio	1% for all modes
Mass per unit volume m_s	192 kg/m^3
Air density	1.25 kg/m^3

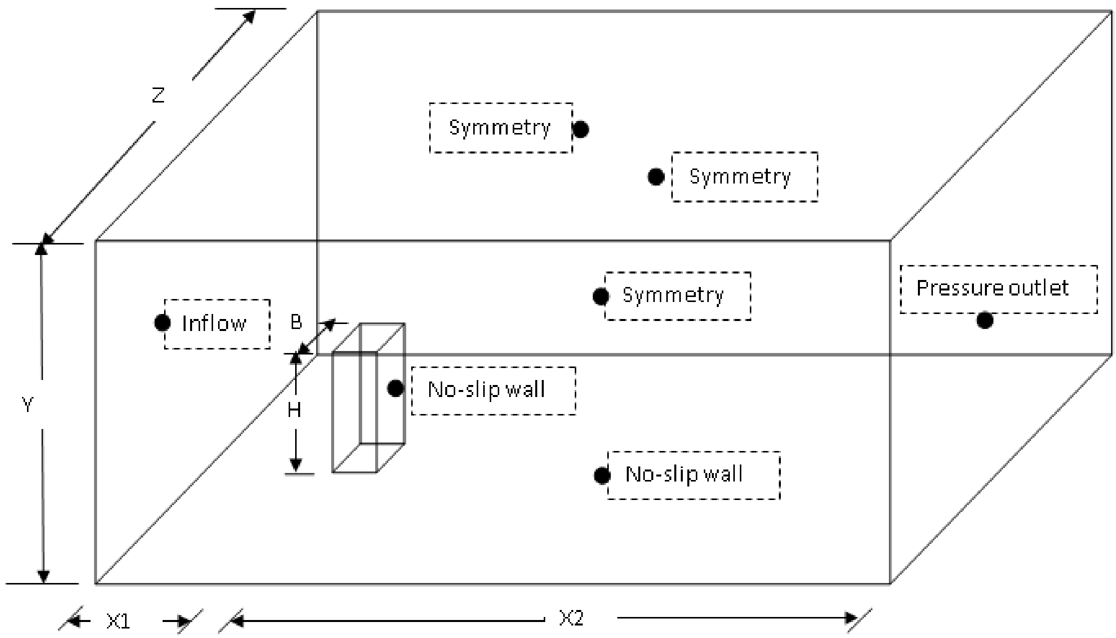

Figure 2-12 Boundary conditions and domain dimensions

Table 2-4 Computational domain dimensions

Parameter	Current	Cost (2007)	AIJ (2008)
X1	5 *H* (30 *B*)	5 *H*	36 *B*
X2	15 *H* (90 *B*)	15 *H*	
Y	10 *H* (60 *B*)	4.6 *H*	21.6 *B*
Z	4 *H* (30 *B*)	4 *H*	40 *B*

Figure 2-12 shows the employed model dimensions and boundary conditions, which follows the recommendation by Franke *et al.* (2006) and COST (2007). In the model, *X*-axis represents the main flow direction, while *Y* and *Z* axes represent the transverse and vertical directions, respectively.

Table 2-4 summarizes the employed dimensions compared with those of COST (2007) and Architectural Institute of Japan (AIJ) recommendations (Tamura *et al.* 2008). Commercial CFD package (STAR-CCM+ solver) is utilized to solve the LES represented by Equation 2-12. Dynamic Sub-Grid Scale model by Smagornisky (1963) and Germano *et al.* (1991) is used to account for the turbulence. Parameters used to handle flow quantities as well as the solution technique are summarized in Table 2-6. Inflow field generated by DRFG and

CDRFG techniques is introduced into STAR CCM using space and time-dependent table option (*x*, *y*, *z*, *t*).

$$\frac{\partial \overline{u_i}}{\partial x_i} = 0$$

$$\frac{\partial \overline{u_i}}{\partial t} + \overline{u_j}\,\frac{\partial \overline{u_i}}{\partial x_j} = -\frac{1}{\rho}\frac{\partial \overline{P}}{\partial x_i} + \frac{\partial}{\partial x_j}(-\tau_{ij} + 2\nu \overline{S_{ij}})$$

$$\tau_{ij} = \overline{u_i u_j} - \overline{u_i}\,\overline{u_j}$$

$$\overline{S_{ij}} = \frac{1}{2}\left(\frac{\partial \overline{u_i}}{\partial x_j} + \frac{\partial \overline{u_j}}{\partial x_i}\right)$$

$$\tau_{ij} - \frac{1}{3}\delta_{ij}\tau_{kk} = 2\nu_e \overline{S_{ij}}$$

$$\nu_e = (C_s.\Delta)^2\left(2\overline{S_{ij}}\,\overline{S_{ij}}\right)^2$$

Equation 2-12

where *i*=1, 2, 3 correspond to the *x*-, *y*- and *z*-directions, respectively, The over bar represents the filtered quantities, u_i, *p*, *t*, τ_{ij} and ν represent fluid velocity, pressure, time, the SGS Reynolds stress and molecular viscosity coefficient, respectively. S_{ij}, ν_e, Δ, C_s represent strain rate tensor, eddy viscosity, grid size, Smagorinsky constant which is determined instantaneously based on the dynamic model (Germano *et al.* 1991), respectively. δ_{ij} represents Kronecker delta.

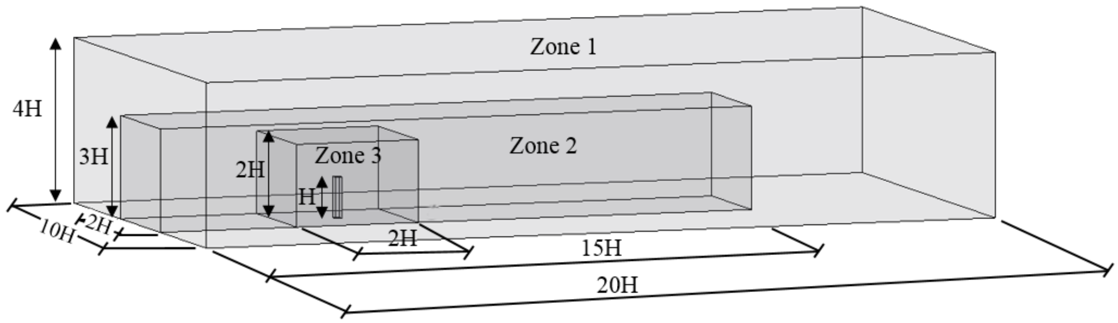

Figure 2-13 Dimensions of different mesh zones

Table 2-5 Properties of the employed grids

Grid	Grid 1 (G1)			Grid 2 (G2)		
	Zone 1	Zone 2	Zone 3	Zone 1	Zone 2	Zone 3
Grid size	H / 10	H / 50	H / 90	H / 10	H / 36	H / 60
Total number of grids	990,000			670,000		

The computational domain is discredited using polyhedral mesh option available in Star CCM+. Two grids sizes G1 and G2 are employed to study the grid independency of the results. For both grids, fine meshes are used near the building faces, the wake zone, and the zone between the inflow and the building. Distribution of the mesh size within computational domain is divided into three zones as illustrated in Figure 2-13and summarized in Table 2-5. Figure 2-14 shows details of the employed grids. COST (2007) and Tominaga *et al.* (2008) suggested that the stretching ratio of the grids in regions of high velocity gradients should be less than 1.3. The use of a high stretching ratio with LES can cause numerical divergence due to the sudden differences in the cut-off wave number of the energy spectrum between resolved and sub-grid modeled scales. In the current study, a number of 10 prism layers with 1.05 stretching is utilized for both grids as indicated in Figure 2-14, following the recommendation by Murakami (1998).

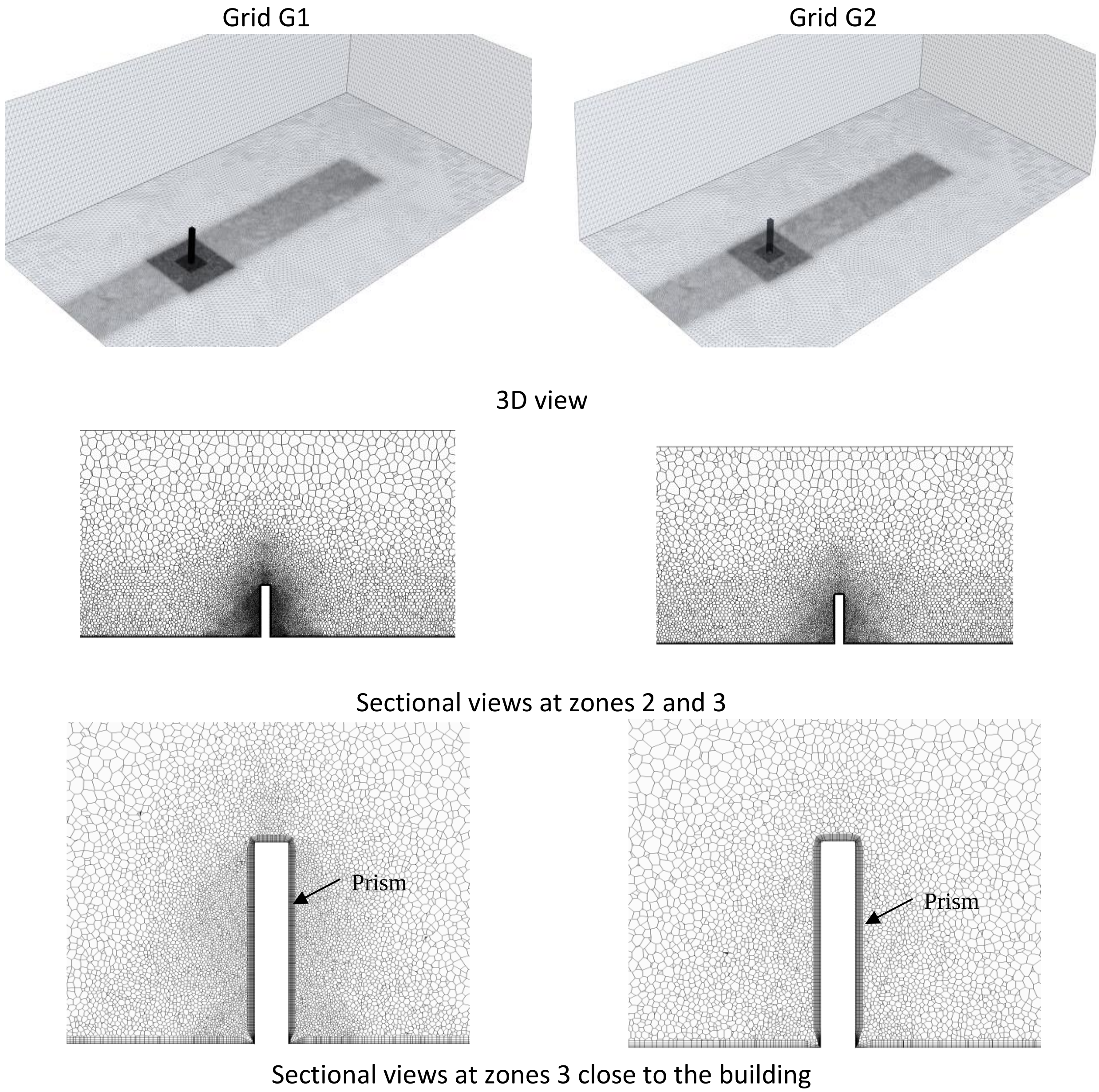

Figure 2-14 Comparison between grids G1 and G2

Time step in the LES is chosen to be equal to 0.0002 sec to maintain Courant Friedrichs-Lewy (CFL) less than 1.0. A number of 30,000 time steps are resolved which represents a 6 sec (i.e. 750 sec in the full scale using a velocity of 10 at the building height or to 3000 sec in the full-scale using a velocity of 40 m/s at the building top). The SharcNet high performance computer (HPC) facility at the University of Western Ontario has been used to conduct the simulations, which employed 128 cores for each grid. Simulation on grid

G1 took 28 hours and on grid G2 took around 19 hours. Results for the last 24,000 time steps are employed in calculating flow statistics and building responses.

Table 2-6 Parameters used in the LES

Parameter	Type
Time discretization	Second order implicit
Momentum discretization	Bounded central difference
Pressure discretization	Second order
Pressure-velocity coupling	Coupled
Under relaxation factors	A value of 0.7 for the momentum and 0.7 for the pressure

2.4.2 Resulting flow field

Figure 2-15 illustrates the instantaneous quasi-streamlines superimposed on the velocity field on a vertical section (passing through mid-building width) and on a horizontal section (passing through mid-building height) resulting from the CDRFG employing G1. The shown quasi-streamlines are generated in 2D plane assuming zero velocities in the perpendicular direction to that plane. As indicated in Figure 2-15, instantaneous field depicts clearly large and small scale turbulent structures at the inflow and near the building walls. Figure 2-16 shows instantaneous surfaces of equal vorticity magnitudes where turbulent structure including various shear layers and horseshoe vortex is captured by the numerical simulation.

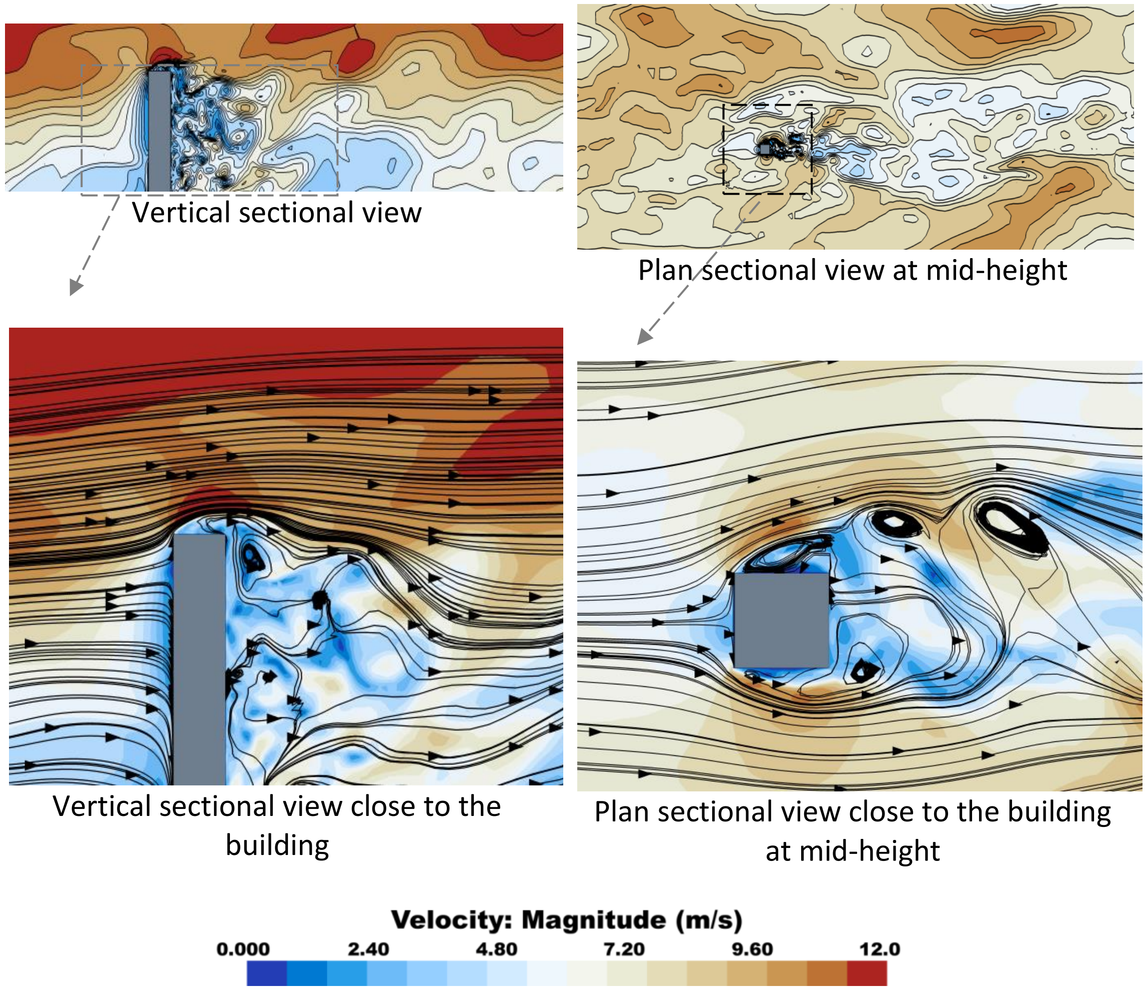

Figure 2-15 Flow field: Instantaneous velocity magnitude and quasi-streamlines

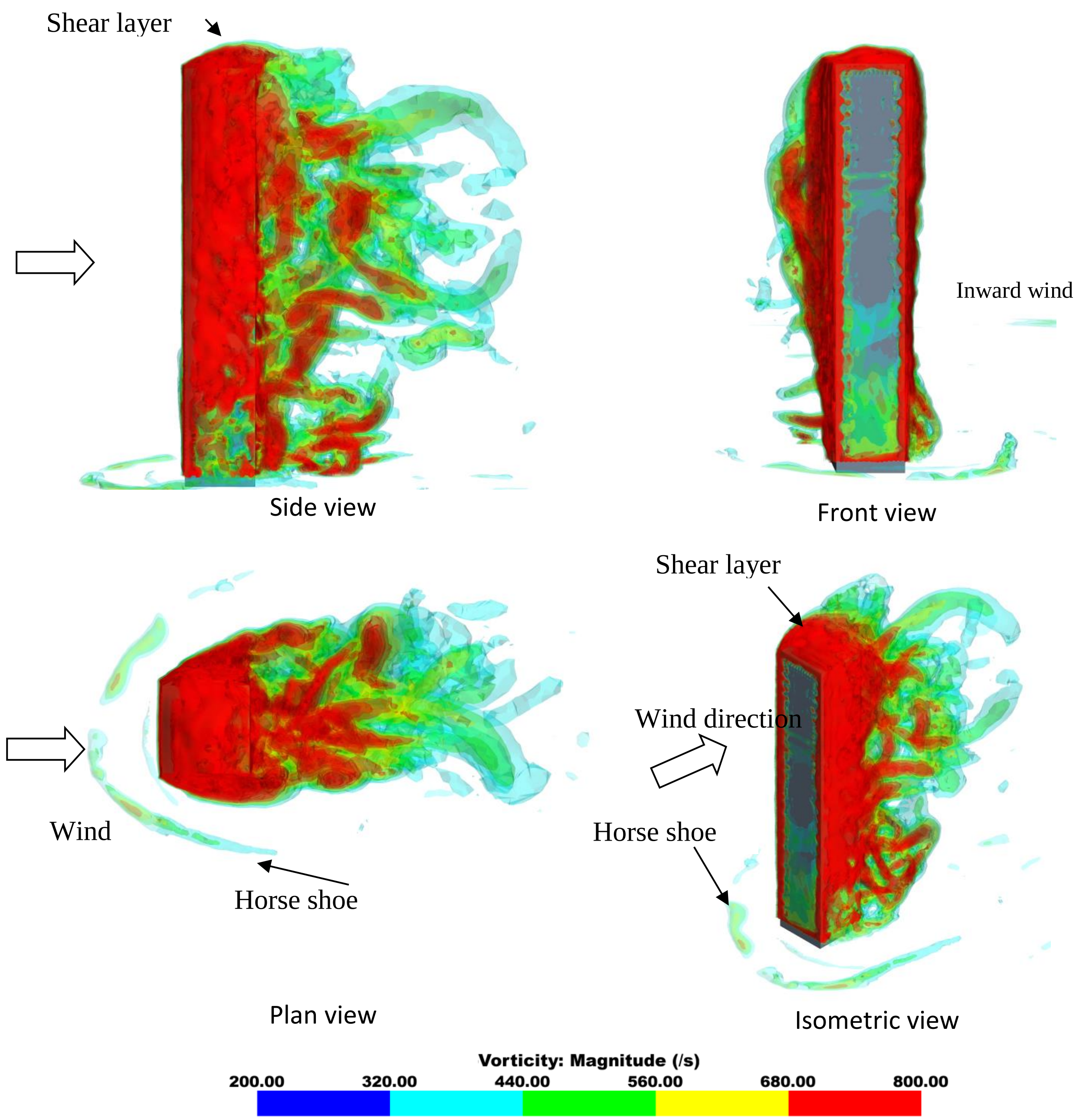

Figure 2-16 Surfaces of equal vorticity magnitude

2.4.3 Resulting building responses

In the current study, dynamic building responses are calculated using wind-induced base moments, similar to the method used for force balance tests in the boundary layer wind tunnel. Figure 2-17 shows time histories of base moments around x-axis (due to across wind force), y-axis (due to along wind force), and z-axis (torsional) obtained from LES using the CDRFG technique and employing grid G1. The shown base moments are normalized using reference base moments defined by Equation 2-13.

$$M_{yref} = \frac{1}{2}\rho V_h^{\ 2} B H^2$$

$$M_{xref} = \frac{1}{2}\rho V_h^{\ 2} D H^2 \qquad \text{Equation 2-13}$$

$$M_{zref} = \frac{1}{2}\rho V_h^{\ 2} D B H$$

where V_h is the mean velocity at the building height and ρ is the air density which is taken equal to 1.25 kg/m^3.

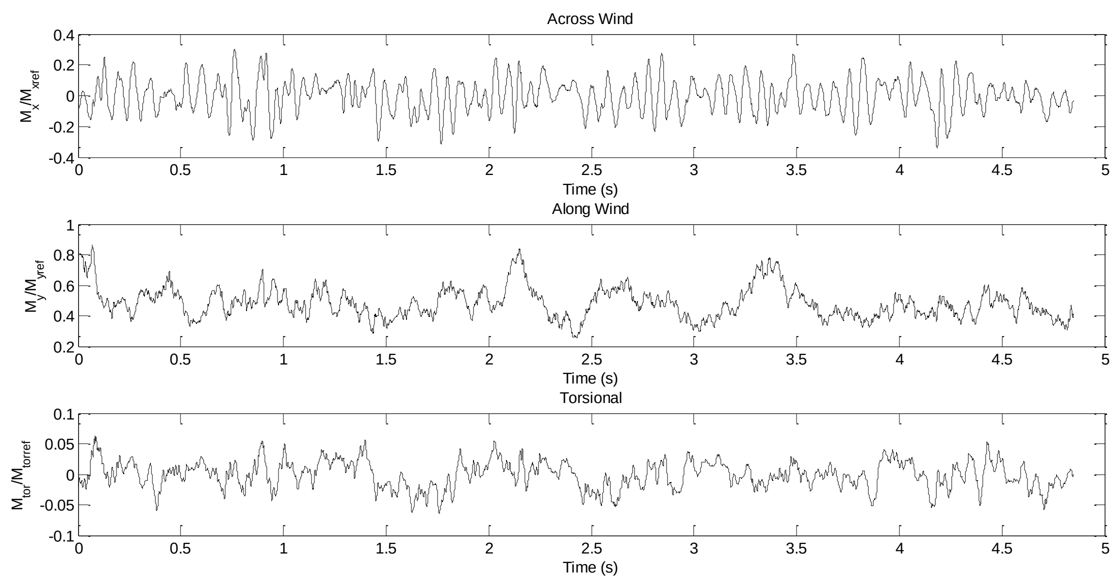

Figure 2-17 Plots for base moments around the x-axis (across wind), y-axis (along-wind) and z-axis (torsional) obtained from LES using CDRFG technique

Power spectral density (PSD), which illustrates the energy distribution with the frequencies, are plotted in Figure 2-18 for the three base moments. This figure shows PSD resulting from LES employing CDRFG on grid G1 and G2, from LES employing DRFG employing grid G1, and from the boundary layer wind tunnel (Zhou *et al.* 2003).

As can be seen from Figure 2-18, PSD resulting from the LES using the CDRFG technique provides very good matching results with the boundary layer wind tunnel in the along wind, across wind and torsional directions. Although PSD for the across wind moment resulting from LES employing DRFG technique is in a good agreement with the boundary layer wind tunnel, PSD for other moment directions (i.e. along wind and torsional) deviates from the boundary layer wind tunnel results. The main reason behind those discrepancies is attributed to the coherency function among the generated velocities. As indicated in Figure 2-2, Figure 2-10 and Figure 2-11, CDRF well maintains the coherency function as the target while it is not the case when DRFG is used. This leads to unrealistic correlated fluctuations of pressure that have frequencies close to the natural frequency of the building. Those unrealistic fluctuations act primarily on the windward face of the building which affect the along wind and torsional base moments and not the across wind base moment.

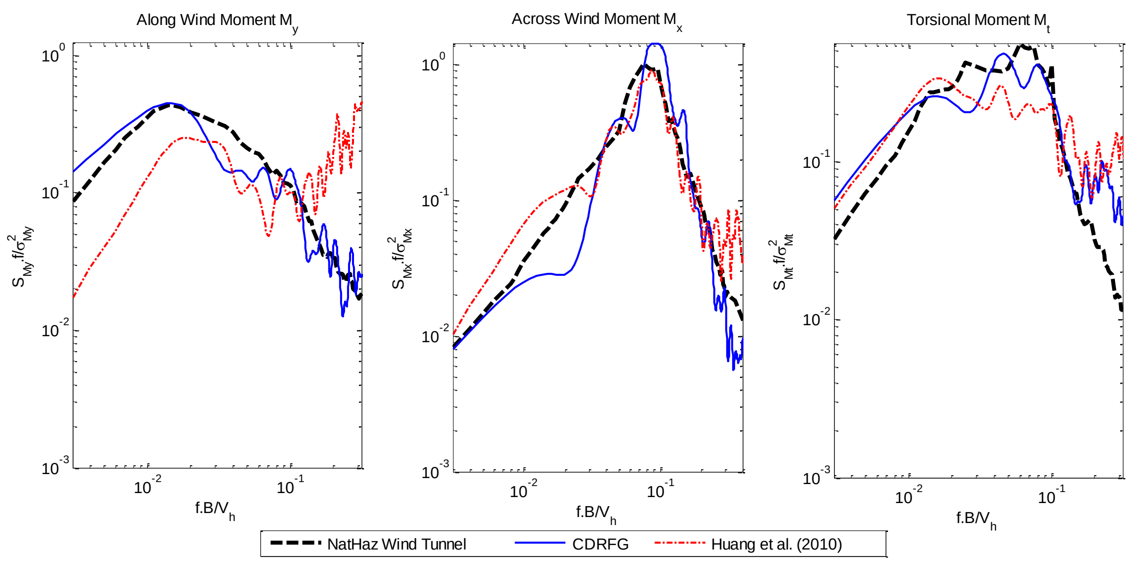

Figure 2-18 Spectra of the base moments

Dynamic responses of the building are evaluated using the base moments' spectra shown in Figure 2-18. The analysis is conducted using the method described by Kijewski and Kareem (1998) and Chen and Kareem (2005) to evaluate peak building's top displacement, top acceleration, and equivalent static base moments. The analysis is conducted to cover a velocity range from 8 to 40 m/s at the building top.

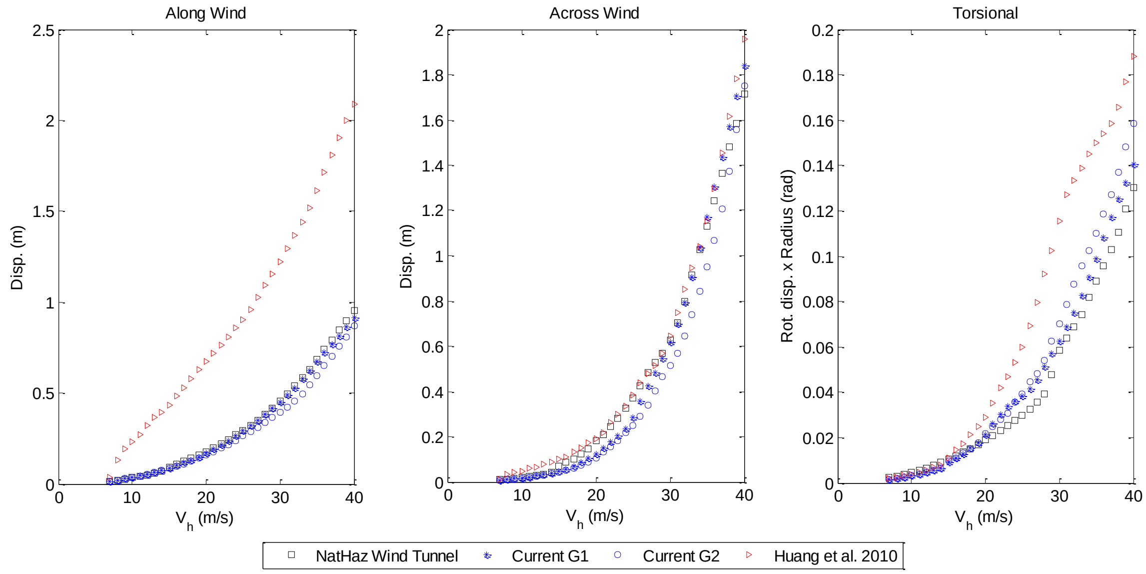

Figure 2-19 Peak top floor displacements

Figure 2-19 and Figure 2-20 show plots of the peak displacement and acceleration at the building top, respectively. Figure 2-21 shows plots of the peak equivalent static moment at the base. In general, similar to the findings observed from the Figure 2-18, Figures Figure 2-19, Figure 2-20 and Figure 2-21 show that responses predicted using LES employing CDRFG technique are in a very good agreement with those from the boundary layer wind tunnel. The same figures also show that responses predicted using LES employing DRFG are in a good agreement for the across wind responses, but are deviated for the along wind and torsional responses. This indicates the advantage of the new CDRFG technique proposed in the current study to analyze wind-induced responses of structures.

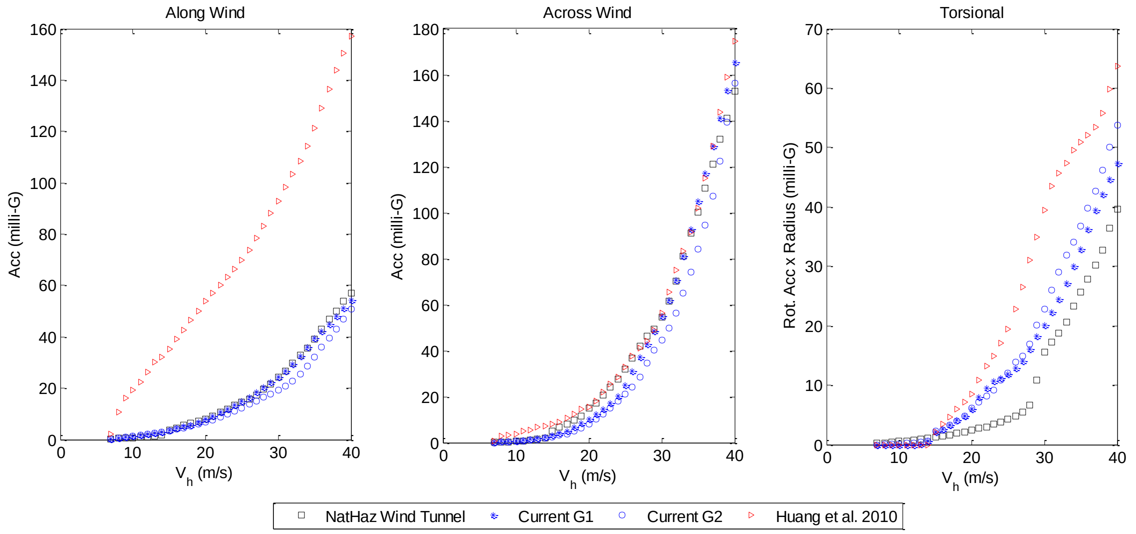

Figure 2-20 Peak top floor accelerations

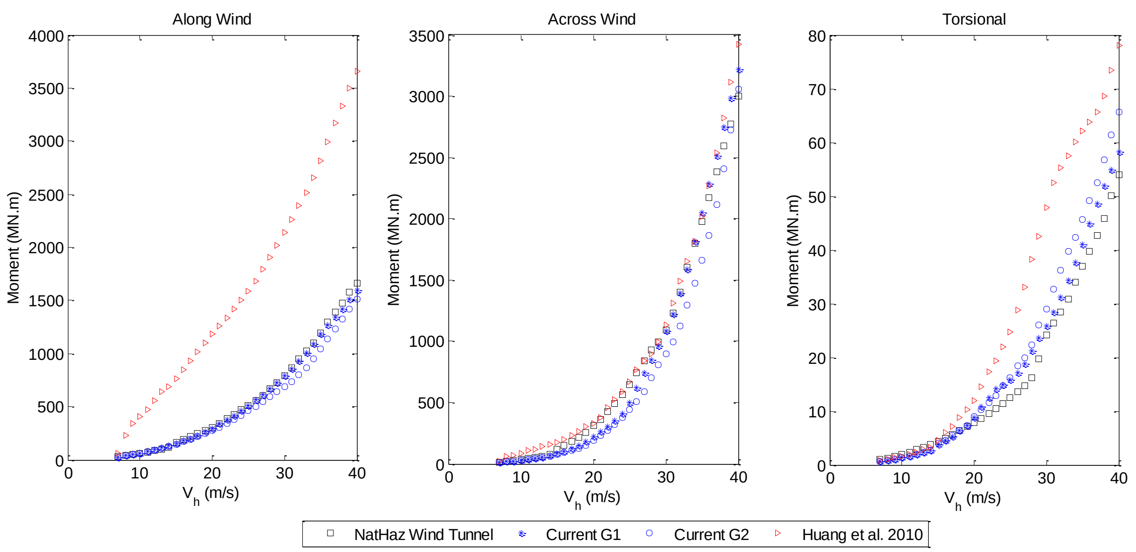

Figure 2-21 Peak base moments

2.5 Conclusions

The current study presented a literature review on inflow turbulence generation approaches for LES, focusing on the unique advantages and some limitations of the discrete random flow generation (DRFG) technique by Huang *et al.* (2010). Two modifications have been proposed to the DRFG technique in the current study to model the proper spectra and the coherency function. The adapted technique is called consistent discrete random flow generation (CDRFG) technique, owing to its consistent spectra and coherency reproduction. Accuracy of the technique in generating proper coherence and spectra is assessed in comparison with target ABL flow statistics form literature. This is followed by assessment of the technique's applicability to evaluate wind-induced responses of structures by comparing base moments and top floor acceleration with force balance data measured in a boundary layer wind tunnel. The results indicate that using CDRFG with LES leads to building' responses that are in a very good agreement with those obtained from the wind tunnel. The results also indicate that CDRFG technique leads to a better matching response to the wind tunnel compared with original DRFG technique especially in the along wind and torsional directions. The CDRFG technique is accurate and amendable for parallel implementation and robust compared with other methods of generating inflows for LES, thus, it is expected to be widely used for wind engineering applications employing LES.

2.6 References

Aboshosha, H., 2014. Response of transmission line conductors under downburst wind, PhD Thesis, University of Western Ontario.

Aboshosha, H., Bitsuamlak, G., El Damatty A. 2015. Turbulence characterization of downbursts using LES. Journal of Wind Engineering and Industrial Aerodynamics, 136, 44–61.

Batten, P., Goldberg, U., Chakravarthy, S. 2004. Interfacing statistical turbulence closures with large-eddy simulation. American Institute of Aeronautics and Astronautics Journal, 42, 485–492.

Bechara, W., Bailly, C., Lafon, P. 1994. Stochastic approach to noise modeling for free turbulent flows. AIAA Journal 32(3), 455–463.

Bitsuamlak, G.T., Simiu, E. 2010. CFD's potential applications: wind engineering perspective. The fifth International Symposium on Computational Wind Engineering, Chapel hill, NC, May 23-27.

Castro, G.H., Paz, R.R., Sonzogni, V.E. 2011. Generation of turbulent inlet velocity conditions for large eddy simulations. Mecánica Computacional, 2275-2288.

Chen, X. and Kareem, A. 2005. Dynamic wind effects on buildings with 3-D coupled modes: application of HFFB measurements. Journal of Engineering Mechanics, ASCE, 131(11), 1115-1125.

COST 2007. Best practice guideline for the CFD simulation of flows in the urban environment COST Action 732.

Dagnew, A., Bitsuamlak, G.T. 2013. Computational evaluation of wind loads on buildings: a review, Wind and Structures, 16(6), 629-660.

Dagnew, A., Bitsuamlak, G.T. 2014. Computational evaluation of wind loads on standard tall building using a large eddy simulation, Wind and Structures, 18(5), 567-598.

Daniels, S.J., Castro, I.P., Xie, Z.T. 2013. Peak loading and surface pressure fluctuations of a tall model building, Journal of Wind Engineering and Industrial Aerodynamics, 120, 19-28.

Davenport, A.G., 1967. Gust loading factors. Journal of Structural Engineering, ASCE, 93(3), 11–34.

Davenport, A.G.1993.How can we simplify and generalize wind loads? Presented at the Third Asia-Pacific Symposium on Wind Engineering, Keynote Lecture, December13–15, Hong Kong.

Engineering Sciences Data Unit (ESDU) 85020. 2001. Characteristics of atmospheric turbulence near the ground. Part II: single point data for strong winds.

Fung, J., Hunt, J., Malik, N., Perkins, R. 1992. Kinematic simulation of homogeneous turbulence by unsteady random Fourier modes. Journal Fluid Mechanics, 236, 281–318.

Franke, J. 2006. Recommendations of the COST action C14 on the use of CFD in predicting pedestrian wind environment. The forth international Symposium on Computational Wind engineering, Yokohama, Japan, July 16-19, 529-523.

Hoshiya, M. 1972. Simulation of multi-correlated random processes and application to structural vibration problems. Proceedings of JSCE, 204, 121–128.

Huang, S.H., Li, Q.S. 2010. Large eddy simulation of wind effects on a super-tall building. Wind and Structures, 13(6), 557-580.

Huang, S., Li, Q., Wu, J. 2010. A general inflow turbulence generator for large eddy simulation. Journal of Wind Engineering and Industrial Aerodynamics, 98, 600-617.

Iwatani, Y., 1982. Simulation of multidimensional wind fluctuations having any arbitrary power spectra and cross spectra. Journal of Wind Engineering. Japan, 11, 5–18.

Gousseau, P., Blocken, B., Stathopoulos, T., van Heijst, G.J.F., 2011. CFD simulation of near-field pollutant dispersion on a high-resolution grid: a case study by LES and RANS for a building group in downtown Montreal. Atmospheric Environment, 45 (2), 428-438.

Germano, M., Piomelli, U., Moin, P., Cabot, W.H. 1991. A dynamic subgrid-scale eddy viscosity model. Physics of Fluids, 3(7), 1760–1765.

Jarrin, N., Benhamadouche, S., Laurence, D., Prosser, R. 2006. A synthetic-eddy- method for generating inflow conditions for large-eddy simulations. International Journal of Heat and Fluid Flow, 27(4), 585–593.

Jiang, Y., Alexander, A., Jenkins, H., Arthur, R., Chen, Q. 2003. Natural ventilation in buildings: measurement in a wind tunnel and numerical simulation with large-eddy simulation. Journal of Wind Engineering and Industrial Aerodynamics, 91(3), 331-353.

Keating, A., Piomelli, U., Balaras, E., Kaltenbach, H.J. 2004. A priori and a posteriori tests of inflow conditions for large-eddy simulation. Physics of Fluids, 16, 4696.

Kraichnan, R. 1970. Diffusion by a random velocity field. Physics of Fluids, 13, 22-31.

Kim, Y., Castro, I.P., Xie, Z.T., 2013. Inflow conditions for Large-Eddy Simulations with incompressible flow solvers. Computers & Fluids, 84, 56–68.

Kijewski T., Kareem A. 1998. Dynamic wind effects: a comparative study of provisions in codes and standards with wind tunnel data. Wind and Structures, 1(1), 77-109.

Kondo, K., Murakami, S., Mochida, A. 1997. Generation of velocity fluctuations for inflow boundary condition of LES. Journal of Wind Engineering and Industrial Aerodynamics, 67-68, 51–64.

Klein, M.A., Sadkiki, Janicka, J., 2003. A digital filter based generation of inflow data for spatially developing direct numerical or large eddy simulations. Journal of Computational Physics, 186, 652–665.

Li, A., Ahmadi, G., Bayer, R., Gaynes, M. 1994. Aerosol particle deposition in an obstructed turbulent duct flow. Journal of Aerosol Science, 25 (1), 91–112.

Lim, H.C., Thomas, T.G., Castro, I.P., 2009. Flow around a cube in a turbulent boundary layer: LES and experiment. Journal of Wind Engineering and Industrial Aerodynamics, 97(2), 96–109.

Liu, K.L., Pletcher, R.H. 2006. Inflow conditions for the large eddy simulation of turbulent boundary layers: a dynamic recycling procedure. Journal of Computational Physics, 219 (1), 1–6.

Lumley, J.L., Panofsky, H.A. 1964. The Structure of Atmospheric Turbulence. Wiley-Interscience, New York, 239.

Lund, T.S., Wu, X., Squires, K.D. 1998. Generation of turbulent inflow data for spatially developing boundary layer simulations. Journal of Computational Physics, 140, 233–258.

Maruyama, T., Morikawa, H. 1994. Numerical simulation of wind fluctuation conditioned by experimental data in turbulent boundary layer. In: Proceeding of the 13th Symposium on Wind Engineering, 573–578.

Murakami, S. 1998. Overview of turbulence models applied in CWE–1997. Journal of Wind Engineering and Industrial Aerodynamics, 74-76, 1-24.

Nozawa, K., Tamura, T. 2002. Large eddy simulation of the flow around a low-rise building in a rough-wall turbulent boundary layer. Journal of Wind Engineering and Industrial Aerodynamics, 90, 1151-1162.

Nozu, T., Tamura, T., Okuda, Y., Sanada, S. 2008. LES of the flow around building wall pressures in the center of Tokyo. Journal of Wind Engineering and Industrial Aerodynamics, 96, 1762- 1773.

Sagaut, P., Garnier, E., Tromeur, E., Larchevêque, L., Labourasse, E. 2003. Turbulent inflow conditions for LES of subsonic and supersonic wall-bounded flows. American Institute of Aeronautics and Astronautics Journal, 42, 469–478.

Smagorinsky, J. 1963. General circulation experiments with the primitive equations, I. the basic experiment. Monthly Weather Review, 91, 99-164.

Shirani, E., Ferziger, J.H., Reynolds, W.C. 1981. Mixing of a passive scalar in isotropic and sheared homogeneous turbulence, Report TF-15, Mech. Eng. Dept., Stanford Univ.

Smirnov, R., Shi, S., Celik, I. 2001. Random flow generation technique for large eddy simulations and particle-dynamics modeling. Journal of Fluids Engineering, 123, 359-371.

Tamura, T. 2000. Towards practical use of LES in wind engineering. Journal of Wind Engineering and Industrial Aerodynamics, 96 (10–11), 1451–1471.

Tamura, T. 2009. Large Eddy Simulation of Building Aerodynamics. The Seventh Asia-Pacific Conference on Wind Engineering, November 8-12, 2009, Taipei, Taiwan.

Tamura, T. 2008. Towards practical use of LES in wind engineering. Journal of Wind Engineering and Industrial Aerodynamics, 96, 1451–1471.

Tamura, T., Nozawa,K., Kondo, K. 2008. AIJ guide for numerical prediction of wind loads on buildings. Journal of Wind Engineering and Industrial Aerodynamics, 96, 1974–1984.

Tamura, T. 2010a. Application of LES-based model to wind engineering-Implementation of meteorological effects. The Fifth International Symposium on Computational Wind Engineering, Chapel hill, NC, May 23-27.

Tamura, T. 2010b. LES for aerodynamic characteristics of a tall building inside a dense city district", The Fifth International Symposium on Computational Wind Engineering, Chapel hill, NC, May 23- 27.

Tominaga, Y., Mochida, A., Yoshiec, R., Kataokad, H., Nozu, T., Masaru Yoshikawa, M., Shirasawa, T. 2008. AIJ guidelines for practical applications of CFD to pedestrian wind environment around buildings. Journal of Wind Engineering and Industrial Aerodynamics, 96(10-11), 1749–1761.

Tominaga, Y., Stathopoulos, T., 2010. Numerical simulation of dispersion around an isolated cubic building: model evaluation of RANS and LES. Building and Environment, 45 (10), 2231-2239.

Tominaga, Y., Stathopoulos, T. 2011. CFD modeling of pollution dispersion in a street canyon: Comparison between LES and RANS. Journal of Wind Engineering and Industrial Aerodynamics, 99(4), 340-348.

Tutar, M., Celik, I. 2007. Large eddy simulation of a square cylinder flow: Modelling of inflow turbulence. Wind and Structures, 10(6), 511-532.

Xie, X.T., Castro. I.P. 2008. Efficient generation of inflow conditions for large eddy simulation of street-scale flow. Flow, Turbulence and Combustion, 81(3), 449-470.

Zhou. Y., Kijewski, T. Kareem, A. 2003. Aerodynamic Loads on Tall Buildings: Interactive Database. Journal of Structural Engineering: ASCE, 3, 394-404.

Chapter 3

3 LES evaluation of wind-induced responses for an isolated and a surrounded tall building

3.1 Introduction

Wind is a governing design load case for flexible structures such as tall buildings. Boundary layer wind tunnel testing has been widely used over the past five decades to evaluate structural design loads and responses. With the recent advancements in the computer technology, Computational Fluid Dynamics (CFD) analysis, particularly those based on Large Eddy Simulation (LES), are becoming useful in many wind engineering applications. For example, LES was utilized by Tominaga and Stathopoulos [1, 2] to study the dispersion around a building and street canyon while Gousseau et al. [3] studied the dispersion in a city center. Jiang [4] and Durrani et al. [5] utilized LES to study the natural ventilation of buildings caused by thermal and pressure forces. Abdi and Bitsuamlak [6] studied the velocity speed up factors resulting from various topographic structures. In applications related to building aerodynamics, many researchers evaluated forces and pressure distribution acting on tall buildings, such as Nozawa and Tamura [7], Huang et al. [8], Tamura et al. [9], and Braun and Awruch [10], Dagnew and Bitsuamlak [11] and Aboshosha et al. [12]. A recently detailed review is provided by Dagnew and Bitsuamlak [13]. This review highlights the different types of turbulence modeling and inflow boundary conditions (IBC) used in literature. These studies showed encouraging results in predicting the forces and mean pressures using LES.

Table 3-1 summarizes the scope and the main findings of previous numerical studies focusing on building responses. As indicated from the table, most of these studies were conducted on isolated buildings where the influence of the surroundings was not considered. It is well-known from experimental wind tunnel engineering that the effect of the surroundings can be significant.

Proper Inflow Boundary Condition is essential for accurate LES modeling of building aerodynamics (Huang and Li [14]; Dagnew and Bitsuamlak [11]). According to the Keating et al. [15] IBC can be generated using three methods (i) precursor database (Bitsuamlak and Simiu [16], Liu and Pletcher [17]), (ii) recycling method (Lund et al. [18]; Nozawa and Tamura [7], Aboshosha et al. [19]), and (iii) synthesizing the turbulence (Kondo et al. [20]; Huang et al. [21]; Smirnov et al. [22]). The first two methods require prior simulations to generate the inflow which can be computationally expensive compared to the synthesizing the turbulence method. Recently, the authors have developed an efficient inflow generator based on synthesizing the turbulence, which is named the Consistent Discrete Random Flow Generator (CDRFG) (Aboshosha et al. [12]). This method is able to properly model the statistical properties of the inflow represented in the turbulent spectra as well as the coherency function, which are very important characteristics for accurate evaluation of building aerodynamics (Davenport [23]; Kijewski and Kareem [24]).

Table 3-1 Scope and the main findings of previous studies focused on building responses

Reference	Turbulence Model	Scope	Findings/ Comments
Nozawa and Tamura (2002) [7]	LES	pressure distribution on low-rise buildings employing the recycling method to generate the inflow	good agreement was found for the peak pressures obtained from the model with those from wind tunnel
Huang et al. (2007) [8]	RANS and LES	aerodynamic behavior of the CAARC building using RANS and LES models	LES with a dynamic sub grid scale (SGS) model lead to satisfactory predictions for mean and dynamic wind loads
Zhang and Gu (2008) [25]	RANS	aerodynamic behavior of buildings with staggered arrangement	good agreement with wind tunnel results in terms of mean pressure, base force and base moment coefficients
Tamura (2008) [9]	LES	employed LES models in different wind engineering applications including tall buildings in a city center	LES model led to encouraging results in terms of base moment spectra

Braun and Awruch (2009) [10]	LES	aeroelastic LES model of the CAARC building	good agreement was found with other experimental and numerical predictions in mean pressures, however lesser agreement was found in the rms pressures
Dagnew and Bitsuamlak (2014) [11]	LES	effect of various inflow conditions on the aerodynamic behavior of the CAARC building	good agreement with experimental results was found for LES model adopting fluctuations generated using the synthetic IBC
Aboshosha et al. (2015a) [12]	LES	developing a new turbulence inflow generator for LES evaluation of tall building aerodynamic responses	very good matching between the results from the numerical model and the wind tunnel was found, indicating the importance of consistent inflow turbulence generation.

Dagnew and Bitsuamlak [29] attempt to simulate wind load for a building immersed in the city but did not produce good comparison with the wind tunnel data. This was primarily due to the computational resource limitations and the quality of the adopted inflow turbulence generation technique. These non-satisfactory results motivated the authors to develop a new IBC technique [12], which was assessed using an isolated building. The current study builds on the findings of that previous research to assess the pressure distributions and building responses of a tall building located in a complex surrounding. The Commonwealth Advisory Aeronautical Research Council (CAARC) building is considered. This building is used by many researchers to calibrate and validate wind tunnel experiments and numerical models, such as in Wardlaw and Moss [30] and Melbourne [31]. Results of the wind tunnel conducted by Dragoiescu et al. [32] are used to validate the LES model.

The study is divided into five sections. In section 1 (this section), an introduction on the previous LES studies on tall buildings is presented. Section 2 briefly describes the CDRFG technique used for synthesizing the IBC for the sake of completeness. In section 3, details about the wind tunnel experiment conducted by Dragoiescu et al. [32] are provided. Section 4 describes the LES model utilized to predict the forces and responses of the CAARC building. In Section 5, the LES results and discussions are provided and comparisons are made with the corresponding values from the wind tunnel experiment and other numerical simulations from the literature, whenever applicable.

3.2 Inflow turbulence generation

Inflow boundary condition is generated using the Consistent Discrete Random Flow Generator (CDRFG) technique. Details of that technique, including a Matlab source code, are provided in Aboshosha et al. [12], however, a brief description of the method is presented here for completeness. The steps illustrated by the flow chart given in Figure 3-1 are followed.

- In Step 1, mean velocity, turbulence intensity, and turbulence length scale profiles measured from the wind tunnel are fitted to the power law profiles. Table 3-2 summarizes the flow characteristics including: mean velocity, turbulence intensity and length scale profiles in addition to the coherence function. Figure 3-2 shows the profiles measured from the wind tunnel compared to those used in the LES. As indicated in Figure 3-2, the LES profiles match with the wind tunnel profiles with an average regression coefficient of 0.94.

- In Step 2, the characteristic distance D required is taken equal to $H/2$ to properly model the correlations along the building height [12].

- In Step 3, the frequency range is divided into number of segments (M) and within each segment, random frequencies are selected where the number of those selected frequencies are (N). In the present study, the turbulent spectra divided into M =100 segments, with N=50 random frequencies $f_{m,n}$ within each segment. More details can be found in Aboshosha et al. (2015). Frequencies in the range from 1.0 to 100 *hz* are used to represent the spectra, which means that the frequency step Δf is taken equal to 1.0 *hz*.

- In Step 4, von Karman (ESDU [33]) spectra, defined by Equation 3-1, is used to obtain the $p_i^{m,n}$ and $q_i^{m,n}$ parameters.

$$S_u = \frac{4(I_u U_{av})^2 (L_u / U_{av})}{\left(1 + 70.8(fL_u / U_{av})^2\right)^{5/6}}$$

$$S_v = \frac{4(I_v U_{av})^2 (L_v / U_{av})\left(1 + 188.4(2fL_v / U_{av})^2\right)}{\left(1 + 70.8(2fL_v / U_{av})^2\right)^{11/6}} \qquad \text{Equation 3-1}$$

$$S_w = \frac{4(I_w U_{av})^2 (L_w / U_{av})\left(1 + 188.4(2fL_w / U_{av})^2\right)}{\left(1 + 70.8(2fL_w / U_{av})^2\right)^{11/6}}$$

where L_u, L_v and L_w are the length scales of turbulence in the along-wind, across-wind, and vertical directions, respectively, and are shown in Figure 3-2.

- In Step 5, random numbers using $p_i^{m,n}$ and $q_i^{m,n}$ to maintain the divergence free criterion are generated.

- In Step 6, the turbulent velocity field are evaluated for the three velocity components.

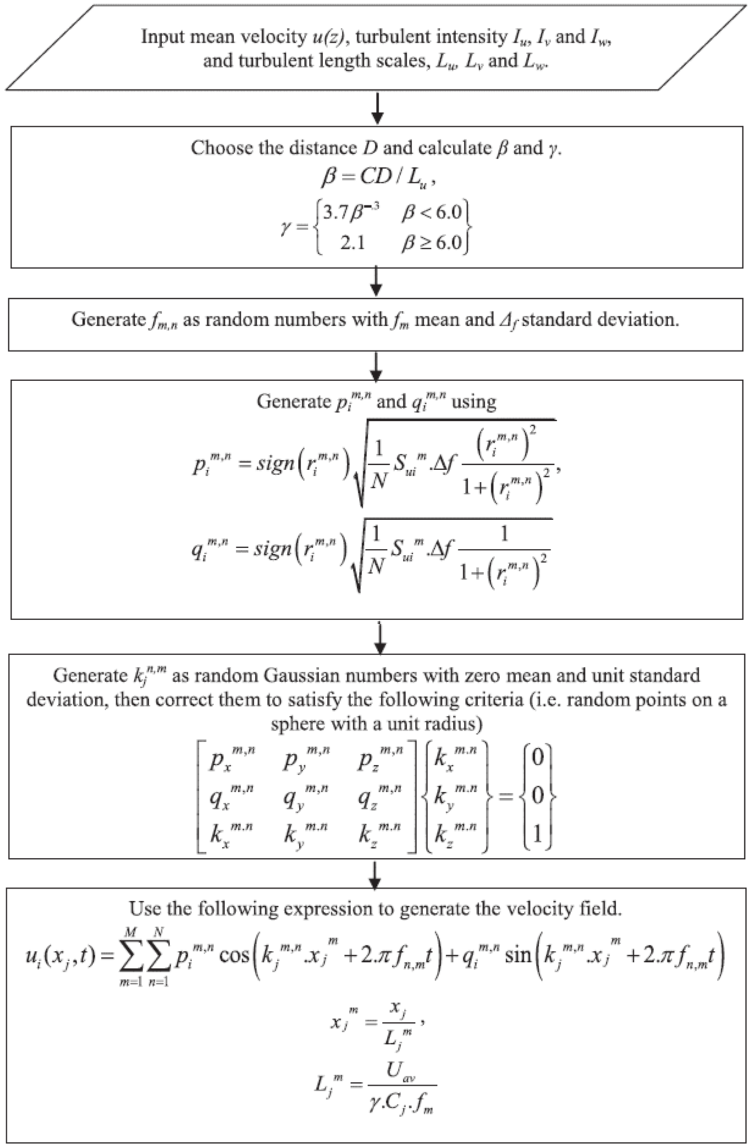

Figure 3-1 CDRFG technique flow chart (Aboshosha et al. [12], reproduced with permission)

Table 3-2 Parameters used for generating velocity field

Parameter	Definition	Value(s)
Exposure	Open terrain	
Mean velocity U_{av}	$U_{av} = U_{av\,ref}\left(\frac{z}{z_{ref}}\right)^{\alpha}$	$U_{av\ ref} = 10\ m/s$ $z_{ref} = 0.4562\ m$ $\alpha = 0.17$
Turbulent intensity *I*	$I_j = I_{refj}\left(\frac{z}{z_{ref}}\right)^{-dj}$	$I_{refj} = 0.197,\ 0.167,\ 0.145$ and d_j = 0.232, 0.154, 0.007 in the *u*, *v* and *w* directions, respectively. (Zhou et al. [34]; ESDU [33])
Length scale	$L_j = L_{refJ}\left(\frac{z}{z_{ref}}\right)^{\varepsilon_j}$	$L_{refJ} = 0.563,\ 0.147,\ 0.186\ m$ and ε_j = 0.133, 0.154, 0.178, in x, y, z directions respectively
Coherency function	$Coh(f_m) = \exp\left(-\frac{C_j f_m dx_j}{U_{av}}\right)$ (Davenport [23])	C_j is coherency decay constant
Frequency parameters		$f_{m\,min}$=1.0 hz *M* =100 $f_{m\,max}$ = 100 hz *N*=50 Δ_f=1.0 hz

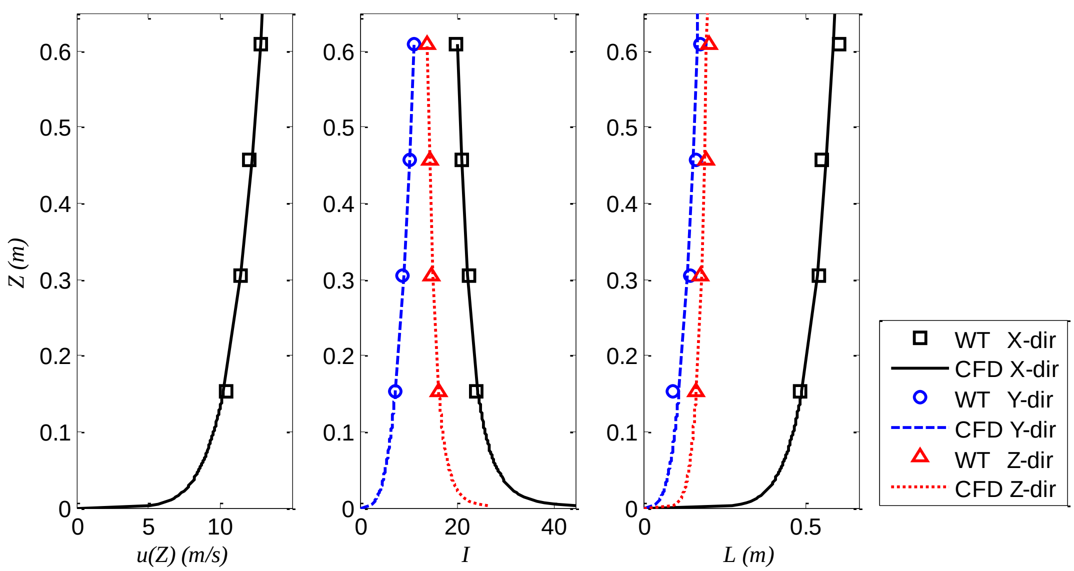

Figure 3-2 profiles measured from the wind tunnel and the fitted profiles for CFD

3.3 Boundary layer wind tunnel test description

For validating the LES model, an experimental wind tunnel test was conducted by Dragoiescu et al. [32] to simulate the wind flow around the CAARC building using a length scale of 1:400. The building has an open upwind terrain condition defined by Table 3-2. The building was tested at Rowan Williams Davies and Irwin (RWDI) Inc.'s wind tunnel and used for the present work after a permission from RWDI. The wind tunnel testing section was of 2.6 m width and 2.1 m height. Two configurations are chosen in the current study: Configuration 1 for isolated building, and Configuration 2 for the building with surroundings (i.e. in a large city center). The two configurations are shown in Figure 3-3 The full-scale dimensions are 30.5 m width, 45.7 *m* depth and 182.5 *m* height. The High Frequency Pressure Integration method is used to characterize the loads on the building. A number of 280 pressure taps is used as indicated in Figure 3-4.

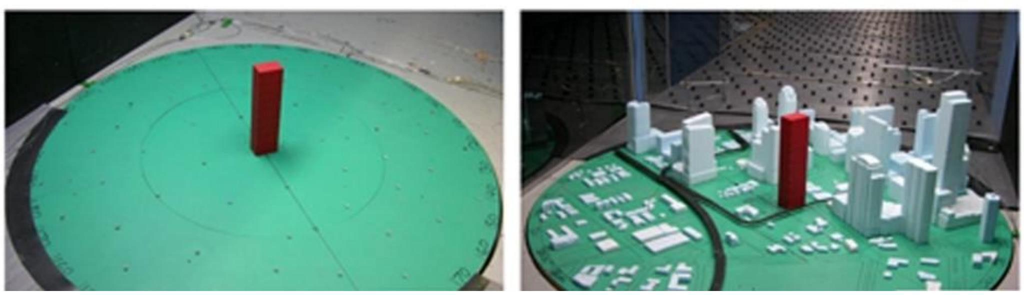

Figure 3-3 Wind tunnel test configurations (Dragoiescu et al. [32], reproduced with permission)

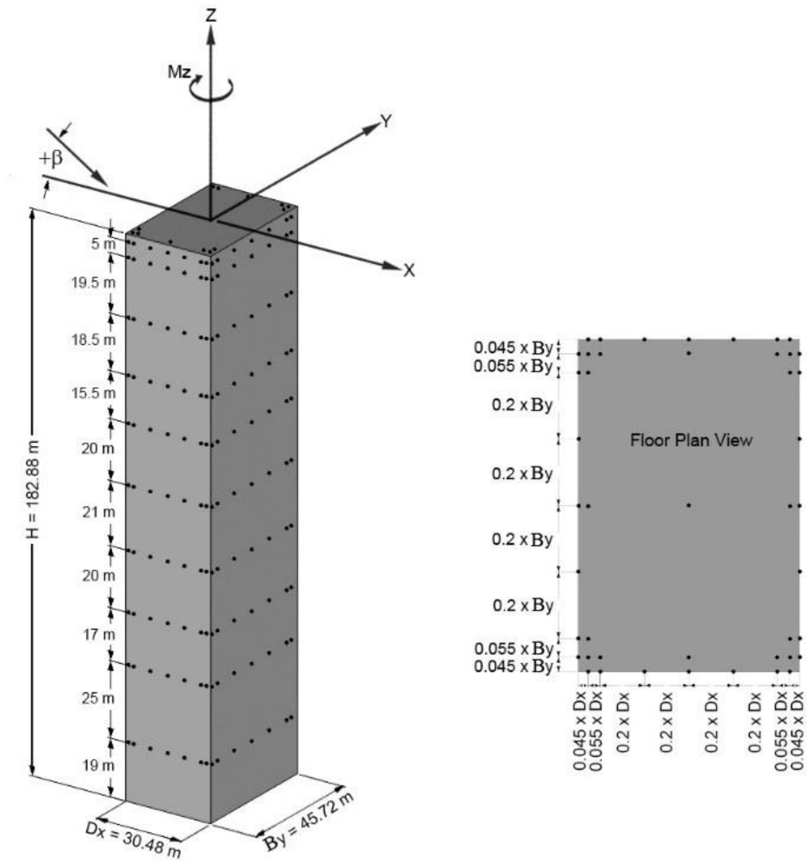

Figure 3-4 CAARC standard full-scale dimensions and pressure tap locations

3.4 Large eddy simulation models

3.4.1 Computational domain dimensions and boundary conditions

Similar to the wind tunnel, a scaled LES model is conducted with length and time scales of 1:400 and 1:100. A mean wind velocity of 10 *m/s* at the building height as indicated in Figure 3-2a is used. Computational domain employed for the LES is chosen based on the recommendation of COST [35], Frank [36] and Dagnew and Bitsuamlak [13], as shown in Figure 3-5. The figure shows also the boundary conditions employed where CDRFG technique is utilized to generate turbulent inflow used in the IBC. The inflow boundary condition utilizes a database for each velocity component depending on both location and time (e.g. u_x (x, y, z, t)), which is previously generated using CDRFG technique. The sides and the top of the computational domain are assigned as symmetry plane boundary condition, which extrapolates the parallel velocity and pressure components in the adjacent cell using reconstruction gradients and develop zero shear stress at the symmetry plane. The bottom of the computational domain and all buildings' faces are defined as no-slip walls, where the tangential velocity component is set to zero. The simulations are conducted using a commercial CFD package (STAR-CCM+ v.9.04) [37] employing LES with dynamic sub-grid scale model by Smagornisky [38] and Germano et al. [39]. Parameters used in the simulations to handle flow quantities and the solution method are summarized in Table 3-3. In order to maintain the convergence and the accuracy of the solution, Courant Friedrichs-Lewy (CFL) is maintained less than 1.0 by setting the time step to be 0.0005 *sec* (i.e. maximum CFL ~ 0.5 at the top of the building). Each simulation is resolved for 14,000 time steps representing 7 seconds in model-scale (i.e. 11.5 minutes in full-scale). The simulations are conducted using the SharcNet [40] high performance computer (HPC) facility at the Western University. The duration required for each numerical simulation performed on 128 processors is 5 hours for grid G1 and 11 hours for grid G2.

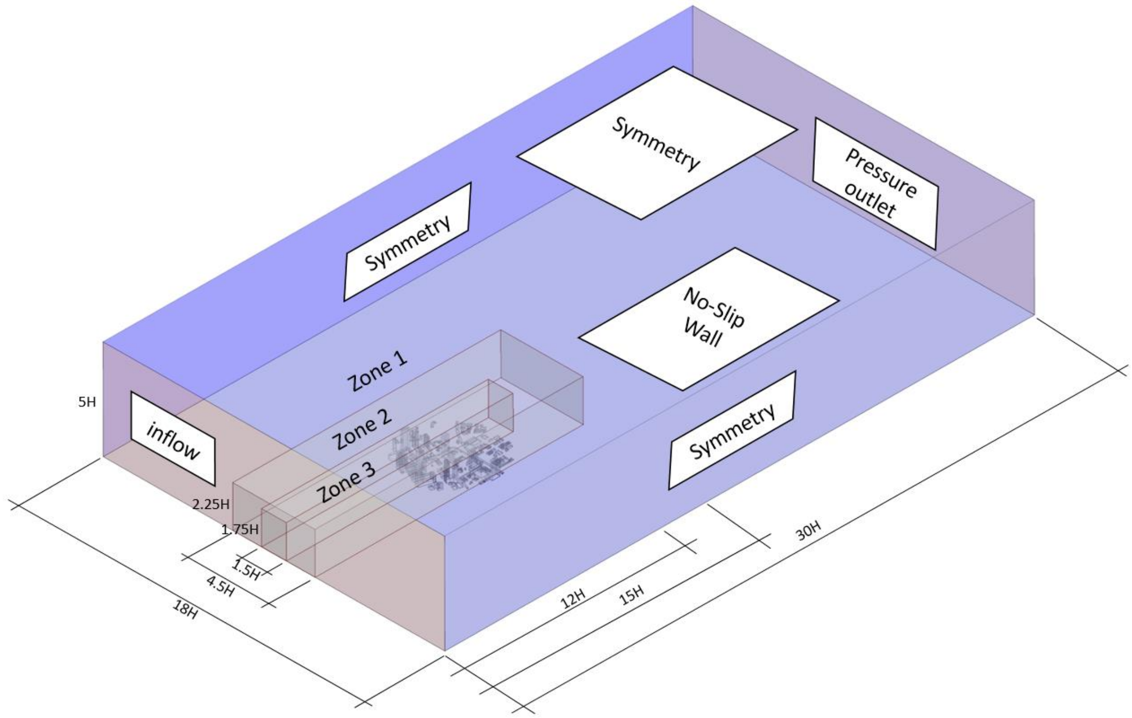

Figure 3-5 Computational domain dimensions and boundary conditions

Table 3-3 Parameters used in the LES

Parameter	Type
Time discretization	Second order implicit
Momentum discretization	Bounded central difference
Pressure discretization	Second order
Pressure-velocity coupling	Coupled
Under relaxation factors	A value of 0.7 for the momentum and pressure

3.4.2 Grid Discretization

The computational domain is discretized using polyhedral control volumes. Two grid resolution G1 and G2 are used for the isolated building configuration to check the grid independency as shown in Figure 3-6. For the second configuration with surrounded building, one grid size (G1*) is used as shown in Figure 3-7. Properties of the three grids are summarized in Table 3-4. Each grid is divided into three zones as illustrated in Figure 3-5. Zone 1 is located away from the building of interest where the grid size is maximum.

Zone 3 is located close to the building of interest and its surroundings. Grid size in this zone is decreased to capture important details of flow structures in the wake zone and the front zone between the IBC and the building. A number of 15 prism layers parallel to the building surfaces with stretching factor of 1.05 is utilized in zone 3 satisfying the recommendations by Murakami [41], COST [35] and Tominaga et al. [42]. Zone 2 is chosen in between zones 1 and 3 and has an intermediate grid size. Four simulation cases are considered in the current study that is summarized in Table 3-5. Cases 1 and 2 simulate the isolated building (Configuration 1) using grid G1 and G2, respectively, for a zero angle of attack (AOA) (i.e. wind is perpendicular to the 45.7 *m* wide wall). Case 3 simulates the isolated building for a 90^{o} angle of attack (i.e. wind is perpendicular to the 30.5 *m* wide wall). Case 4 simulates the surrounded building (Configuration 2) for a 90^{o} angle of attack.

Table 3-4 Properties of the employed grids

Grid	G1			G2			G1*		
	Zone 1	Zone 2	Zone 3	Zone 1	Zone 2	Zone 3	Zone 1	Zone 2	Zone 3
Grid size	H / 10	H / 20	H / 50	H / 10	H / 30	H / 70	H / 10	H / 20	H / 50
Total number of cells	880 000			1 510 000			1 920 000		

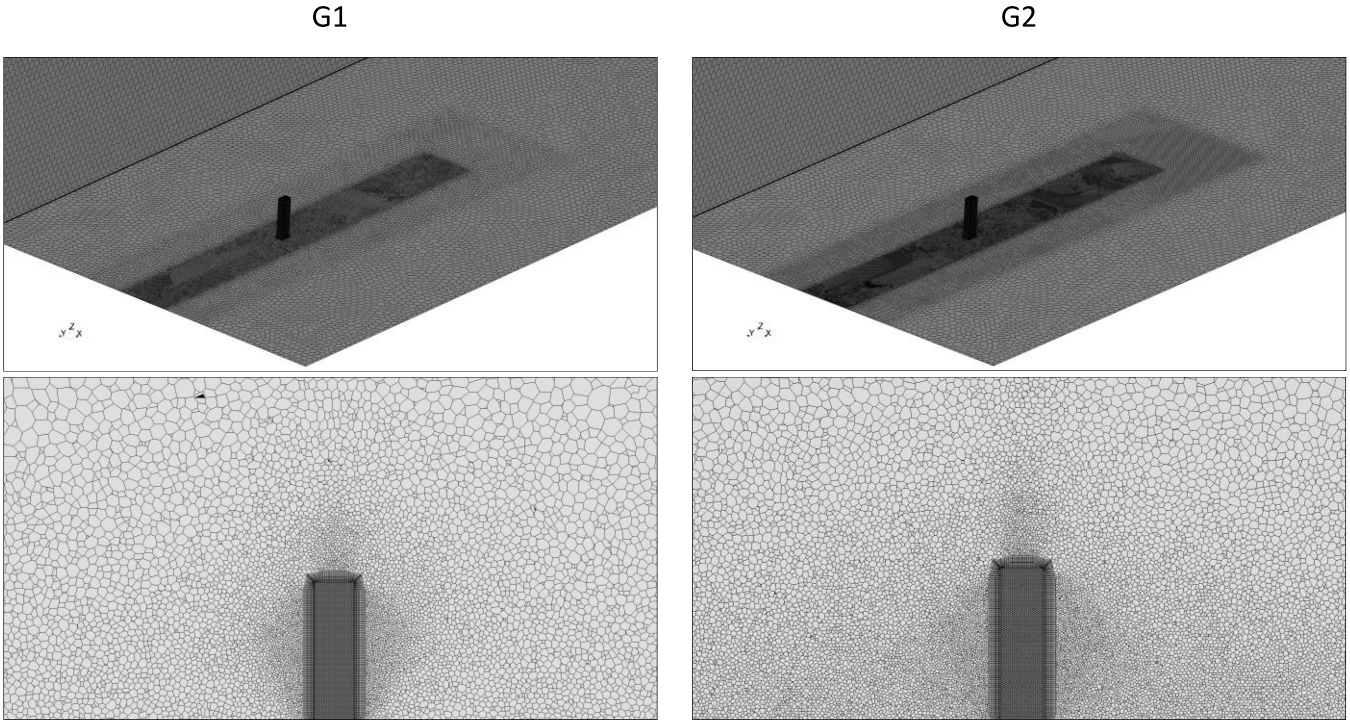

Figure 3-6 Comparison between grids G1 and G2 (Configuration 1 – isolated case)

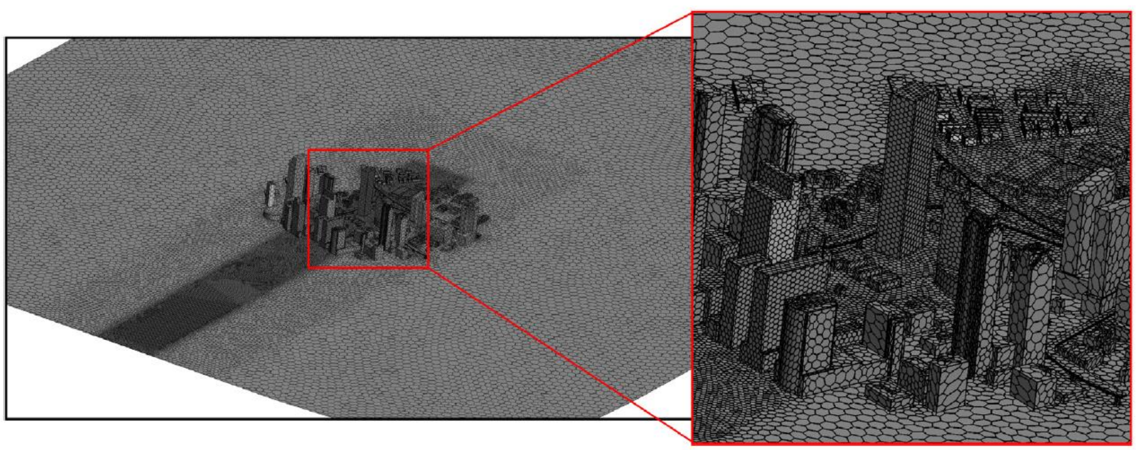

Figure 3-7 Grid G1* used for the surrounded building model (Configuration 2 –complex surrounding).

Table 3-5 Grid size, wind angle of attack and building configuration for the study cases

Case number	Grid	Wind angle of attack	Configuration
Case 1	G1	0^o	1
Case 2	G2	0^o	1
Case 3	G1	90^o	1
Case 4	G1*	90^o	2

3.5 Results and discussions

3.5.1 Wind Flow Field

Figure 3-8 shows the instantaneous velocity contour plot for 90^o wind angle of attack for isolated (Case 3) and surrounded (Case 4) configurations. As demonstrated by the figure, approaching velocity field in the surrounded case varies from the isolated case due to the presence of other structures in front of the study building. The complex flow field in Case 4 demonstrates that the neighboring structures change the characteristics of the upcoming wind as it approaches the study building. The presence of the surrounding structures results in complex flow interference such as channeling and wake effects on the study building. Figure 3-9 shows the instantaneous vorticity contours, which indicates the development of flow vortices caused by the flow separations at sharp corners of the buildings. The figure illustrates the different in aerodynamic behavior and vortices formation between isolated and surrounded building cases. Figure 3-10 shows the instantaneous quasi-streamlines (i.e. projected on 2D plane) superimposed on the velocity field on a horizontal section (passing through mid-building height) and on a vertical section (passing through mid-building width). Figure 3-10 shows the time averaged (mean) of the instantaneous quasi-streamlines. As shown in this figure, the flow is symmetric around the isolated configuration (Case 3), while the channeling effect around the surroundings deviated the flow from symmetry in the surrounded configuration (Case 4).

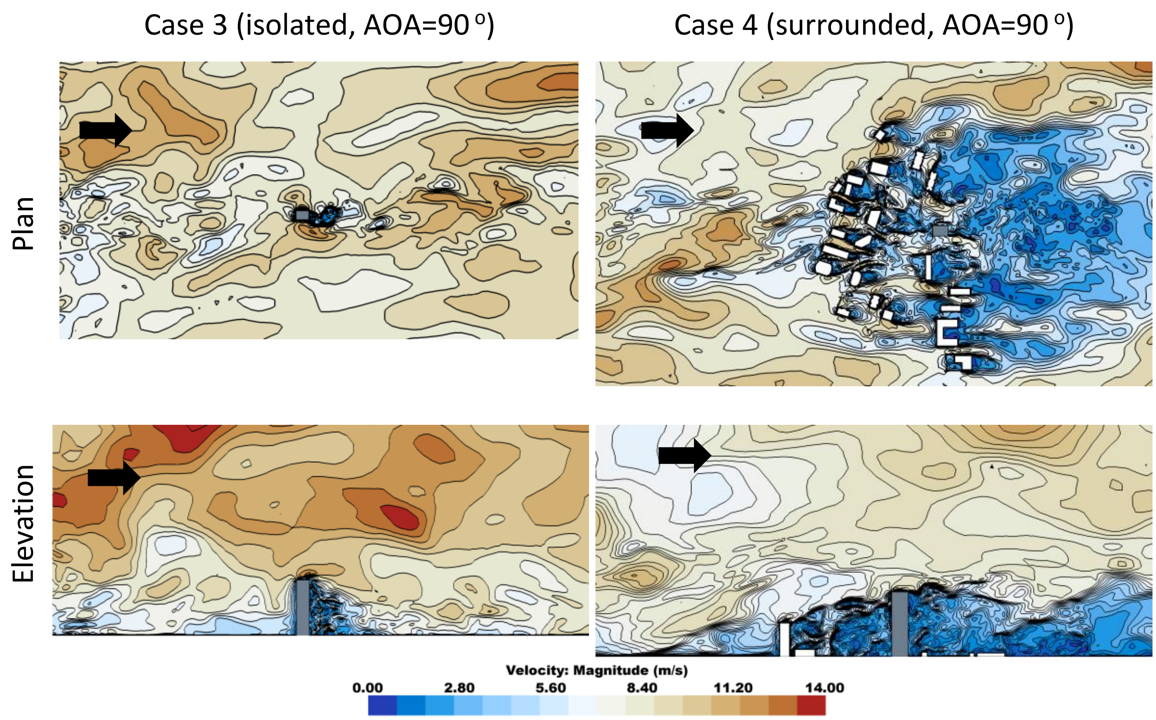

Figure 3-8 Instantaneous velocity magnitude contours

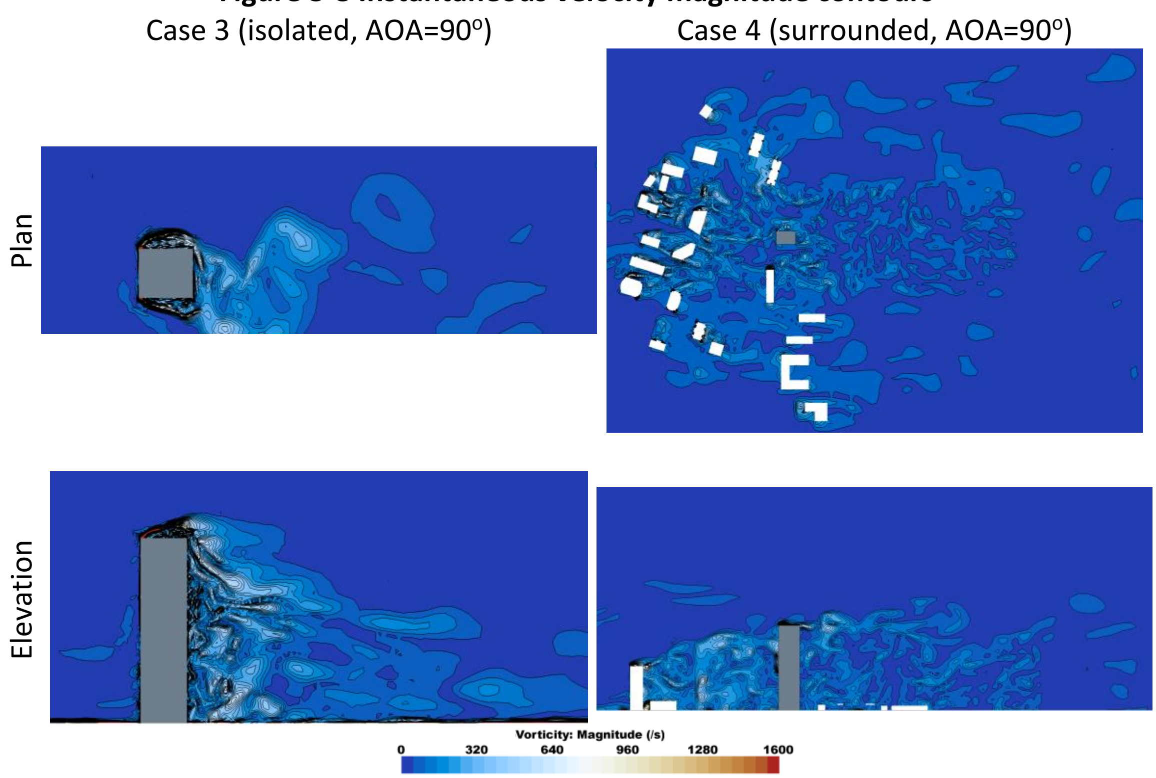

Figure 3-9 Instantaneous vorticity magnitude contours

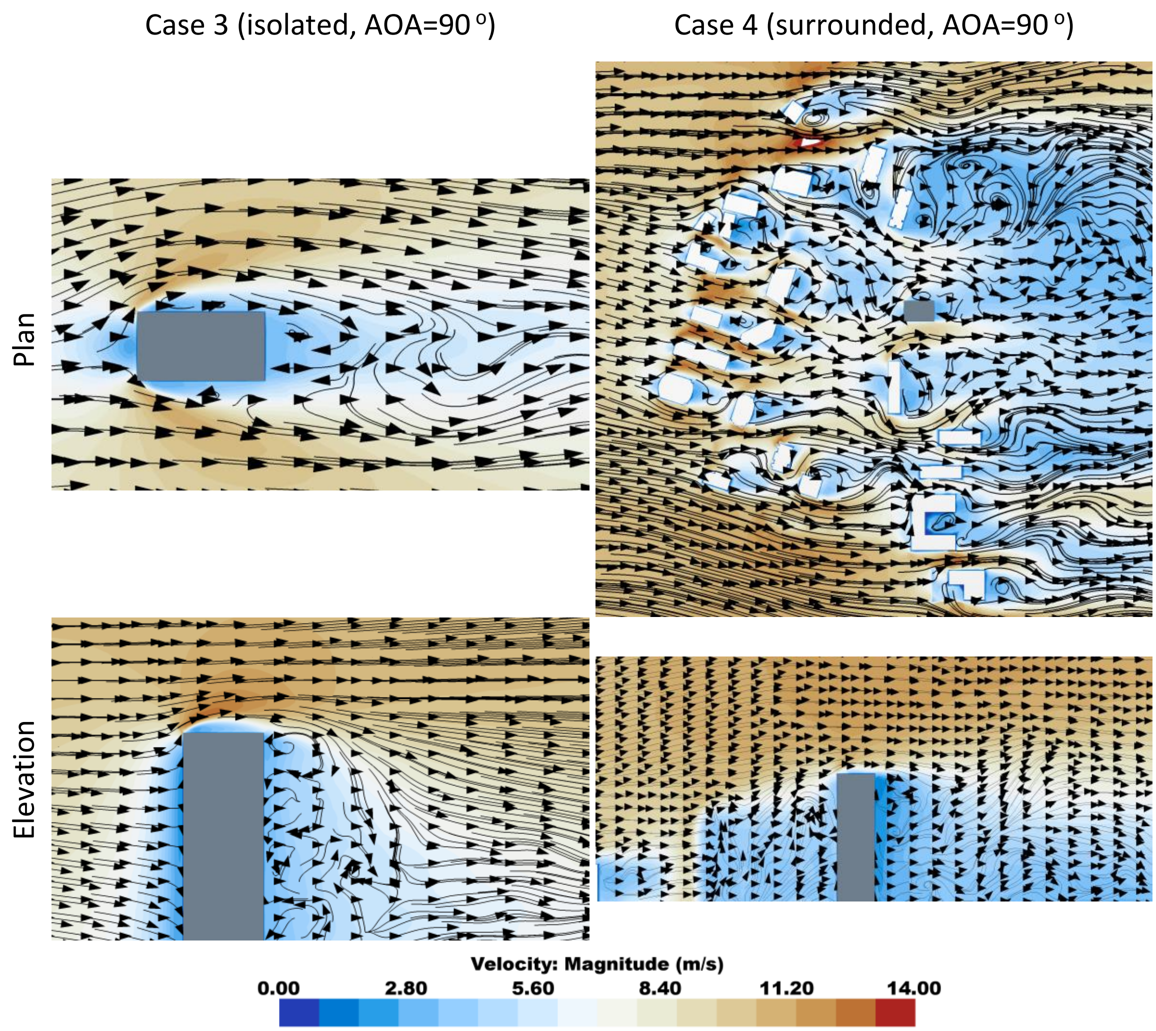

Figure 3-10 Mean velocity magnitude and quasi-streamlines

3.5.2 Mean and rms pressure coefficient distributions

Figure 3-11 shows the mean pressure coefficients (C_p) distribution across a horizontal section at 2/3 of the building height compared with the experimental results obtained from the BLWT testing (Dragoiescu et al. [32]) and similar simulations from the literature (Huang et al. [8]; Dagnew and Bitsuamlak [11]). The C_p is evaluated using Equation 3-2. For the LES, the reference pressure is taken at a point on the inlet boundary at the building height. While in the experimental testing, the reference pressure is taken at the building height measured by the pitot-tube installed at the building height upwind of the turntable, as shown in Figure 3-3.

$$C_P = \frac{P - P_o}{\frac{1}{2}\rho v_H^2} \qquad \text{Equation 3-2}$$

where v_H is the reference velocity at the building height, ($P - P_o$) is the dynamic pressure head, ρ is the air density and H is the height of the study building.

As indicated in this figure, there is a very good agreement between the mean C_p distributions resulted from the present LES and literature with those from the BLWT on both windward and leeward faces (i.e. ~ 2% on average). For the side faces, where the separation occurs, the current study provides also close pressure results to the BLWT measurements (i.e. ~ 3 % on average). It is noticed that the maximum difference in mean C_p between the LES and the experimental results located in the side faces, where the difference reached 12%. By comparing the mean pressures resulting from the current study and other numerical simulations, it appears that the LES model employed in the current study leads to a better matching results with the BLWT for the leeward and side faces. Figure 3-12 shows the distribution of the root-mean-square (rms) C_p at the horizontal section at 2/3 of the building height resulted from the numerical and experimental results. The rms C_p distribution resulted from the current LES model has a better agreement with the BLWT measurements than other the numerical simulations from the literature (i.e. ~

4% on average). Six experimental tests were reported by Melbourne (1980) using different boundary layer and turbulence flow spectra. These tests include: University of Bristol, England; the City University, England; Monash University, Australia; National Aeronautical Establishment (NAE), Canada; and National Physical Laboratory (NPL), England. Figure 3-13Figure 3-14compare the mean and rms C_p values on the front, back and side faces at 2/3 H obtained from the current study and those six experiments, respectively. Although the mean Cps seem to agree well, variations are observed on the rms Cps. These variations can be attributed to differences in the boundary conditions used by the various experiments considered for the comparison.

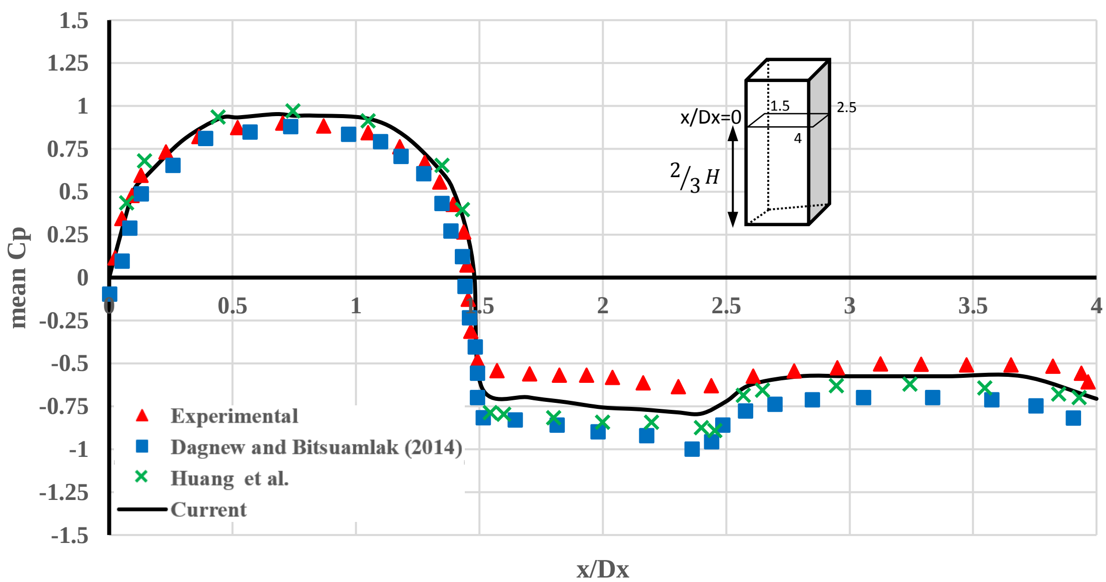

Figure 3-11 mean C_p distribution over horizontal section of the building

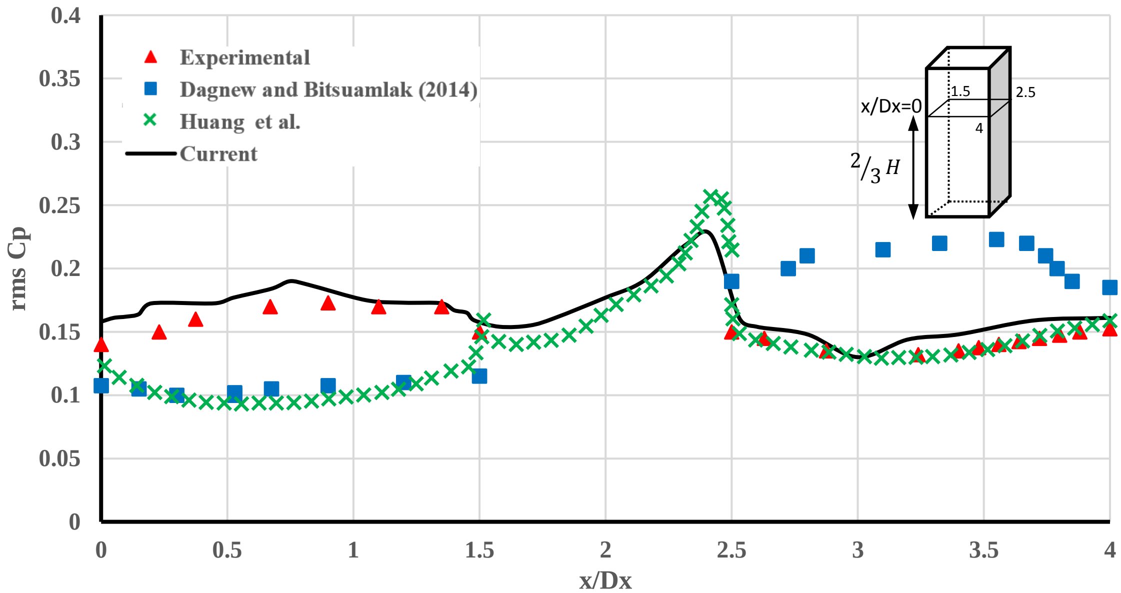

Figure 3-12 rms C_p distribution over horizontal section of the building

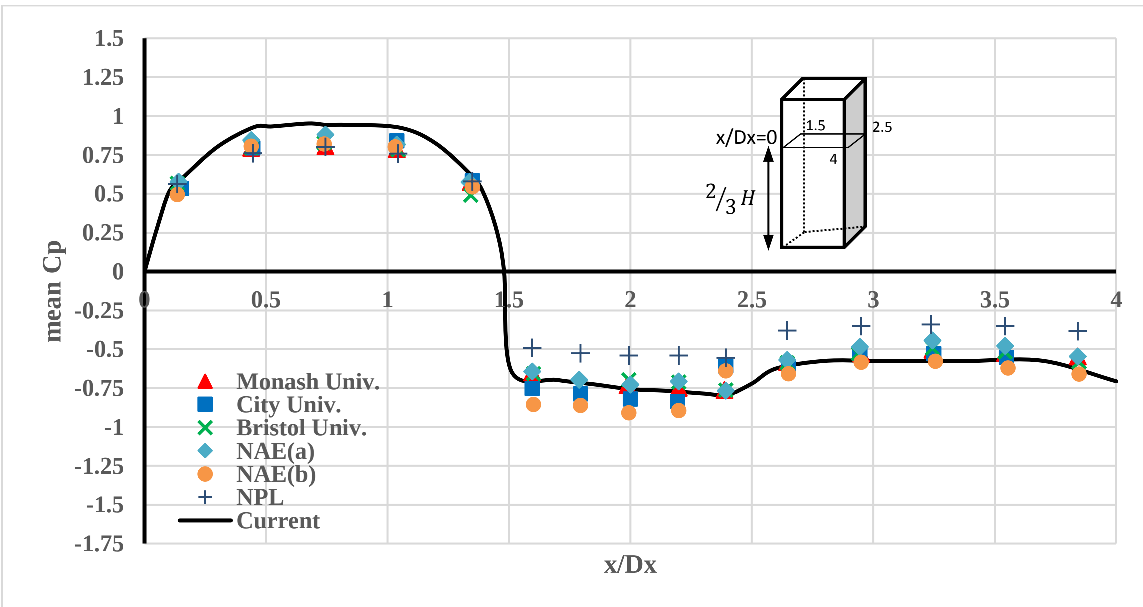

Figure 3-13 Comparing mean C_p distribution of current study with BLWT from literature

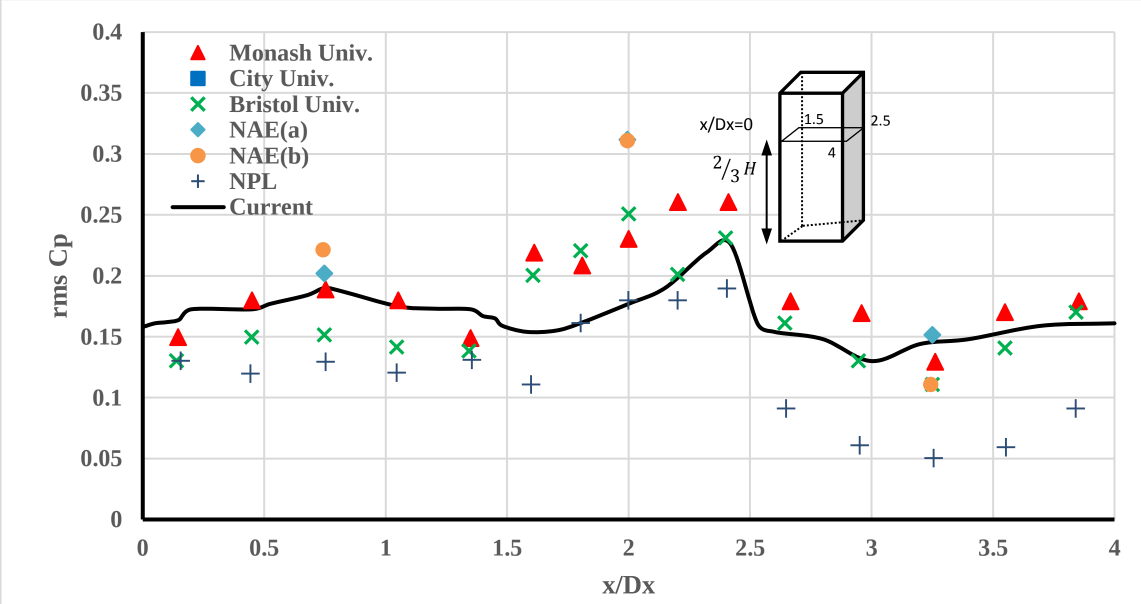

Figure 3-14 Comparing rms C_p distribution of current study with BLWT from literature

Figure 3-15 shows the contour plots of mean C_p on front and lee faces of the building resulting from the current study and from other numerical and experimental studies in the literature. Figure 3-16 shows the contour plots of rms C_p on front and lee faces of the building resulting from the current study and from the literature. The LES work conducted by Dagnew and Bitsuamlak [11] adopted three different techniques for inflow generation. Inflow-1 utilized the spectral synthesizer method developed by Smirnov et al. [22], Inflow-2 utilized the recycling method developed by Lund et al. [18] and Inflow-3 utilized the synthesized turbulence developed by Huang et al. [21]. It is noticed that the stagnation point in the current numerical study is slightly shifted upward compared to the experimental results. This is believed to be due to discrepancy in the simulated frequency range. In the experimental work done by Dragoiescu et al. [32] the BLWT was able to simulate most of the higher frequency range while missing some of the lower frequencies (i.e. large eddies) due the physical limitation of the test section. Whereas the numerical simulations, this lower frequency range is captured, which will lead to a better simulation for larger wind eddies that may affect the location of the stagnation point. Pressure distributions from the current studies match with the experimental results better than those from the literature despite the present use of a coarser grid resolution. The differences are estimated to be 4% in mean C_p and 9% in rms C_p. It is believed that these differences can be further reduced by employing finer grids near the region of interest. Particularly, the good agreement of the rms C_p on the front face is a good indication of the inflow generator quality used in the present study. This indicates the importance of proper modeling of wind statistical properties (i.e. spectra and coherency) of the IBC. As discussed earlier, those statistical properties are maintained by employing the CDRFG technique in generating the inflow, which seems to be the main advantage of the current simulation over other numerical simulations. It worth mentioning that the rms C_p distribution appears to be unsymmetrical along the vertical centerline of both the front and the back faces. Although, the maximum difference between the two half-faces doesn't exceed 6% for LES and 3% for the BLWT generated rms C_p, respectively. The LES difference can be attributed to the slight unsymmetrical grid employed in the analyses. It should also be mentioned that the use of many contour levels and the very narrow range of the rms C_p values (i.e. only from 0.15 to 0.21) could exaggerate the non-symmetry visually as well.

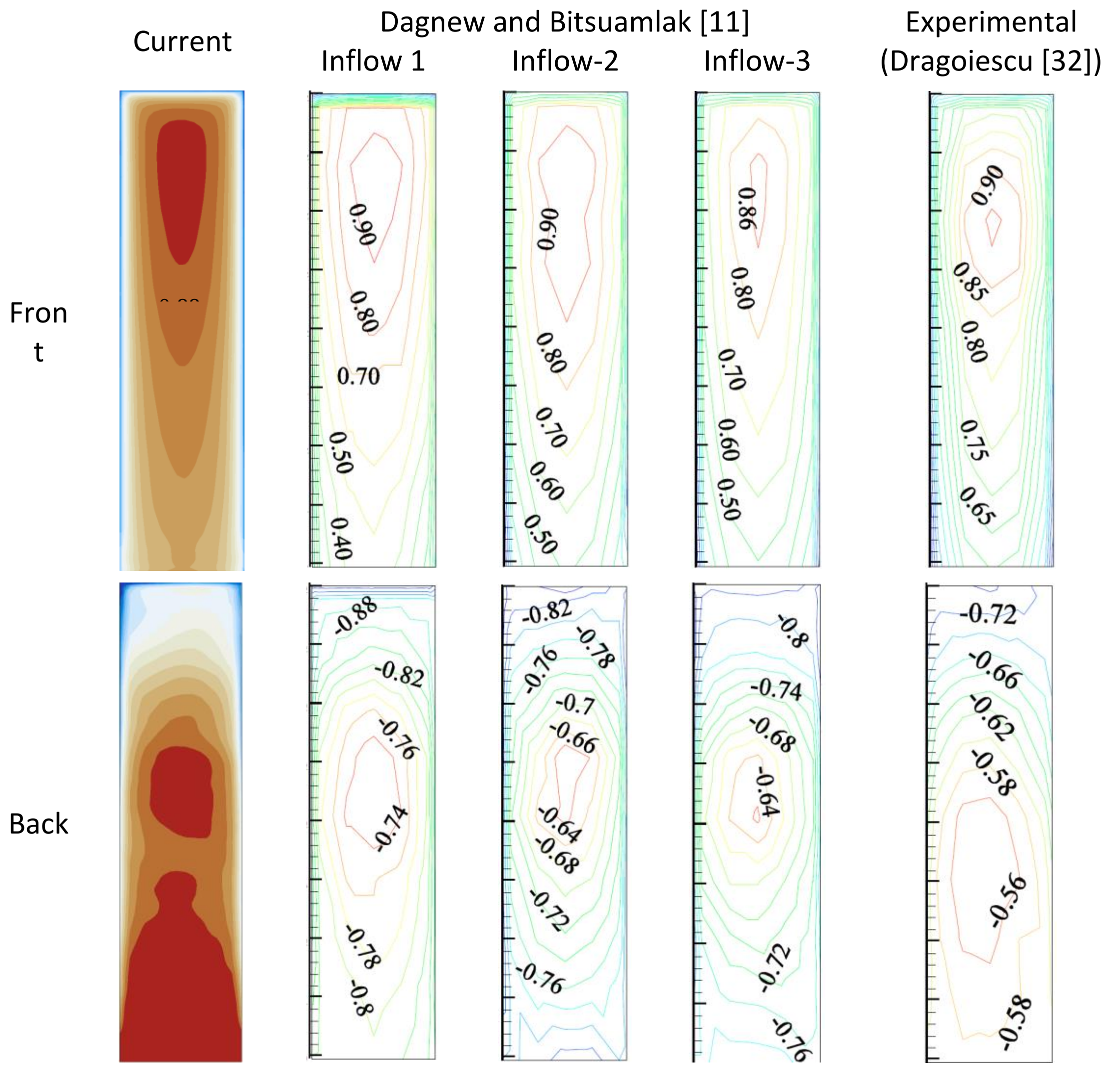

Figure 3-15 Contour distribution of mean C_p over front and back faces of CAARC building obtained from current study and literature

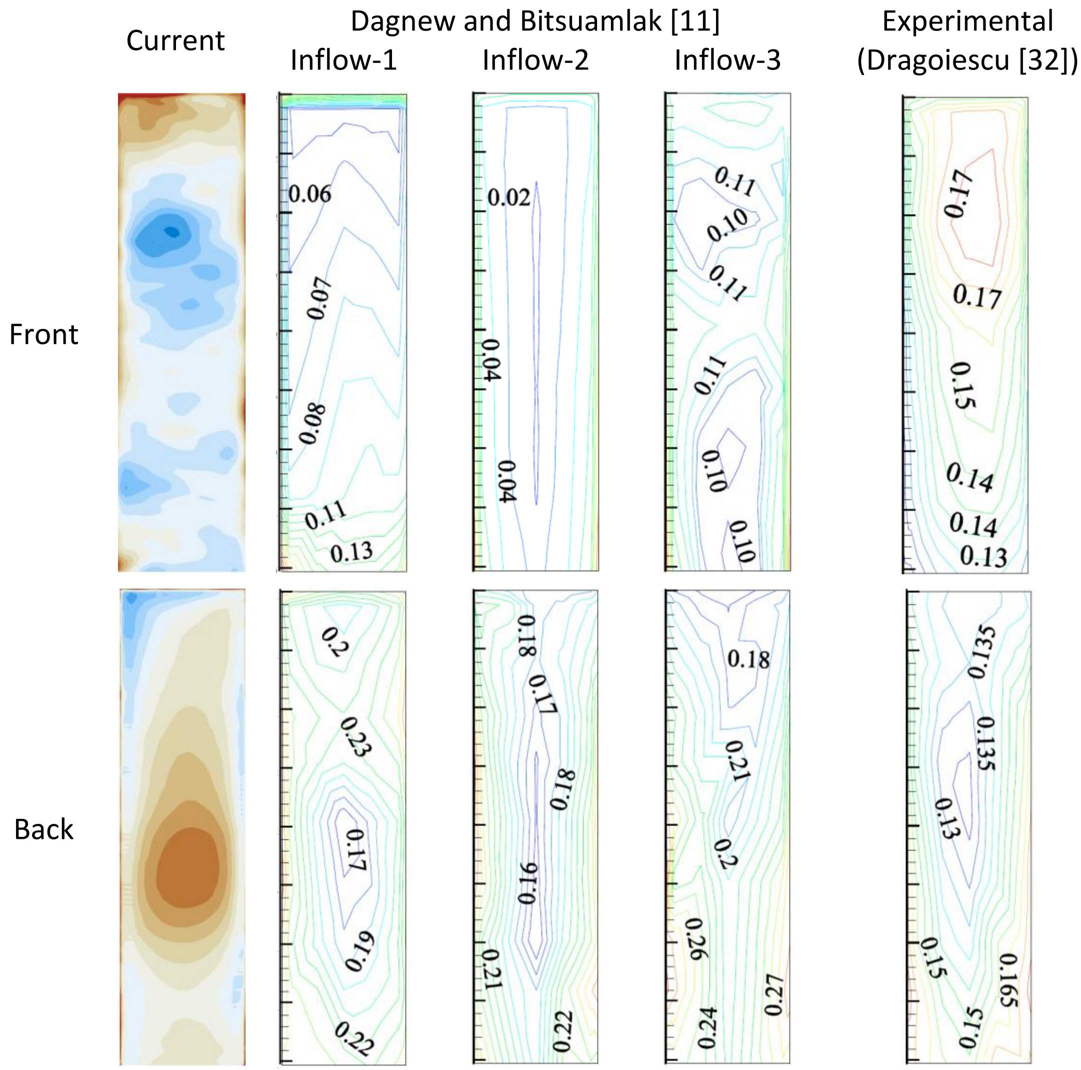

Figure 3-16 Contour distribution of rms C_p over front and back faces of CAARC building obtained from current study and literature

Figure **3-17** shows the mean C_p distribution on the building faces for the isolated (Case 3) and the surrounded (Case 4) building configurations. By comparing the mean C_p for the isolated and the surrounded building configurations, it is noticed that the neighboring structures significantly changed the pressure distribution on the building. The surrounded building experiences a sheltering effect as it is located in the urban canopy developed from the interference between wakes of the surrounding upstream buildings. This leads to unsymmetrical distribution of the mean C_p for the surrounded building configuration compared to the symmetric distribution for the isolated case. Moreover, the absolute mean pressure values for the surrounded configuration is found to be lower than the values of the isolated configuration (i.e. 50% or more), which agrees with the findings of Kim et al. [43]. Figure 3-18 shows the distribution of the rms C_p for the two configurations. For the surrounded building configuration, the rms pressure values is higher than those in isolated configuration (i.e. 40% on average), which reflects the higher turbulence in the surrounded case resulted from the presence of other surrounding structures. Those surrounding structures act as an additional roughness affecting the upcoming wind.

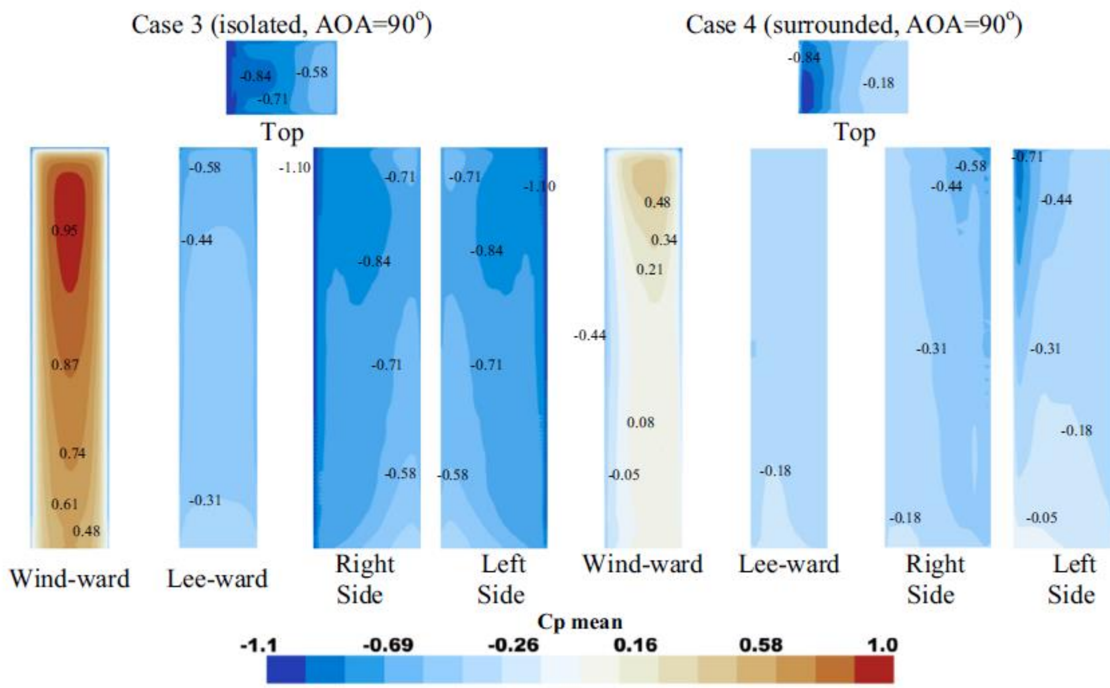

Figure 3-17 mean pressure coefficient distribution over building faces

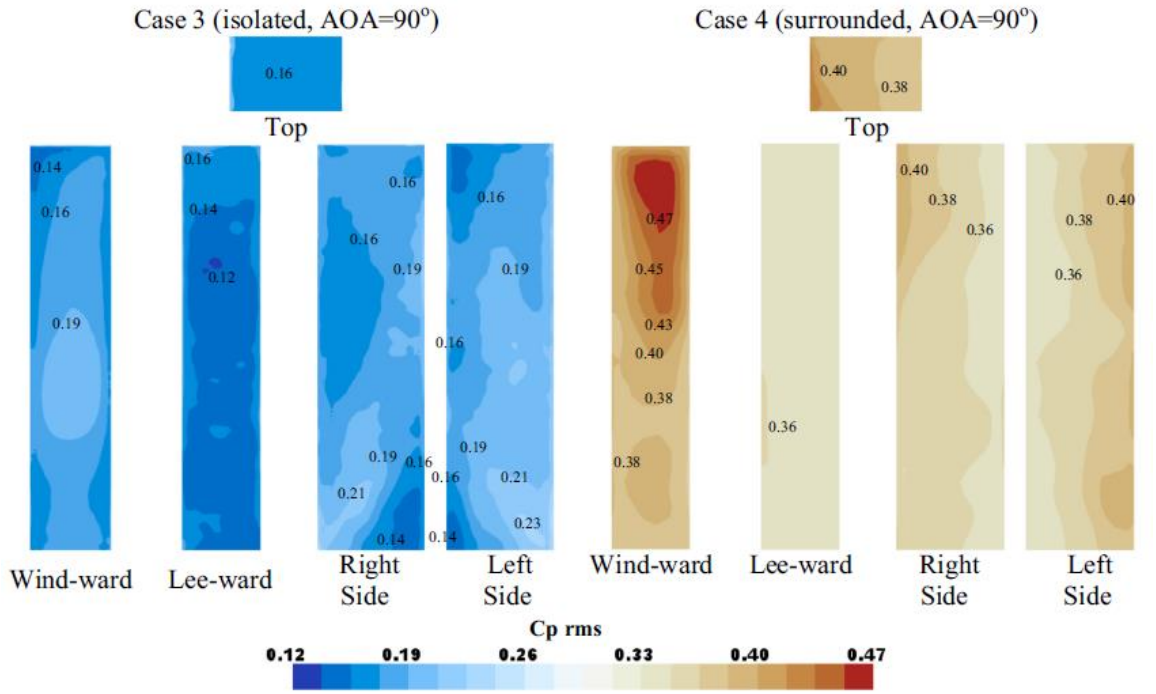

Figure 3-18 fluctuating pressure coefficient (rms) distribution over building faces

3.5.3 Building Responses

In order to calculate the building responses and wind-induced base moment spectra, the building base moment time histories are obtained from the LES for different cases. Figure 3-19 shows the time histories of the base moments obtained, where base moments around x, y and z-axis are in the along-wind, across-wind, and torsional directions. The base moments are normalized using Equation 3-3. It is noted that lower along-wind moments are developed in the surrounded configuration compared to the isolated configurations. This decrease in the longitudinal moments for the surrounded configuration results from the sheltering of surrounding structures located in the upstream of the study building. Concerning across-wind moments, higher values are developed in the surrounded configuration compared to the isolated ones. The rise in across-wind moments, for the surrounded configuration, is caused by the increase in wake buffeting resulted from upstream buildings.

$$M_{yref} = \frac{1}{2}\rho V_h^{\,2} B_y H^2 \quad M_{xref} = \frac{1}{2}\rho V_h^{\,2} D_x H^2 \quad M_{torref} = \frac{1}{2}\rho V_h^{\,2} D_x B_y H \qquad \text{Equation 3-3}$$

where V_h is the mean velocity at the building height, ρ is the air density which is taken equal to 1.25 kg/m^3, B_y is the building width (normal to wind direction) and D_x is the building depth (along wind direction).

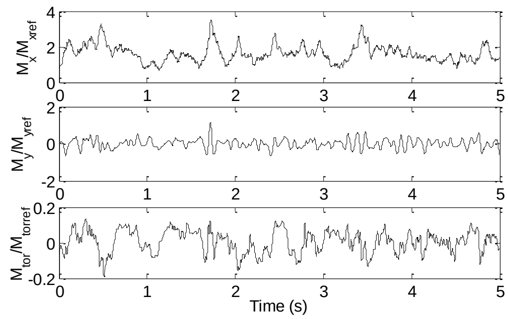

Case 2 (isolated, AOA=0^o)

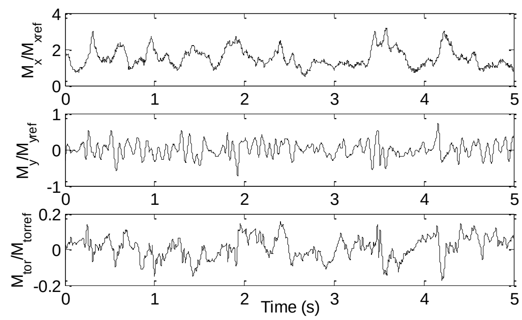

Case 3 (isolated, AOA=90^o)

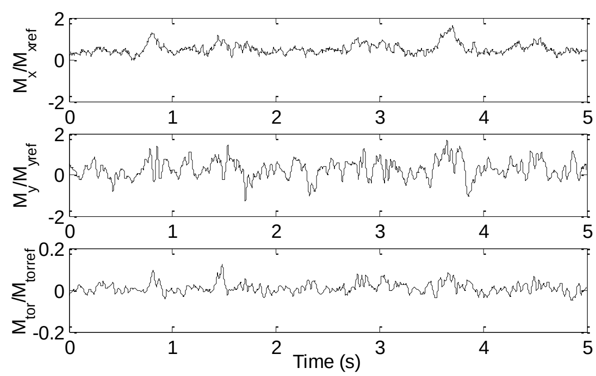

Case 4 (surrounded, AOA=90^o)

Figure 3-19 Base moments around the x-axis (along-wind), y-axis (across-wind) and z-axis (torsional)

Figure 3-20 shows the smoothed Power Spectral Density (PSD) plot, which illustrates the energy distribution with the corresponding frequencies. The PSD plots are evaluated for the isolated and the surrounded configurations using the time history base moments acquired from the LES and the BLWT tests. As shown in this figure, the PSD obtained from the LES matches reasonably with the experimental measurements in the along, across, and torsional wind directions with an average regression coefficient of 0.91. The agreement with the experimental results is found to be affected on a very narrow high frequency range. Although this does not seem to affect the overall base loads, it can be further enhanced by using finer grid resolution (i.e. improving the LES cut-off frequency). It is noticed from Figure 3-20 that there is a peak at high frequency values in the along-wind moment spectra. This peak is believed to be corresponding to the cut-off frequency filter associated with the LES analyses. The agreement can be improved by adopting a finer grid resolution.

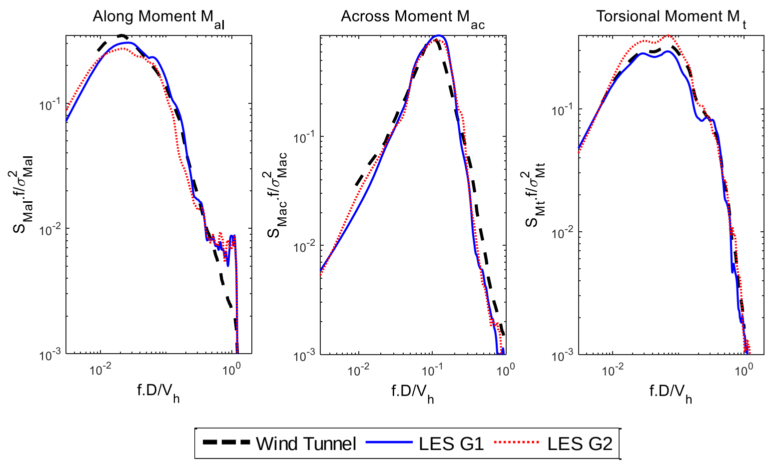

Cases 1 (isolated, AOA=0 º, G1) and 2 (isolated, AOA=0º, G2)

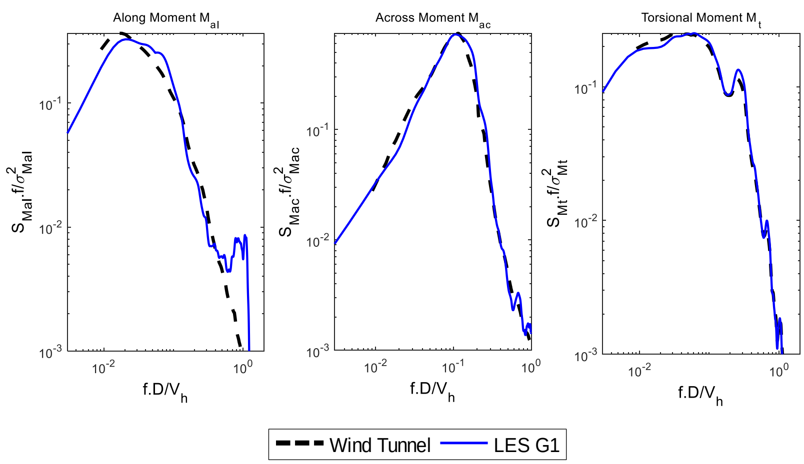

Case 3, (isolated, AOA=90 º)

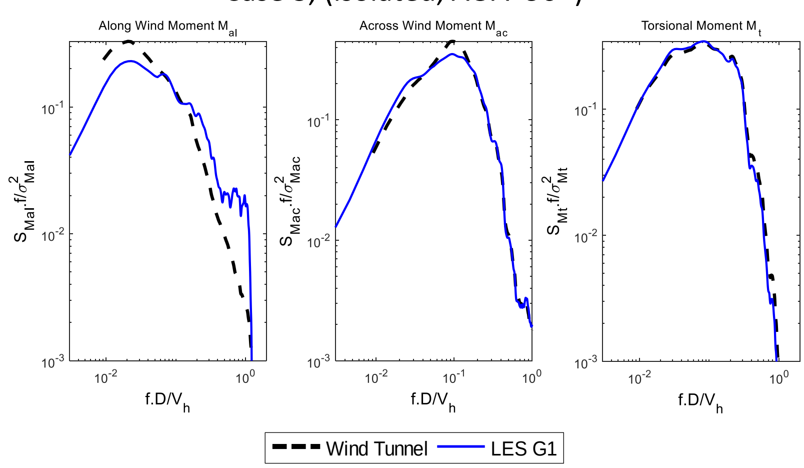

Case 4 (surrounded, AOA=90 º)

Figure 3-20 Spectra of the base moments

Using the spectra of the evaluated base moments, the dynamic responses of the CAARC building are evaluated using the method described by Kijewski and Kareem [24] and Chen and Kareem [44]. The dynamic properties of the CAARC building are listed in Table 3-6. It is assumed that there is no coupling between the responses modes and the building acts as a cantilever for the for the first two mode shapes (developing the maximum deflection and acceleration in the along and across wind directions). The center of mass of the study building is assumed to coincide with its center of rigidity. All building responses are reported at the center of mass of each floor. The peak responses are evaluated following Equation 3-4. In cases where there is a significant coupling between responses modes, more accurate methods could be adopted for evaluating the dynamic responses such as the approaches described in Huang and Chen (2009) [45] and Cui and Caracoglia (2015) [46].

$$R_{peak} = R_{mean} + g_f * R_{rms} \qquad \text{Equation 3-4}$$

where R is the building response and g_f is a peak factor that is taken equal to 3.5.

The peak displacement, acceleration, and base moment are plotted in Figure 3-21, Figure 3-22, and Figure 3-23, respectively. The responses of the CAARC building obtained from the LES models are in a very good agreement with those from the boundary layer wind tunnel. Average difference between LES and WT responses is found to be 6% for the isolated and surrounded building configurations. This indicates the accuracy of evaluating wind loads and responses using LES while employing the CDRFG technique in providing inflow field. For surrounded configuration, a slight discrepancy is noticed between the building responses resulted from experimental and LES results. This difference is believed to be caused by the slight dissimilarity between the frequency ranges simulated in LES and those in the experimental work, also show that surrounded configuration (case 4) has lower torsional response (i.e. top deflection, acceleration and base moments) values than the values of the isolated configuration (Case 3) (i.e. 30% lower). While the across- and along-wind responses of the surrounded configuration are higher than those of the isolated configuration (i.e. 15% higher). This results from the shedding effect introduced by the upstream and side surrounding buildings.

Table 3-6 Dynamic properties of the examined building

Property	Value
Height H, Width B_y, Depth D_x	182.5, 30.5, 45.7 m
Natural Frequency	0.15 (along-wind), 0.15 (across-wind), 0.3 (torsional)
Damping ratio	1% for all modes
Mass per unit volume m_s	192 kg/m^3

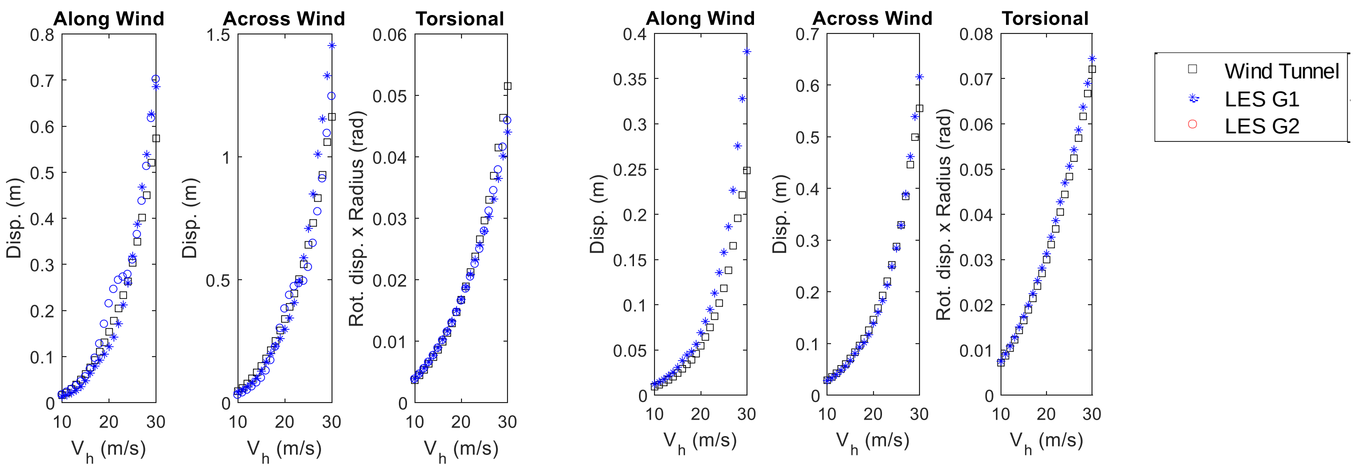

Cases 1 (isolated, AOA=0°, G1) and 2 (isolated, AOA=0 °, G2)

Case 3 (isolated, AOA=90 °)

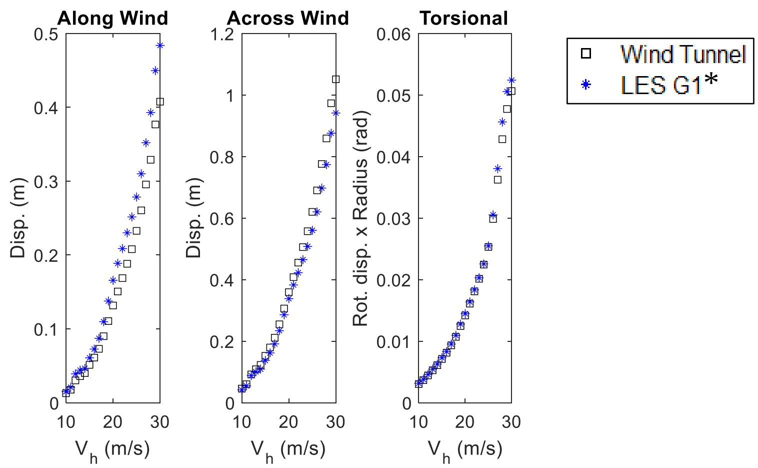

Case 4 (surrounded, AOA=90 °)

Figure 3-21 Peak top floor displacements

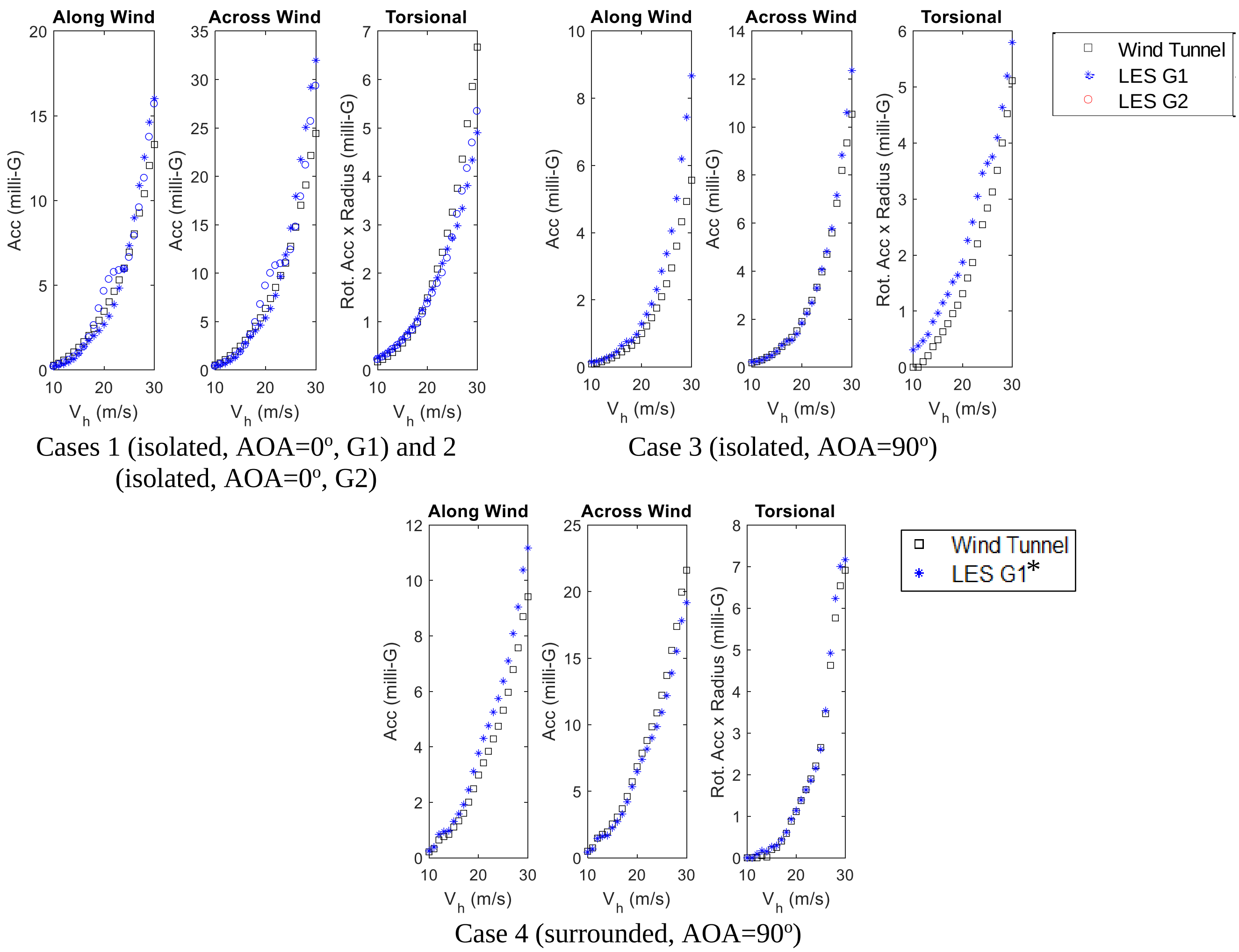

Figure 3-22 Peak top floor accelerations

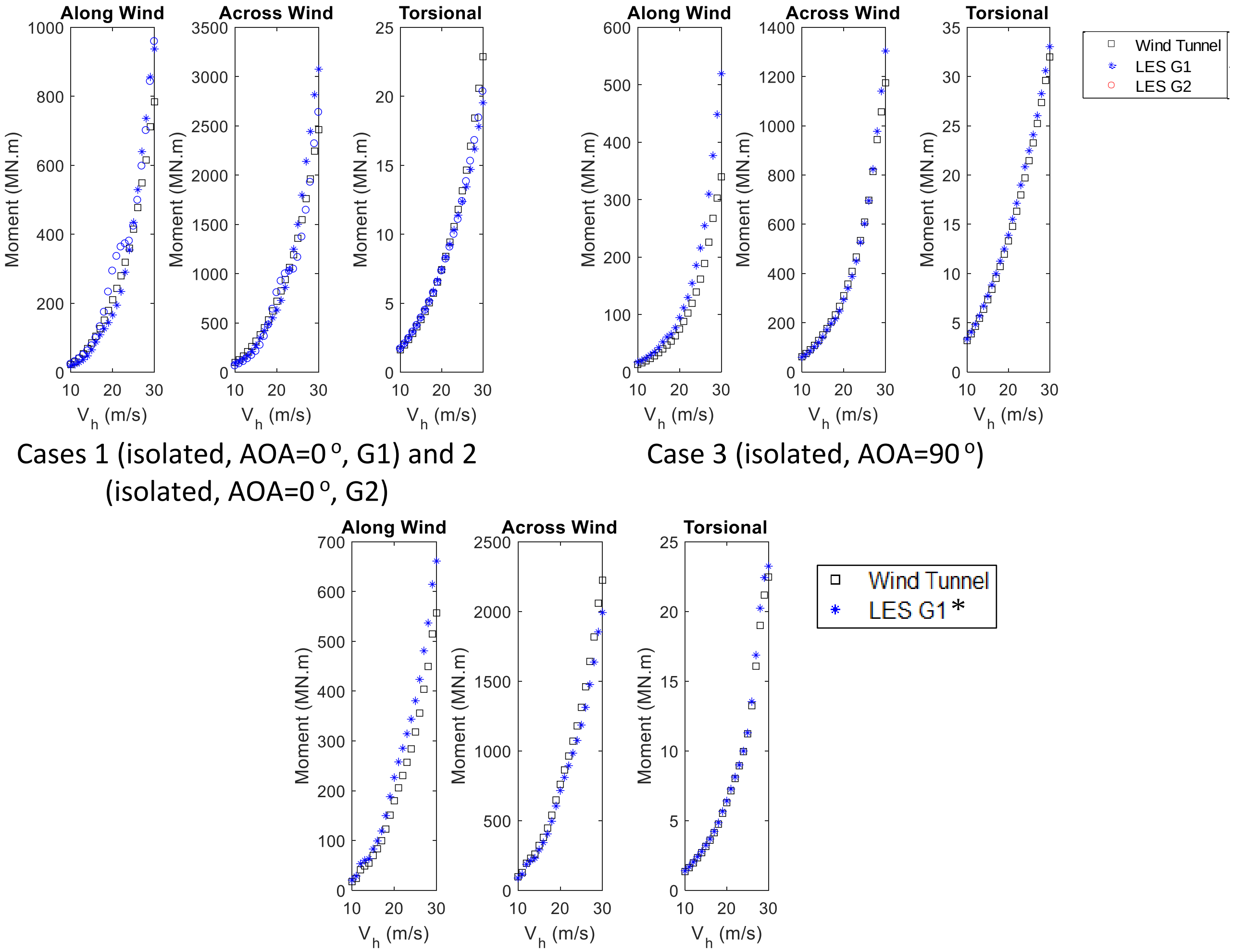

Cases 1 (isolated, AOA=0 º, G1) and 2 (isolated, AOA=0 º, G2)

Case 3 (isolated, AOA=90 º)

Case 4 (surrounded, AOA=90 º)

Figure 3-23 Peak base moments

3.6 Conclusions

This study focuses on evaluating tall building aerodynamic responses using LES. The method of Consistent Discrete Random Flow Generator (CDRFG) developed previously by the authors is used to generate the inflow boundary condition (IBC) that satisfies the proper turbulence spectra and coherency. The Commonwealth Advisory Aeronautical Research Council (CAARC) building is modeled considering both isolated and surrounded configurations. This is to assess the accuracy of LES employing the CDRFG technique in evaluating tall building responses for both configurations. Results obtained from the LES model are compared with the results obtained from a previous boundary layer wind tunnel

(BLWT) test and previous numerical simulations from literature and the following conclusions can be withdrawn.

- Pressures obtained from the current LES model for the isolated building configuration are in a very good agreement with the pressures measured in the BLWT. Mean pressures values obtained from the current LES model has a better agreement with the BLWT results compared to previous numerical models, especially at the leeward and side building faces (i.e. ~ 3% on average). Also, rms pressures values obtained from the current LES model has a better agreement with the BLWT results compared to previous numerical models at the windward and leeward building faces. (i.e. ~ 4 % on average).

- Base moment spectra and building responses obtained from the current LES model well agree with the spectra and responses obtained from WT. Average difference between LES and WT responses is found to be less than 6% for both configurations.

- As expected, significant differences are noticed in terms of pressures and dynamic responses of the isolated and the surrounded configurations. In general, surrounded configuration has a lower mean pressure values (i.e. 50 % or more) and higher rms values (i.e. 40 % on average) than those of the isolated configurations. The torsional responses of the surrounded configuration are found to be lower than the responses of the isolated configuration (i.e. 30 % lower). However, the along- and across-wind responses of the surrounded configuration are found to be higher than the responses of the isolated configuration (i.e. 15 % higher). This indicates the importance of including the surrounding effects while evaluating the pressure distributions of a tall building and responses.

- The employed LES model while using CDRFG technique to simulate the inflow field leads to more accurate estimation for the wind pressure distributions on a tall building and its responses. Since, this model supports parallel computation, it allows for a time-efficient evaluation of the building aerodynamic behavior (i.e. in the order of 12 *hrs*.).

3.7 References

1] Tominaga Y, Stathopoulos T. Numerical simulation of dispersion around an isolated cubic building: model evaluation of RANS and LES. Building and Environment 2010; 45 (10), 2231-2239.

[2] Tominaga Y, Stathopoulos T. CFD modeling of pollution dispersion in a street canyon: Comparison between LES and RANS. Journal of Wind Engineering and Industrial Aerodynamics 2011; 99(4), 340-348.

[3] Gousseau P, Blocken B, Stathopoulos T, van Heijst GJF. CFD simulation of near-field pollutant dispersion on a high-resolution grid: a case study by LES and RANS for a building group in downtown Montreal. Atmospheric Environment 2011; 45 (2), 428-438.

[4] Jiang Y. Study of Natural Ventilation in Buildings with Large Eddy Simulation. Massachusetts Institute of Technology, Cambridge, Mass 2002.

[5] Durrani F, Cook M, McGuirk J. Evaluation of LES and RANS CFD modelling of multiple steady states in natural ventilation. Building and Environment 2015; 92, 167-181.

[6] Abdi D, Bitsuamlak G. Wind flow simulations on idealized and real complex terrain using various turbulence models. Advances in Engineering Software 2014; 75, 30-41.

[7] Nozawa K, Tamura T. Large eddy simulation of the flow around a low-rise building immersed in a rough-wall turbulent boundary layer. Journal of Wind Engineering and Industrial Aerodynamics 2002; 90, 1151-1162.

[8] Huang S, Li QS, Xu S. Numerical evaluation of wind effects on a tall steel building by CFD, Journal of Constructional Steel Research 2007; 63(5), 612-627.

[9] Tamura T. Towards practical use of LES in wind engineering. Journal of Wind Engineering and Industrial Aerodynamics 2008; 96, 1451-1471.

[10] Braun AL, Awruch AM. Aerodynamic and aeroelastic analyses on the CAARC standard tall building model using numerical simulation. Computers and Structures 2009; 87(9-10), 567-581.

[11] Dagnew A, Bitsuamlak GT. Computational evaluation of wind loads on standard tall building using a large eddy simulation. Wind and Structures 2014; 18(5), 567-598.

[12] Aboshosha H, Elshaer A, Bitsuamlak G, El Damatty A. Consistent inflow turbulence generator for LES evaluation of wind-induced responses for tall buildings. Journal of Wind Engineering and Industrial Aerodynamics 2015a; 142, 198-216.

[13] Dagnew A, Bitsuamlak GT. Computational evaluation of wind loads on buildings: a review, Wind and Structures 2013; 16(6), 629-660.

[14] Huang SH, Li QS. Large eddy simulation of wind effects on a super-tall building. Wind and Structures 2010; 13 (6), 557-580.

[15] Keating A, Piomelli U, Balaras E, Kaltenbach HJ. A priori and a posteriori tests of inflow conditions for large-eddy simulation. Physics of Fluids 2004; 16, 4696.

[16] Bitsuamlak GT, Simiu E. CFD's potential applications: wind engineering perspective. The fifth International Symposium on Computational Wind Engineering 2010; Chapel hill, NC.

[17] Liu KL, Pletcher RH. Inflow conditions for the large eddy simulation of turbulent boundary layers: a dynamic recycling procedure. Journal of Computational Physics 2006; 219 (1), 1-6.

[18] Lund TS, Wu X, Squires KD. Generation of turbulent inflow data for spatially developing boundary layer simulations. Journal of Computational Physics 1998; 140, 233-258.

[19] Aboshosha H, Bitsuamlak G, El Damatty A. LES of ABL flow in the built-environment using roughness modeled by fractal surfaces. Sustainable Cities and Societies 2015b; 19, 46-60.

[20] Kondo K, Murakami S, Mochida A. Generation of velocity fluctuations for inflow boundary condition of LES. Journal of Wind Engineering and Industrial Aerodynamics 1997; 67-68, 51-64.

[21] Huang S, Li Q, Wu J. A general inflow turbulence generator for large eddy simulation. Journal of Wind Engineering and Industrial Aerodynamics 2010; 98, 600-617.

[22] Smirnov R, Shi S, Celik I. Random flow generation technique for large eddy simulations and particle-dynamics modeling. Journal of Fluids Engineering 2001; 123, 359-371.

[23] Davenport AG. How can we simplify and generalize wind loads? Presented at the Third Asia-Pacific Symposium on Wind Engineering 1993; Keynote Lecture. Hong Kong.

[24] Kijewski T, Kareem A. Dynamic wind effects: a comparative study of provisions in codes and standards with wind tunnel data. Wind and Structures 1998; 1(1), 77-109.

[25] Zhang A, Gu M., Wind tunnel tests and numerical simulations of wind pressures on buildings in staggered arrangement. Journal of Wind Engineering and Industrial Aerodynamics 2008; 96(10-11), 2067-2079.

[26] Kareem A, Spence S, Bernardini E, Bobby S, Wei D. Using computational fluid dynamics to optimize tall building design. CTBUH Journal 2013; 3, 38-43.

[27] Elshaer A, Bitsuamlak G, El Damatty A. Aerodynamic shape optimization for corners of tall buildings using CFD. 14th International Conference on Wind Engineering 2015a; Porto Alegre, Brazil.

[28] Elshaer A, Bitsuamlak G, El Damatty A. Vibration control of tall buildings using aerodynamic optimization. 25th Canadian Congress of Applied Mechanics 2015b; London, Canada.

[29] Dagnew A, Bitsuamlak GT. Large eddy simulation for wind-induced response of tall buildings located in a city center. Engineering Mechanics Institute and 11th ASCE Joint Specialty Conference on Probabilistic Mechanics and Structural Reliability (EMI/PMC 2012); Notre Dame, IN June 17-20.

[30] Wardlaw RL, Moss GF. A Standard Tall Building Model for the Comparison of Simulated Natural Winds in Wind Tunnels 1970. Report CC-662 Tech. 25, Commonwealth Advisory Aeronautical Research Council, UK.

[31] Melbourne WH. Comparison of measurements of the CAARC standard tall building model in simulated model wind flows. Journal of Wind Engineering and Industrial Aerodynamics 1980; 6:78-88.

[32] Dragoiescu C, Garber J, Kumar SS. A comparison of force balance and pressure integration techniques for predicting wind-induced response of tall buildings. Structural Engineering and Public Safety Proceedings of the Structures Congress 2006.

[33] Engineering Sciences Data Unit (ESDU) 85020. Characteristics of atmospheric turbulence near the ground. Part II: single point data for strong winds 2001.

[34] Zhou Y, Kijewski T, Kareem A. Aerodynamic Loads on Tall Buildings: Interactive Database. Journal of Structural Engineering 2003; ASCE. 3, 394-404.

[35] COST. Best practice guideline for the CFD simulation of flows in the urban environment COST 2007; Action 732.

[36] Franke J. Recommendations of the COST action C14 on the use of CFD in predicting pedestrian wind environment. The forth international Symposium on Computational Wind engineering 2006; Yokohama, Japan. 529-523.

[37] STAR CCM+. CD-ADAPCO Product, www.cd-adapco.com/products/star-ccm 2015.

[38] Smagorinsky J. General circulation experiments with the primitive equations, I. the basic experiment. Monthly Weather Review 1963; 91, 99-164.

[39] Germano M, Piomelli U, Moin P, Cabot WH. A dynamic subgrid-scale eddy viscosity model. Physics of Fluids 1991; 3(7), 1760-1765.

[40] SHARCNET is a consortium of colleges, universities and research institutes operating a network of high-performance computer clusters across south western, central and northern Ontario," 2015; [Online]. Available: www.sharcnet.ca.

[41] Murakami S. Overview of turbulence models applied in CWE-1997. Journal of Wind Engineering and Industrial Aerodynamics 1998; 74-76, 1-24.

[42] Tominaga Y, Mochida A, Yoshiec R, Kataokad H, Nozu T, Yoshikawa M, Shirasawa T. AIJ guidelines for practical applications of CFD to pedestrian wind environment around buildings. Journal of Wind Engineering and Industrial Aerodynamics 2008; 96(10-11), 1749-1761.

[43] Kim YC, Yoshida A, Tamura Y. Characteristics of surface wind pressures on low-rise building located among large group of surrounding buildings. Engineering Structures 2012; 35, 18-28.

[44] Chen X, Kareem A. Dynamic wind effects on buildings with 3-D coupled modes: application of HFFB measurements. Journal of Engineering Mechanics 2005; ASCE, 131(11), 1115-1125.

[45] Chen X, Huang G. Evaluation of peak resultant response for wind-excited tall buildings. Engineering Structures 2009; 31(4):858-68.

[46] Cui W, Caracoglia L. Simulation and analysis of intervention costs due to wind-induced damage on tall buildings. Engineering Structures 2015; 87:183-197.

Chapter 4

4 Enhancing wind performance of tall buildings using corner aerodynamic optimization

4.1 Introduction

New generations of tall buildings are becoming increasingly taller, flexible and slender primarily driven by novel developments in design methods and new construction materials and techniques. This in turn makes tall buildings more sensitive to lateral loads such as wind. In addition, there is a need to lower the building weight in order to decrease the gravity loads to control the inertial forces developed by earthquake. This further contributes to an increase in the wind-induced forces and motions. As a result, wind-induced loads and motions typically govern the design of the lateral load resisting systems in tall buildings. The outer shape of the building is one of the main parameters that affect these loads and responses. The dependence of the wind load on the building shape makes the generalizations of wind load for tall buildings almost impossible, because every complex shape and surroundings produce a unique set of design wind loads. On the other hand, this dependency on the shape provides a unique opportunity to reduce the wind load through outer shape modifications either globally or locally. In that context, global modification involves major changes on the form of the building, which has a considerable effect on the overall architectural and structural design. This includes large openings, tapering, twisting, set-backing, etc. The architects can implement global modifications at the early conceptual design of the building if the modifications fit with the major functionalities of the building. On the other hand, local modifications result in minor changes on the building shape that have limited effects on the structural and architectural designs. Thus, the architects can introduce the local mitigations at a later stage of the conceptual design. One such local mitigation is corner modification; whish is the focus of the present study.

The outer shape of tall buildings is typically aerodynamically “bluff” and characterized with sharp corners. Wind loads for tall buildings with various shapes have been widely investigated in many numerical and experimental wind engineering studies, few examples include Vickery [1], Lee [2], Okajima [3], Igarashi [4], Nakamura and Ohya [5], and Merrick and Bitsuamlak [6]. Many researchers have reported that careful modification of the shape of the corners can provide better aerodynamic performance (Kwok [7], Kareem et al. [8], Tamura and Miyagi [9], Carassale et al. [10]). Figure 4-1 summarizes the widely used corner modifications in literature. Boundary Layer Wind Tunnel (BLWT) based studies (Kawai [11], Gu and Guan [12], Tse et al. [13], Carassale et al. [10]) reported chamfered, recessed and rounded corners to be effective in reducing the along- and across-wind forces. Kwok and Bailey [14] reported that finned corners increase the along-wind and decrease the across-wind responses, while slotted corners reduce responses in both directions. Tamura and Miyagi [9] reported that 2D flow BLWT tests were sufficient to indicate the aerodynamic improvements by corner modifications similar to ABL flow tests. Table 4-1 summarizes the scope and main findings of previous experimental and computational studies focusing on aerodynamic modifications of tall building corners.

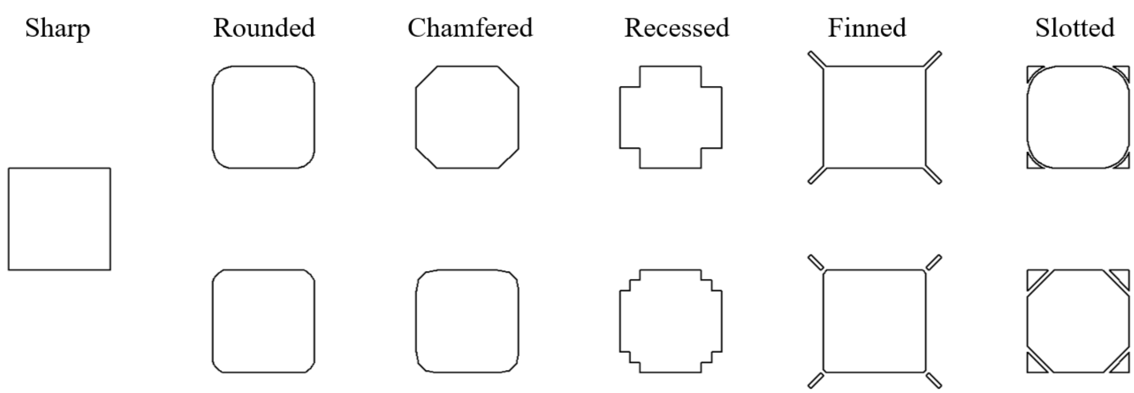

Figure 4-1 Examples of tall building corner mitigations

Table 4-1 Scope and main findings of previous studies focused on local mitigations

Reference	Method	Scope	Findings/ Comments
Kwok and Bailey [14] Kwok et al. [15]	BLWT	Square sections with fins, vented fins and slotted corners	Fins and slotted fins increase the along-wind responses and reduce the across-wind responses. While slotted corners reduce both along- and across-wind responses.
Kawai [11]	BLWT	Square and rectangular sections with rounded, chamfered and recessed corners	Small chamfers and recessions are effective in preventing aeroelastic instability. Rounded corners increase the aerodynamic damping.
Tamura et al. [16]	CFD	Square sections with rounded and chamfered corners using smooth uniform flows	CFD is very reliable in predicting wind loads and basic flow statistics and is able to capture the aerodynamic improvement resulted from corner modifications.
Tamura and Miyagi [9]	BLWT	Square sections with rounded and chamfered corners using smooth uniform and turbulent flows	Chamfered and rounded corners decrease drag forces. Fluctuating lift coefficients for the 3D turbulent models are lower by 10% compared with those obtained from 2D models.
Gu and Guan [12]	BLWT	Square and rectangular sections with chamfered and recessed corners	The effects of terrain condition, aspect ratio and side ratio of cross section are investigated for different cross-sections. In addition, formulas for the power spectra of the across-wind dynamic forces, the coefficients of base moment and shear force are derived.
Tse et al. [13]	BLWT	Square and rectangular sections with chamfered and recessed corners	The effects of aspect ratio of recessed corners are pronounced compared to chamfered corners. Empirical formulae are proposed to relate the cross-wind responses to the building dimensions and dynamic properties
Tanaka et al. [17]	BLWT	Square sections with recessed and chamfered	Base moments and moment coefficients of tall buildings with

		corners in addition to other global modifications such as twisting, openings, tapering and set-backing	various configurations are reported.
Carassale et al. [10]	BLWT	Square sections with rounded corners of different modification length.	Critical angle of incidence decreases with the increase in the modification length. Supercritical Re regime observed only for larger modification lengths.
Elshaer et al. [18]	CFD	Square sections with rounded chamfered and recessed corners using 2D flow and different inflow velocities.	2D models can provide sufficient accuracy for comparing the effect of aerodynamic modifications. Round corners are effective in reducing drag followed by chamfered and then recessed shapes.

As summarized in Table 4-1, BLWT has been widely used for studying building aerodynamic mitigations. This approach is reliable but only useful to compare limited number of feasible building shapes in addition to being costly for repetitive investigation. A wide portion of the search space remains unexplored as the search space is only limited to the tested options (Bernardini et al. [19]). On the other hand, integrating CFD with an optimization algorithm can be more useful to explore wider geometric alternatives to find near optimal shapes. This is inspiring an increased number of researchers to work on building aerodynamic optimization applications. For example, Kareem et al. [20-22] introduced an approach for tall building corner optimization to reduce drag and lift by adopting low-dimensional CFD models. This approach is useful to overcome the computational cost associated with the iterative procedure required for optimization. Bernardini et al. [19] investigated the efficiency of utilizing Kriging model as a surrogate model for the objective function evaluation. The utilization of a surrogate model reduced the computational time. In these studies, Unsteady Reynolds-Averaged Navier–Stokes (URANS) equations were used. Although these studies developed a very promising and useful approach for building aerodynamic optimizations, some limitations are observed. For example, (i) wind directionality effect is not considered, (ii) low-order CFD models are used to evaluate shape alternatives, although wind performance assessment usually requires the use of high accuracy CFD- or BLWT-based evaluations. Using these novel approaches, it is possible to infer the relative performance of the various geometric alternatives (i.e. comparing alternatives) adopting the reduced order 2D simulations. A similar conclusion was also reported by Tamura and Miyagi [9]. However, adopting a simplified low order simulation can significantly reduce the analysis accuracy that may affect the conclusions observed under such simplified scenarios. Particularly when simulating the turbulent atmospheric boundary layer (ABL) flow and its interaction with a tall building. In the author's opinion, the CFD simulations used to assess wind loads on buildings shall be commensurate with the complexity encountered in urban flows. These complex interactions can be realistically captured through LES as reported by Nozawa and Tamura [23], Dagnew and Bitsuamlak [24, 25], Aboshosha et al. [26] and Elshaer et al. [27]. It is to be noted that the accuracy of LES depends on the proper selection of the inflow boundary conditions and the adopted grid resolution. Thus, the consistent discrete random flow generator (CDRFG) technique developed by the authors is utilized to validate the wind responses for the best performing shapes. This technique was previously adopted to study a low-rise building (Hajra et al. [28]), a standalone tall building (Aboshosha et al. [29]) and a surrounded tall building in a city center (Elshaer et al. [27]).

Building on these interesting benchmark aerodynamic optimization studies and targeting to address their shortcomings, the current study presents a new Aerodynamic Optimization Procedure (AOP) that uses LES and accounts for the wind directionality effects (by considering all wind directions). In this procedure, 3D LES models of a 2D flow are utilized to generate the seed aerodynamics database used to train surrogate models. The wind responses of the selected shapes are further verified through accurate 3D LES simulation of an ABL flow (i.e. 3D turbulent flow) interacting with the study building.

The paper is organized in four sections. Section 1 (this section) presents an introduction and literature review on building aerodynamic mitigations. In section 2, a description for the developed AOP is provided. Section 3 presents two optimization application examples focusing on minimizing drag and lift, respectively. Section 4 presents results and discussions of the optimization examples, and verification for the near optimal solutions using ABL flow based wind response.

4.2 Aerodynamic Optimization Procedure (AOP)

The AOP can be adopted for examining various types of mitigations, including corner rounding, chamfering, slotting, building twisting, tapering, etc. It is to be noted that the building shape usually bounded by other architectural and structural design considerations in addition to improving the aerodynamic performance. Thus, the proper selection of the design variables and their upper and lower bounds will ensure that the optimal shape will satisfy other architectural and structural design targets as well.

The AOP aims at minimizing the drag and/or lift by searching the best combinations of these geometric parameters. The current study adopts Genetic Algorithm (GA) for the optimization process. More detailed discussion on GA is provided below in the next paragraph. The GA based optimization procedure requires numerous evaluations of the objective function corresponding to multiple initial candidates, i.e. combinations of design variables, over many generations. If the objective functions are to be evaluated directly using LES, the process becomes computationally costly. Therefore, in the current study, the objective functions for the optimization procedure are evaluated using an Artificial Neural Network (ANN) based surrogate model. The ANN is trained using aerodynamic database of randomly selected design variables obtained from 3D LES simulations of a 2D flow. The utilization of a surrogate model in the optimization procedure will (i) significantly reduce the overall computational cost, (ii) eliminate the need for the direct integration of the CFD with the optimization process (i.e. CFD can be used offline to train the surrogate model), and (iii) allows the use of any available BLWT database in conjunction with the CFD database. ANN model can map a highly nonlinear relationship if trained properly (Bitsuamlak et al. [30]). Exploratory work was reported by the authors in optimizing a building shape for reducing wind drag (Elshaer et al. [31]) and for controlling the building vibrations due to wind (Elshaer et al. [32]) that laid the ground work for the present detailed work. ANN model was adopted in many previous wind engineering [33-35] and aerospace engineering [36] applications. At the end, a verification step is conducted to accurately evaluate the wind loads and to compare the performance of the optimal shape to other near optimal ones. This verification, for the selected shapes, is carried out by using a high accuracy 3D LES of an ABL flow following the procedure described in Aboshosha et al. [29]. Figure 4-2 summarizes the entire aerodynamic optimization procedure.

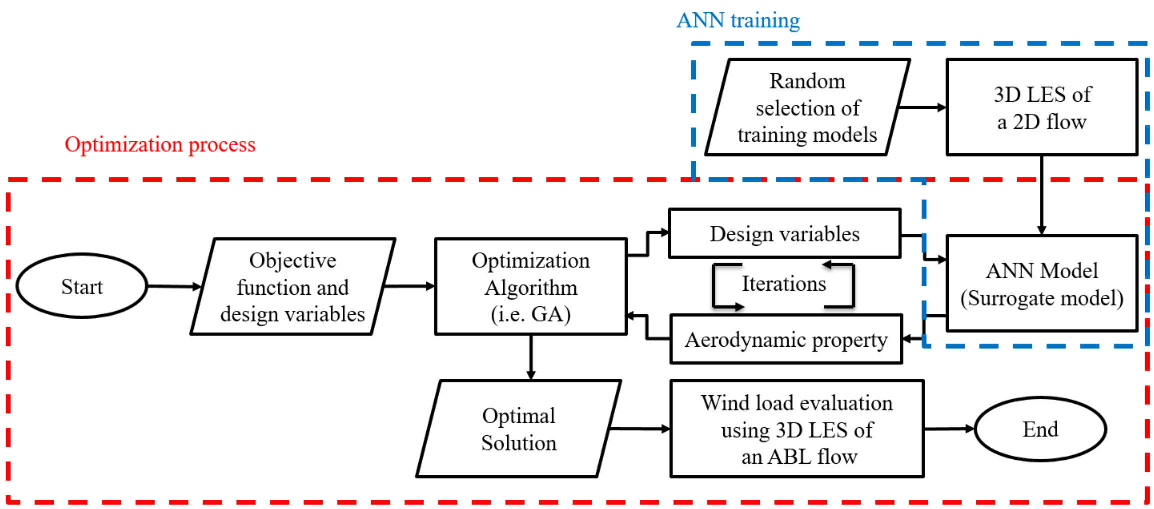

Figure 4-2 Framework of Aerodynamic Optimization procedure (AOP)

Genetic Algorithm (GA), where design variables are coded as real numbers, is adopted for the optimization process. One of the advantage of GA over gradient-based techniques is that it is capable of locating the global extreme value (i.e. maximum or minimum) with less probability of being trapped in a local extreme value. This key capability results from initiating the search process from multiple points in the search space and having mutation operators that generate search points away from the high fitness region to avoid being trapped in local extreme value. The GA is reported to be efficient in estimating the optimal solutions in similar complex engineering optimization problems by Zhou and Haghighat [37] and El Ansary et al. [38]. More detailed discussion on GA can be found in Goldberg [39] and Davis [40]. To recapitulate, the AOP starts by defining the objective function, the design variables, the size of the population, the number of required generations, the number of operators, and the upper and lower bound for each design variable. As explained before, the objective function is the aerodynamic property required to be minimized, while the design variables are the geometric parameters controlling the outer building shape. In GA, each combination of different design variables is called “candidate or chromosome” and represents different building shapes. The GA starts the optimization search using many starting candidates called the “initial population”. The objective function is evaluated for each candidate within the initial population and the candidates will be sorted according to their fitness, i.e. lowering the value objective function. Crossover and mutation operators are then applied on the current population to produce new offspring that form the next population. Crossover operators are applied to the candidates (parents) with higher fitness to produce better candidates (offsprings). While the mutation operators are applied to candidates with lower fitness in order to explore different regions in the search space and avoid stagnating in a local extreme value (Mengistu and Ghaly [36]). The procedure of applying the operators and producing new generations will continue until no significant improvements are obtained over the generations. The highest fitting candidate in the last generation will be considered the optimal solution. Figure 4-3 summarized the overall optimization process using GA.

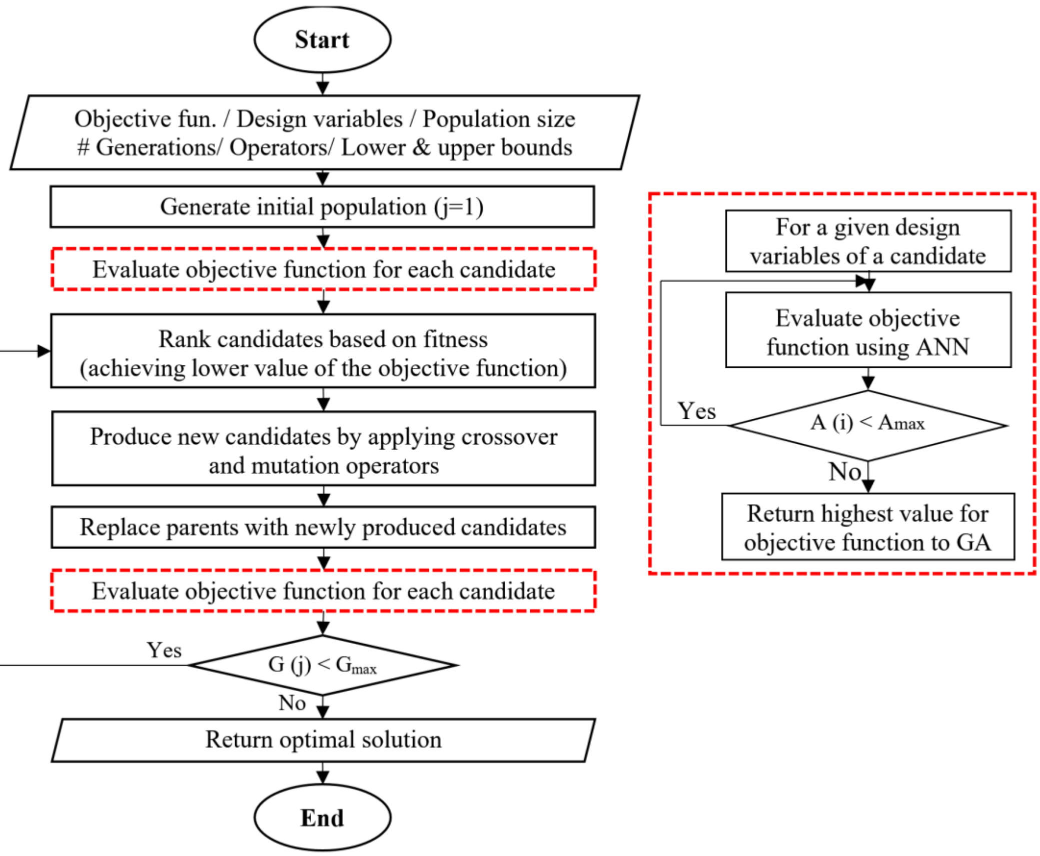

Figure 4-3 Flowchart of the genetic algorithm optimization process

4.3 Aerodynamic optimization application examples

The efficiency of the proposed aerodynamic optimization procedure is examined through two examples. Example 1 aims at finding a cross-section that minimizes the drag forces, while Example 2 aims at finding a cross-section that minimizes the across-wind vibration (or load). Thus, the objective functions are set to be the mean drag coefficient ($\overline{C_D}$) and the standard deviation of the lift coefficient ($C_L{}'$) in Examples 1 and 2, respectively. For each combination of design variables (candidate), the objective function is evaluated for all wind directions with an increment of 5 degrees and the critical wind direction (i.e. the one that develops the highest mean $\overline{C_D}$ or $C_L{}'$) is utilized as the value for the objective function. The C_D and C_L are evaluated using Equation 4-1. In both examples the base building cross-section is chosen to be a square with 50 mm by 50 mm (at wind tunnel scale) plan dimension similar to previous wind tunnel studies from the literature (Tamura et al. [16], Kawai [11], Tamura and Miyagi [9]). Figure 4-4 defines the geometric parameters of the building cross-section. The design variables (*v1* and *v2*) represent the corner shapes and are defined following Equation 4-2. The architect can set the lower and upper bound for each design variable. In the present study, the lower and upper bounds are set to 0.01 and 0.2 for *v1*, respectively. While for *v2*, the lower and upper bounds are set to -1.0 and 2.0, respectively. These geometric parameters are utilized during the LES analyses.

$$C_D = \frac{F_D}{\frac{1}{2}\rho v_{ref}^2 A_p}$$
$$C_L = \frac{F_L}{\frac{1}{2}\rho v_{ref}^2 A_p}$$

Equation 4-1

where F_D and F_L are the along- and across- wind forces, respectively, ρ is the air density, v_{ref} is the reference velocity at the building height and A_p is the building projected cross-section area.

$$v_1 = \frac{c}{L}$$
$$v_2 = \frac{a}{c}$$

Equation 4-2

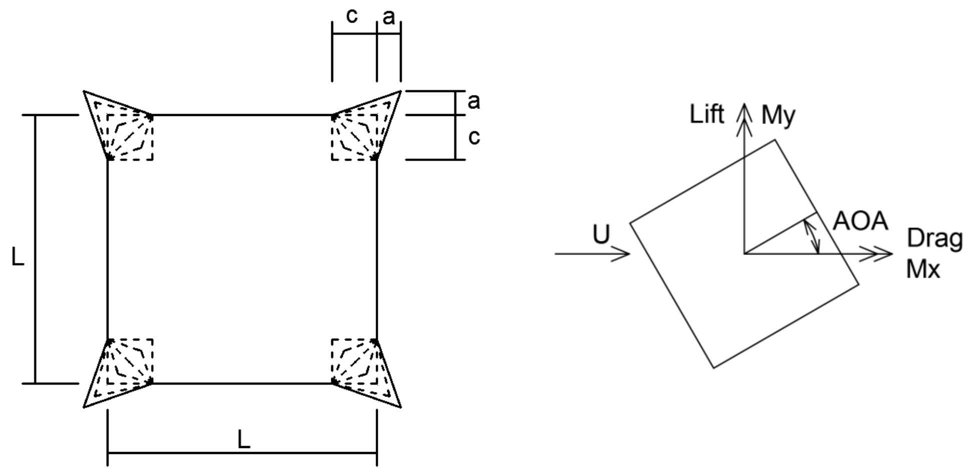

Figure 4-4 Geometric parameters of the study cross-section

4.3.1 LES properties of a 2D flow (training models)

The three-dimensional LES analyses of a 2D flow are carried out to produce the aerodynamic database corresponding to various geometric design parameters discussed in the earlier section and wind angle of attacks (AOAs). This aerodynamic database is used to train the ANN models. The training samples are selected to be random combinations of the design geometric variables and AOA to capture the variability of the ANN outputs (objective function values) with the inputs (design geometric variables and AOA), as shown in Figure 4-5. Effectiveness of the ANN model like any other data driven model is very much dependent on the quality of the training data. Hence a wide range of random representative design geometric parameters and AOA are used for the present study. After randomly selecting the required training samples, initial graphics exchange specification (IGES) files are generated for each input sample using AutoLisp (AutoCAD) in the format readable by the CFD solver. A commercial CFD software, STAR-CCM+ v.10.06 [41], is used in SharcNet [42], a high performance computer facility at the University of Western Ontario. The work flow is automated through a MATLAB code that includes the process of selecting the samples, generating (IGES) files, building CFD models, submitting jobs for SharcNet, and extracting the output from CFD models.

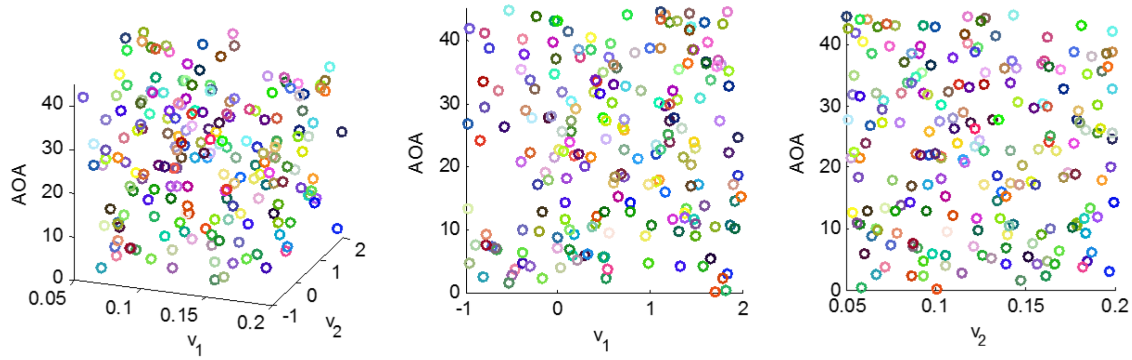

Figure 4-5 Training samples for Artificial Neural Network model

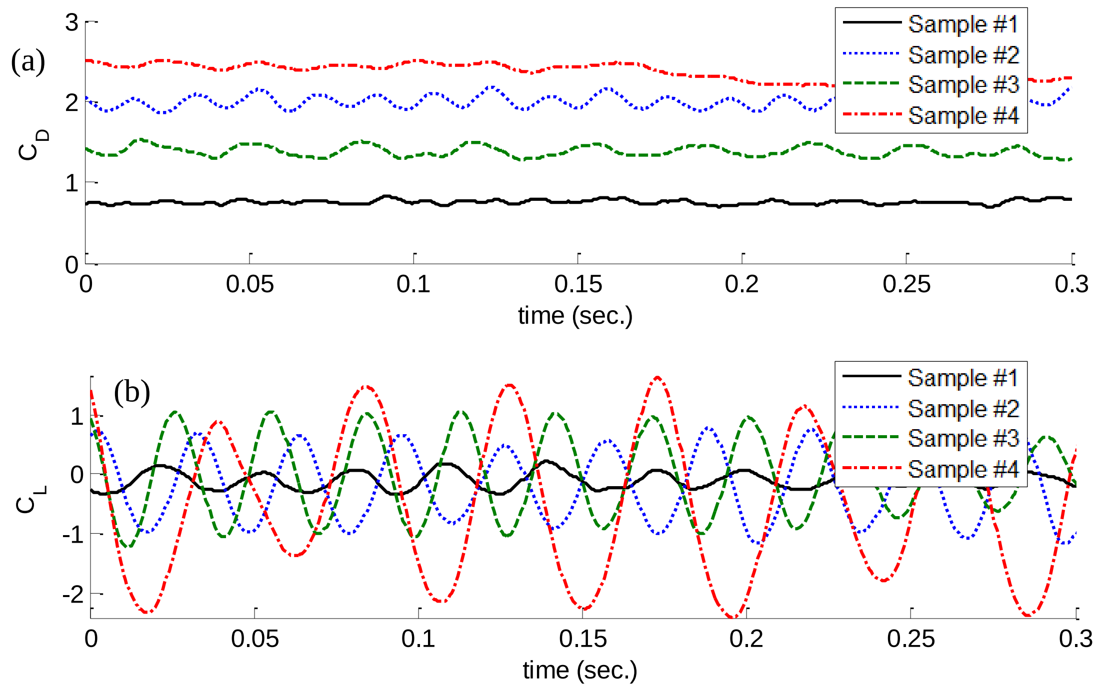

Figure 4-6 (a) Drag and (b) lift coefficient time histories for different geometric samples

3D LES of a 2D flow is conducted for each sample using a length scale of 1:500, time scale of 1:100, and a uniform inlet velocity of 10 *m/s*. The outlet is considered to be a pressure outlet. Top, bottom and the two sides are assigned symmetric plane boundary conditions. All the building faces are assigned as "No-slip" walls. The total number of mesh cells in each model is more than 200,000. The polyhedral mesh size is less than (*L/20*), where *L* is the width of the building. The dimensions of the employed computational domain follow the recommendation of COST guidelines (Franke et al. [43]). The dynamic Sub-Grid Scale model by Smagornisky [44] and Germano et al. [45] is used to account for the turbulence. In order to ensure the convergence and the accuracy of the solution, Courant Friedrichs-Lewy (CFL) is maintained less than 1.0 by setting the solution time step to be 0.0005 *s* (i.e. maximum CFL ~ 0.5 at the top of the building). Each simulation is resolved to 1000 time steps representing 0.5 second in model-scale (i.e. 0.8 minute in full-scale). Time history for the C_D and C_L are extracted from LES to evaluate $\overline{C_D}$ and $C_L{}'$, as shown in Figure 4-6. Figure 4-7 show the generated mesh and the velocity contour for different corner shapes and angles of attack in both examples.

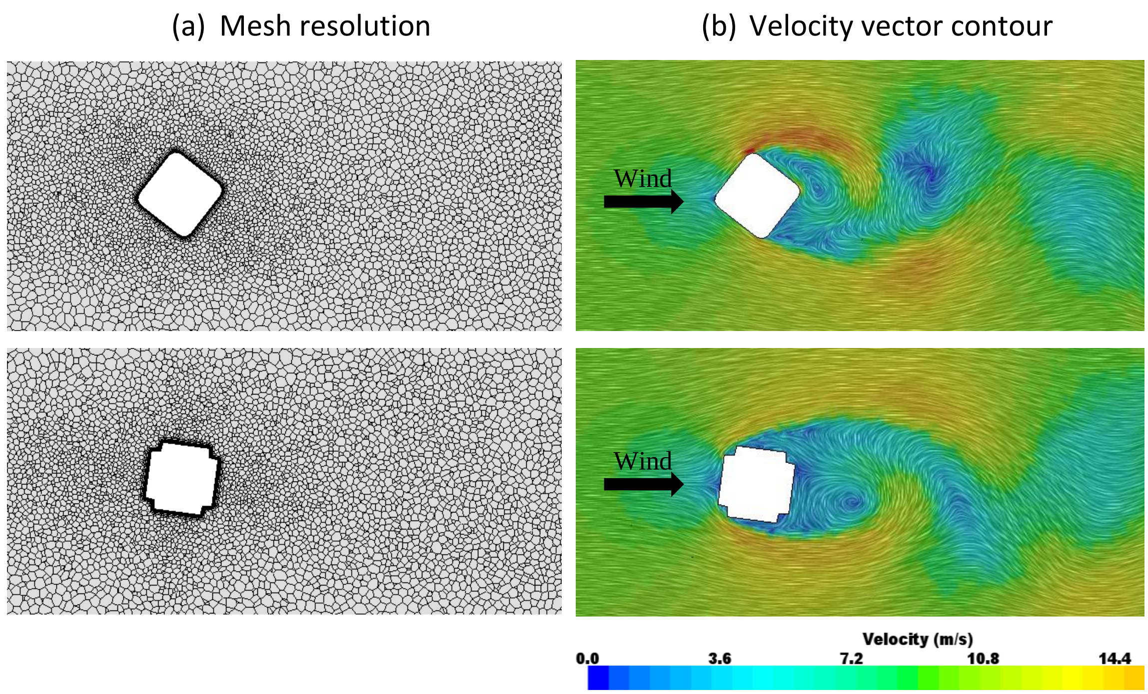

Figure 4-7 (a) mesh resolution utilized in 2D-CFD simulations for different samples and (b) instantaneous velocity vector contour

4.3.2 ANN model properties

Different analytical models, including polynomial, trigonometric, exponential and logarithmic functions, are examined to select the best model that provides reliable evaluation for the objective function. More than 8.5×10^{10} formulas (using Eureqa

Formulize software) were tested and ranked based on their correlation coefficient. Table 4-2 shows examples for the high ranked analytical models and their formulas for evaluating the objective function (C_L'). It is found that the highest correlation coefficient that could be obtained is 0.86.

Table 4-2 Examples for the analytical models and their formulas

Rank	Analytical model	Regression plot (Target vs Output)
1	C_L' = 0.638 + 0.282*v2 + v1*v2 + 0.505* cos(0.161 *AOA) * sin(0.394 *v2 + 5.134 /AOA) - 0.005*AOA - 0.013*v2*AOA	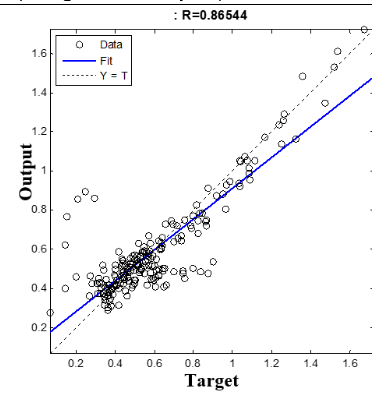
2	C_L' = 0.666 + 0.291*v2 + 0.471 *v1*v2^2 + 0.497 * cos(0.163 *AOA) * sin(0.384*v2 + 5.136/ AOA) - 0.006*AOA - 0.011 *v2*AOA	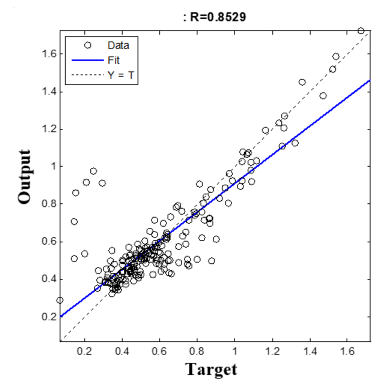
3	C_L' = 0.557 + 0.239*v2 + 0.557*v1*v2 + 0.488* cos(0.150 *AOA) + 0.239*v1*v2^2 + 0.120*v2* cos(0.150*AOA) - 0.011*v2*AOA - 0.014 *AOA *cos(0.150*AOA)	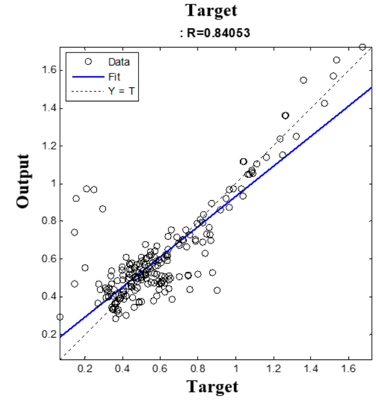

4	C_L' = 0.554 + v1 + 0.404*v2 + 0.554* cos (0.161 *AOA) *sin(0.385*v2 + 5.140/AOA) - 0.005*AOA - 0.014*v2*AOA	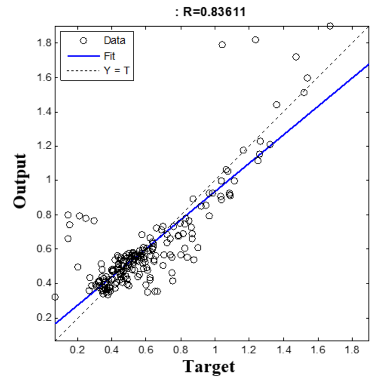

ANN model is selected in this study as a surrogate model for objective function evaluation due to its proven accuracy in capturing complex function that has multiple local peaks if it is properly trained (Bitsuamlak et al. [30]). ANN model is trained with CFD generated aerodynamic data corresponding to different combinations of geometric parameters (v_1, v_2) and AOAs (i.e. a total of 200 samples). As part of the quality check, different sizes of training samples are used to train the ANN model to determine the minimum size of samples which provides a satisfactory accuracy, as shown in Figure 4-8. 70% of the samples are used to train the ANN, 30% are used to validate and test the ANN model. The ANN estimates the objective functions with sufficient accuracy. Figure 4-9a shows the error distribution, Figure 4-9b shows the regression plot of the ANN model. The ANN based objective function evaluation error does not exceed 5% in 60% of the samples used. The correlation coefficient between the ANN predicted objective function and the CFD aerodynamic database is found to be 0.979. This confirms the adequacy of the ANN for mapping highly complex functions when trained using a large number of samples covering wide search domain (through a random approach of selecting these samples).

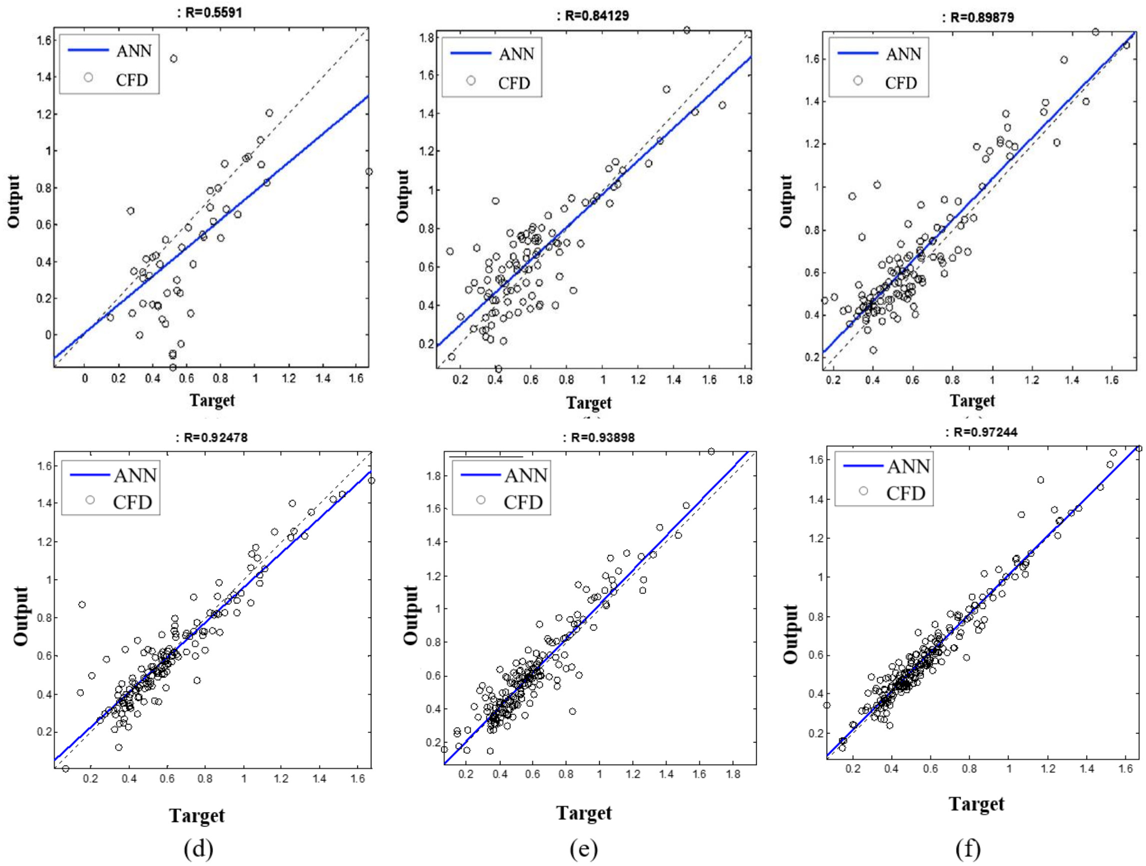

Figure 4-8 Regression plots for different sizes of training samples; (a) 50 samples (b) 100 samples (c) 125 samples (d) 150 samples (e) 175 samples and (f) 200 samples

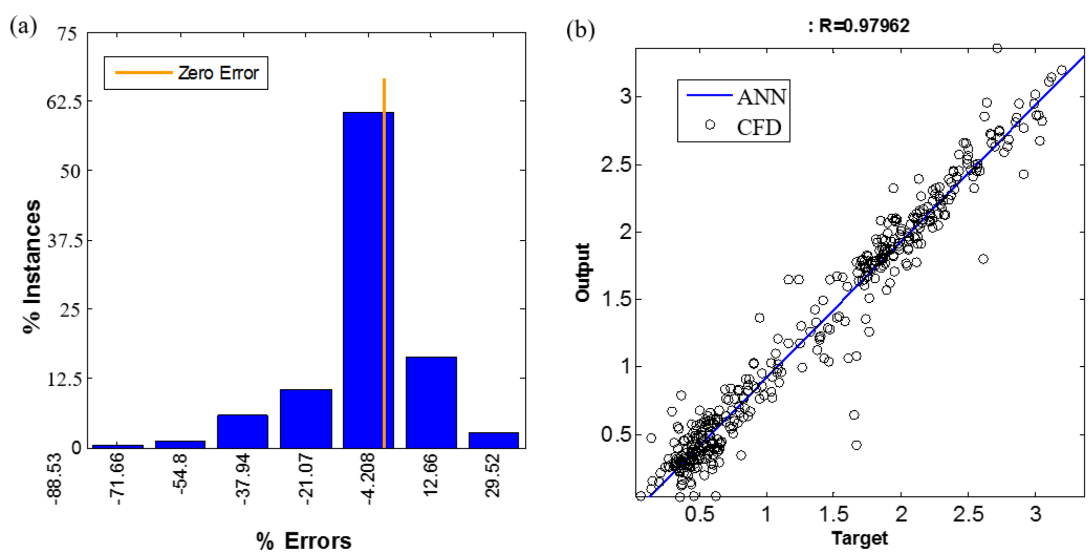

Figure 4-9 (a) Error distribution and (b) regression plot for the ANN model

4.3.3 LES properties of an ABL flow

Three-dimensional LES of the ABL flow (turbulent 3D flow) are conducted for the optimal and near optimal cross-sections to verify the accuracy of 3D LES of 2D flow trained ANN in the aerodynamic optimization procedure. The adopted length and time scales are 1:400 and 1:100, respectively, with a mean wind velocity of 10 *m/s* at the building height. Computational domain dimensions are chosen based on the recommendation of Franke et al. [43] and Dagnew and Bitsuamlak [24]. CDRFG technique [29] is utilized to generate turbulent inflow. The generated wind velocity and turbulence profiles follow ESDU [46] assuming open terrain exposure. Figure 4-10 shows the velocity, the turbulence intensity and the turbulence length scale profiles used for generating the inflow fields using CDRFG technique. The sides and the top of the computational domain are assigned as symmetry plane boundary condition, while the bottom of the computational domain and all building faces are defined as no-slip walls.

The employed grid zones and sizes are similar to those adopted by the authors (Aboshosha et al. [29]; Elshaer et al. [27]), which was previously validated with wind tunnel results and other CFD simulations from literature. Figure 4-11 shows the computational domain dimensions and the boundary conditions for the LES. Polyhedral control volumes are used to discretize the computational domain. The utilized grid sizes are divided into three zones based on the flow structures that required to be captured. Zone 1 is located away from the building of interest where the grid size is maximum. Zone 3 is located close to the building of interest where finer grid size is utilized to capture important flow details of in the wake zone and the zone around the study building. Zone 2 is located between zone 1 and 3 where intermediate grid size is used. Fifteen prism layers (i.e. surface following grids) parallel to the study building surfaces with stretching factor of 1.05 are utilized in zone 3 satisfying the recommendations by Murakami [47], Franke et al. [43] and Tominaga et al. [48]. Figure 4-12 shows the utilized grid in the LES for the current study. The simulations are conducted using a commercial CFD package (STAR-CCM+ v.10.06 [41]) employing LES with dynamic sub-grid scale model by Smagornisky [44] and Germano et al. [45]. Each simulation is resolved for 4,000 time steps representing 2 seconds in model-scale (i.e. 3.5

minutes in full-scale). The computational time required for each simulation is 3 hours on 128 processors cluster.

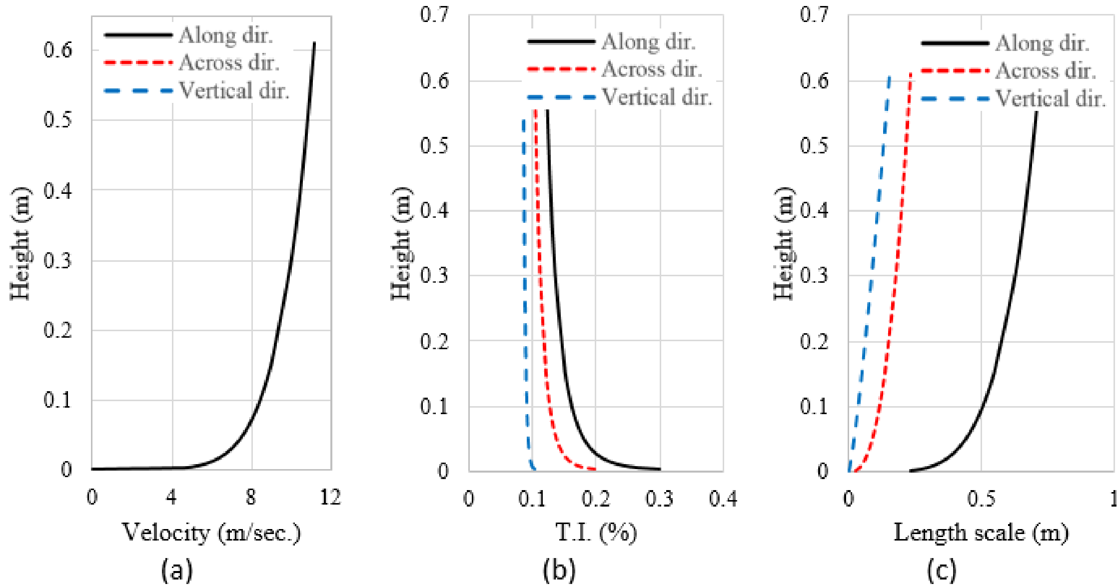

Figure 4-10 (a) velocity, (b) turbulence intensity and (c) turbulence length scale profiles used for inflow generation using CDRFG technique

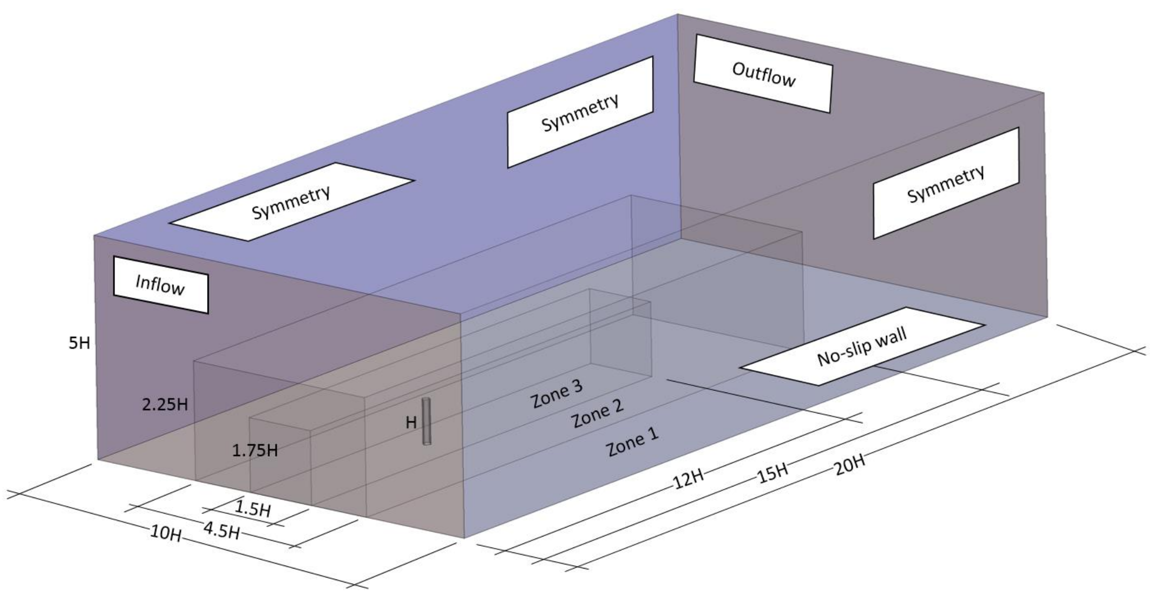

Figure 4-11 Computational domain dimensions and boundary conditions

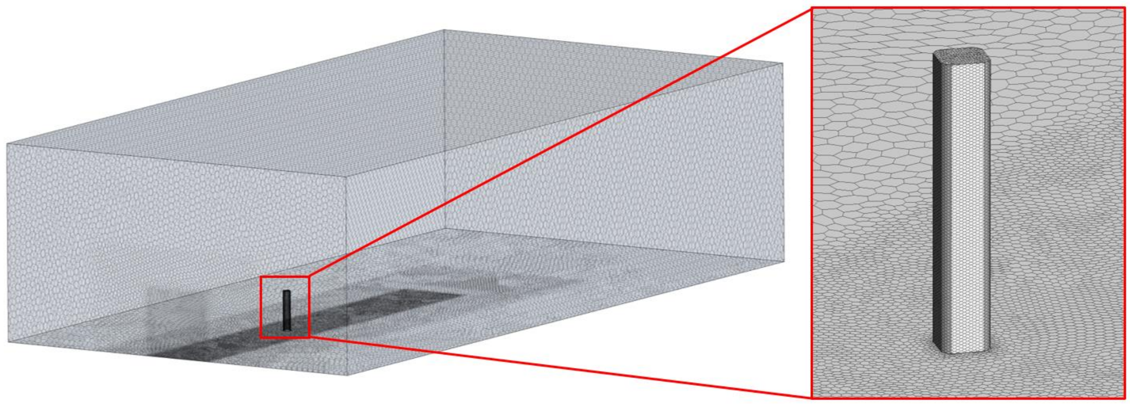

Figure 4-12 Grid resolution utilized for the ABL flow simulations

The validation for the CFD simulation in the current study is conducted for a tall building of v_1 = 1.0 and v_2 = 0. After obtaining the time histories for the base moments from the LES, the smoothed Power Spectral Density (PSD) plots are compared to those obtained from the wind tunnel (Zhou et al. [49]), as shown in Figure 4-13. It is found that the PSD obtained from the LES is in a good agreement with those obtained from the wind tunnel testing.

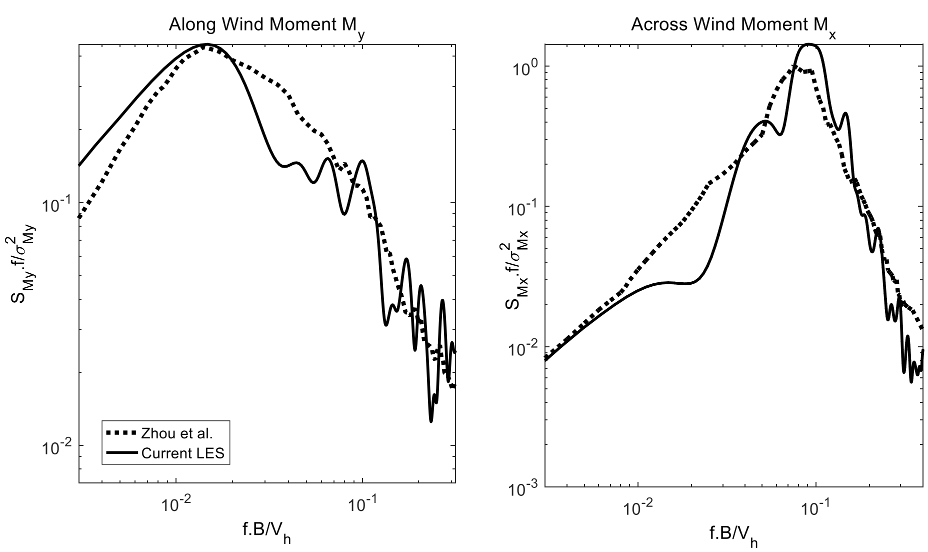

Figure 4-13 Spectra of the base moments in the (a) along-wind and (b) across-wind directions

4.3.4 Optimization algorithm properties

As mentioned earlier, a real coded genetic algorithm is adopted for optimization where the design variables are coded as real numbers. The optimization procedure starts by randomly selecting 50 candidates to form the initial population. Different types of crossover and mutation operators are applied to this population to produce new generations. The GA technique requires precise selection of crossover and mutation operators. Crossover operators combine high fitness parents to produce better offsprings in order to improve the solution over generations. Three types of crossover operators are utilized, which are arithmetic, uniform and heuristic. In contrast, mutation operators alter the design variables of low fitness candidates to produce offsprings that search unexplored areas of the search space to avoid trapping in a local minimum. Three types of mutation operators are used, which are uniform, non-uniform and boundary. The operators are applied on one third of the total size of the population. Details of the operators can be found in Michalewicz and Fogel [50]. The required number of generations is found to be 40 where no improvement is obtained by increasing the number of generations. The optimization procedure is repeated four times to confirm convergence to the same optimal solution thus avoiding trapping in a local minimum.

4.4 Optimization results and verification discussions

4.4.1 Optimization results and discussions

The optimization procedure is conducted for the two optimization examples until the optimal solutions are obtained after 40 generations. Figure 4-14 shows the fitness curves for the optimization examples where the objective function value of the best fitness candidate in each generation is plotted versus the generation number. This figure illustrates the improvement of the aerodynamic properties (objective functions) over optimization generations. For optimization Example 1, the mean drag coefficient ($\overline{C_D}$) of the optimal cross-section is 1.335, which is 30% lower than that of sharp edge square. While for Example 2 the standard deviation of the lift coefficient ($C_L{}'$) of the optimal solution is 0.503. The optimal solution lowered the $C_L{}'$ by 24% compared to that of sharp edge square.

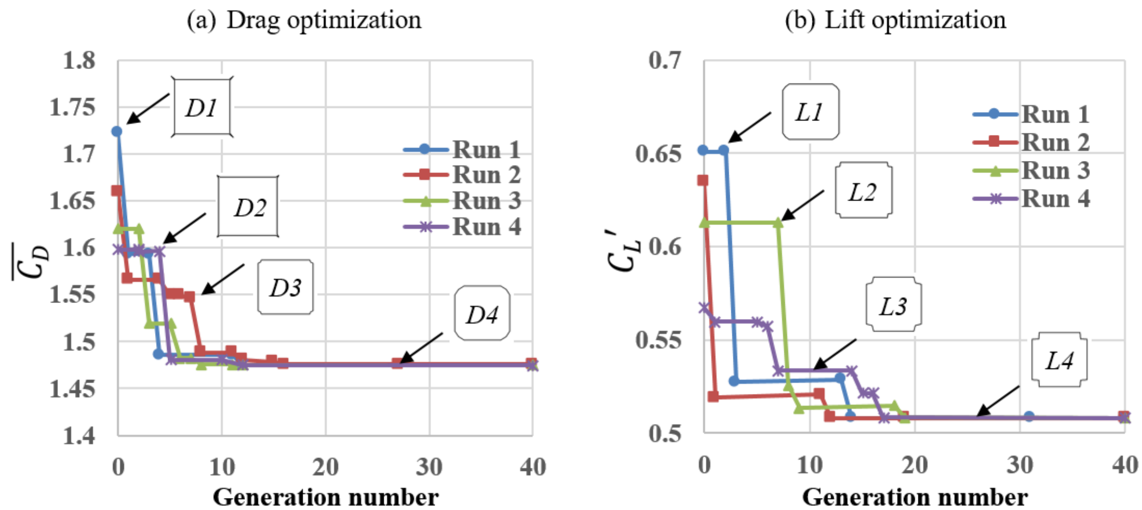

Figure 4-14 Fitness curves for the (a) drag and (b) lift optimization examples

Once the relative performance of the cross-sections is identified, the real aerodynamic performances of the optimal and near optimal cross-section is verified through detailed 3D LES of an ABL flow to verify the aerodynamic improvement resulted from the optimization procedure. Additional three near optimal cross-sections selected from the fitness curve in each optimization example are compared with the optimal solution. Figure 4-15 summarizes the design variables of the selected cross-sections as well as the optimal cross-section for drag and lift optimization examples. Figure 4-16 shows surface plots of the objective functions evaluated using the ANN model. It can be visually inferred that the optimization algorithm is able to locate the global optimal solution without being trapped in a local minimum.

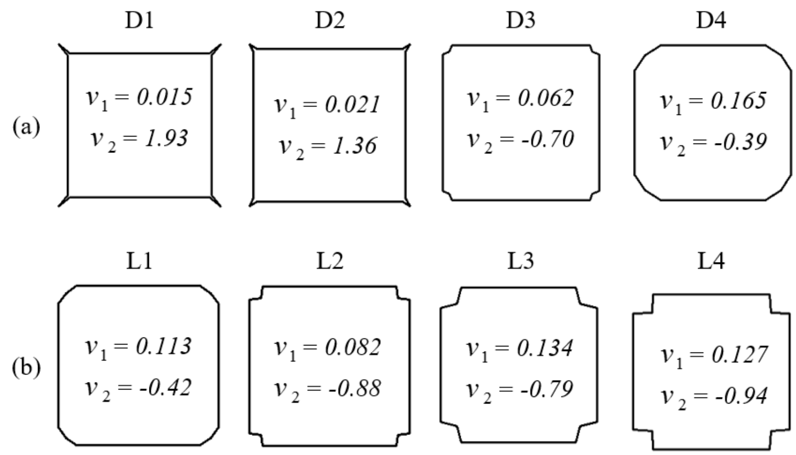

Figure 4-15 Selected cross-sections from (a) drag and (b) lift optimization examples

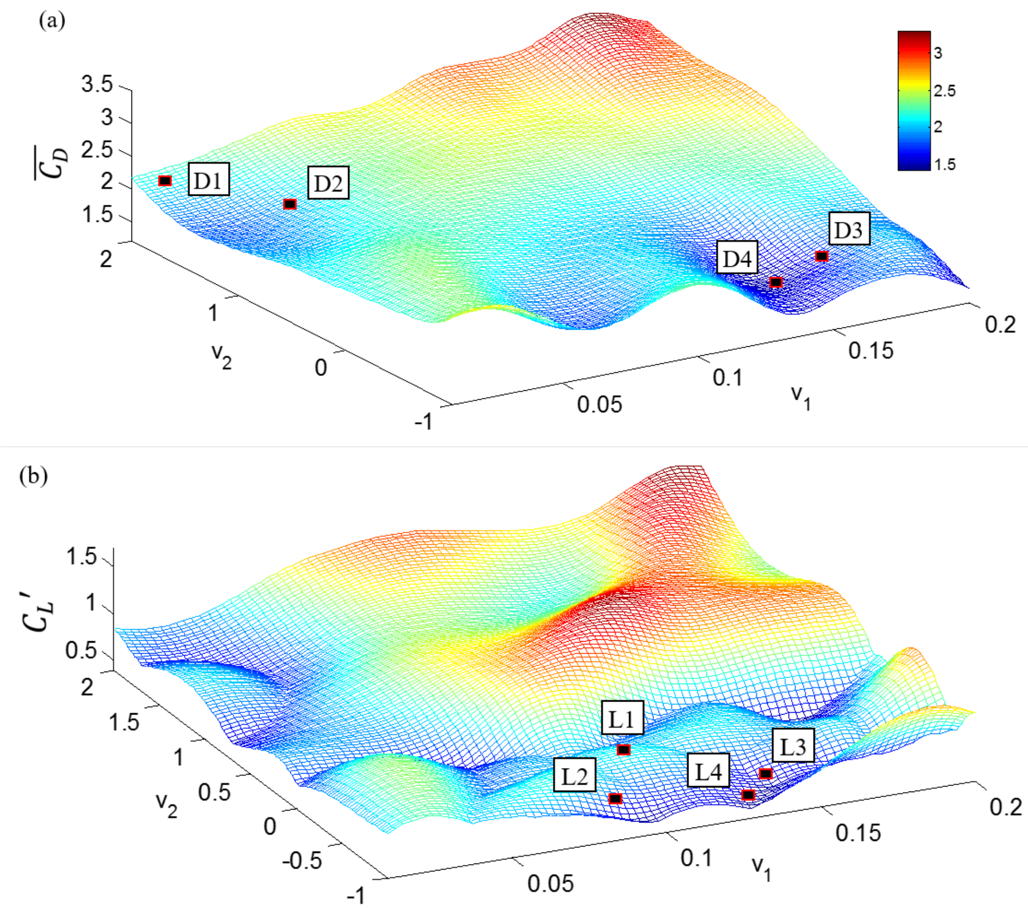

Figure 4-16 Surface plot for the ANN model of the (a) mean drag and (b) fluctuating lift coefficients

4.4.2 Verification and wind load evaluation results

As discussed before, at a verification stage the results of the optimal and near optimal cross-sections are compared to verify the aerodynamic improvement achieved throughout the AOP. The verification is carried out using a highly accurate 3D LES of an ABL flow adopting the recently developed approach (CDRFG), developed by the authors in Aboshosha et al. [29]. The simulations are carried out for the critical wind directions. For the drag optimization example, the mean velocity contours of the optimal (D4) and near optimal (D1) cross-sections are compared, as shown in Figure 4-17. It is noted that the wake size in D4 is smaller compared to the one in D1, which is a visual indicator of the reduction in drag attained from the AOP. This improvement will be reflected on the building responses that will be shown later. Similarly, for lift optimization, the instantaneous velocity contour for the optimal (L4) and near optimal (L1) cross-sections are compared in Figure 4-18 to show the fluctuation in the lateral velocities caused by the vortex shedding. The size of the eddies produced by the vortex shedding in the optimal cross-section (L4) is smaller than that of the near optimal one. This shows qualitatively the reduction in the fluctuating lateral forces. Quantitative verifications are discussed in the next section.

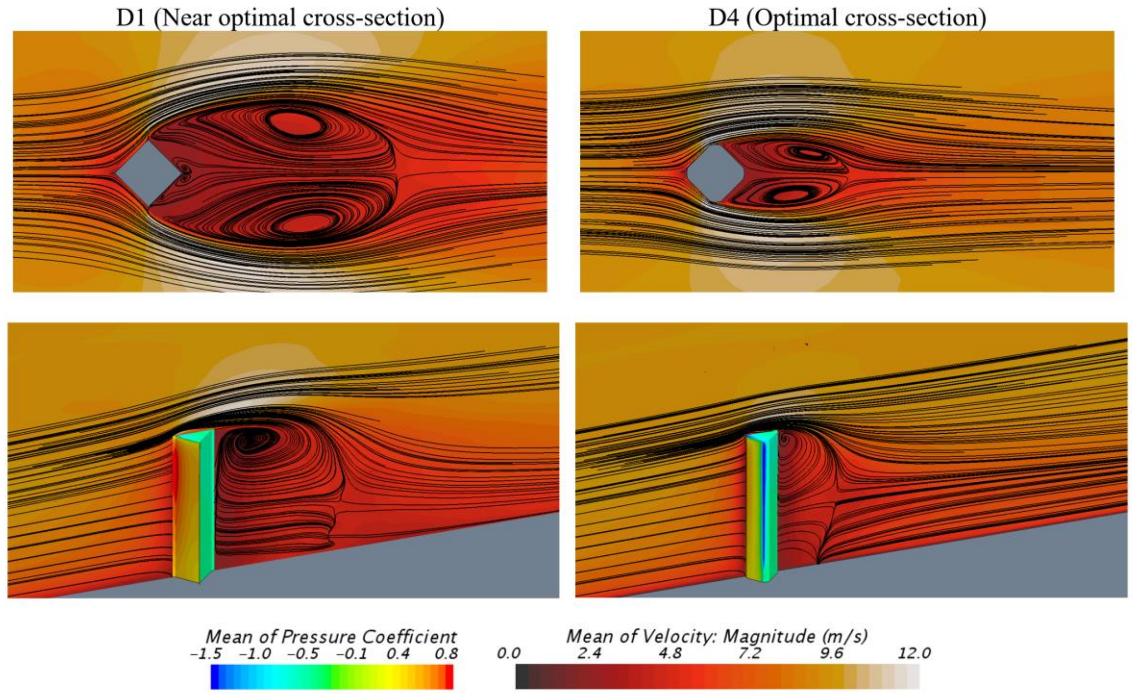

Figure 4-17 Mean velocity & Cp distribution for the drag optimal (D4) & near optimal (D1) cross-sections

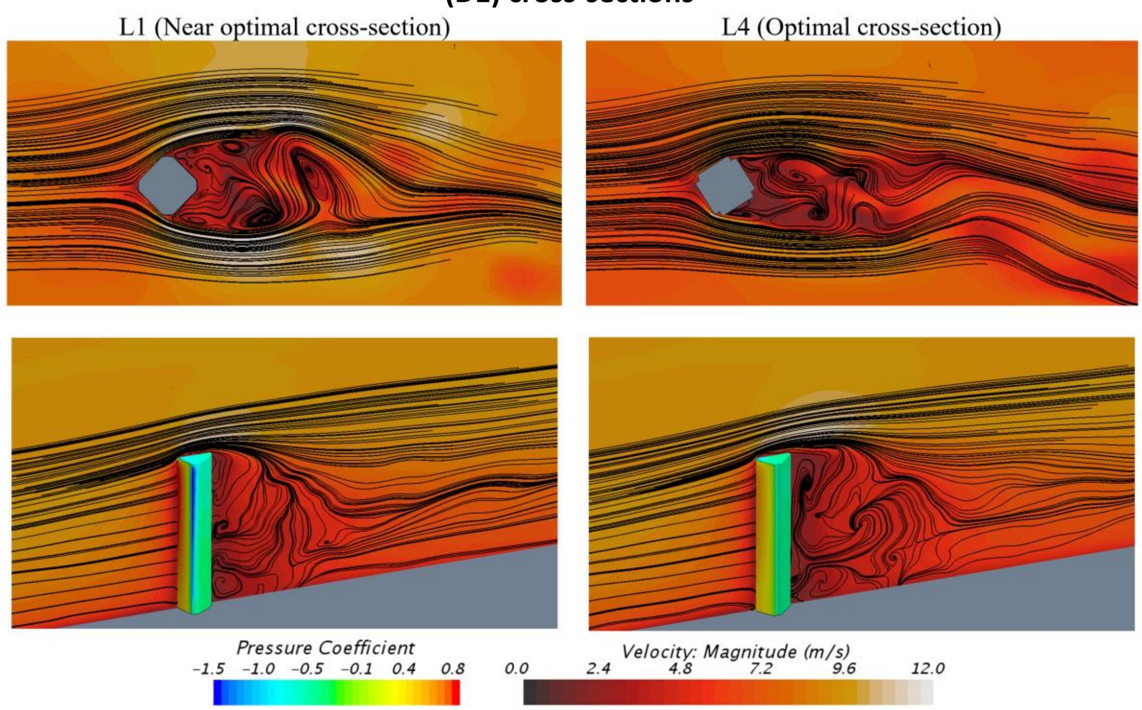

Figure 4-18 Instantaneous velocity field & Cp distribution for the lift optimal (L4) & near optimal (L1) cross-sections

The mean drag and the fluctuating lift from the 2D flow LES is compared to the high accurate ABL flow. Figure 4-19 shows the $\overline{C_D}$ of cross-sections from drag optimization normalized by the $\overline{C_D}$ of the optimal cross-section resulted from LES of the 2D and ABL flow. While Figure 4-20 shows the $C_L{}'$ of cross-sections from lift optimization normalized by the $C_L{}'$ of the optimal cross-section resulted from LES of the 2D and ABL flow. Despite the discrepancy in the inflow profiles and values between 2D and ABL flow simulations, the normalized $\overline{C_D}$ and $C_L{}'$ resulting from both analyses follow a similar trend. This indicates the capability of low-dimensional CFD models in assessing the relative aerodynamic performance of various aerodynamic modifications, which agrees with Tamura and Miyagi [9] and Kareem et al. [21].

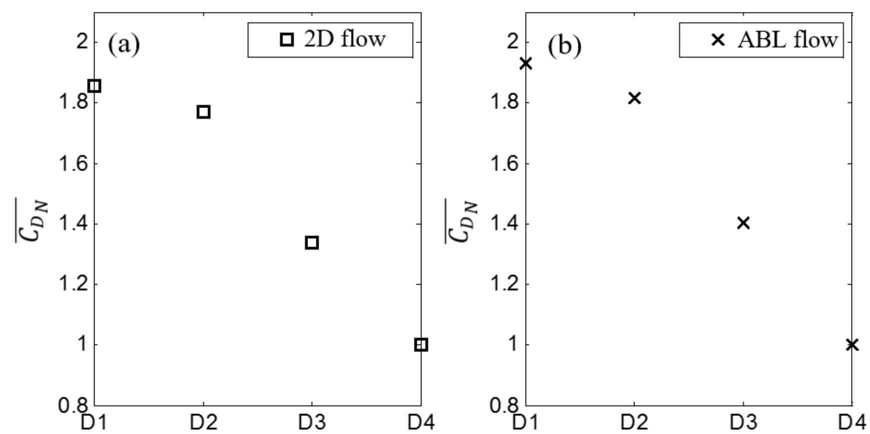

Figure 4-19 Normalized mean drag coefficients and of cross-sections from drag optimization using (a) 2D flow and (b) ABL flow

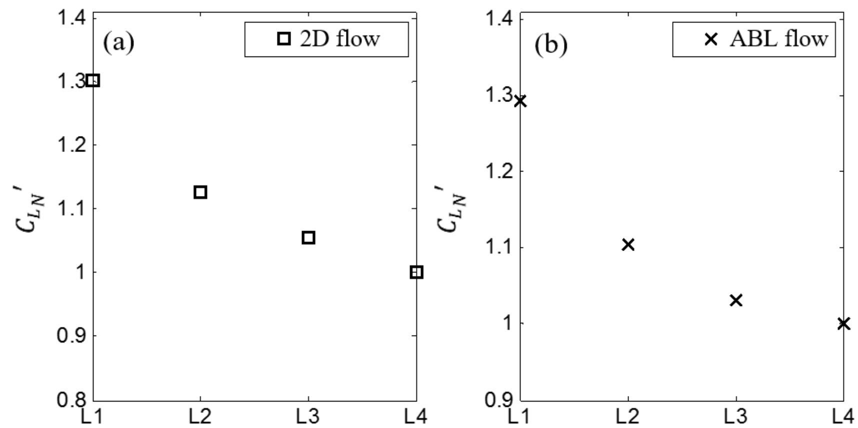

Figure 4-20 Normalized Fluctuating lift coefficients of cross-sections from lift optimization using (a) 2D flow and (b) ABL flow

Figure 4-21a shows the time histories of the normalized along-wind moment for the cross-sections from drag optimization example, while Figure 4-21b shows the time histories of the normalized across-wind moment for the cross-sections from lift optimization example. The base moments are normalized using Equation 4-3. At it can be noticed, the along-wind moment is decreases for higher fitness drag cross-sections, while the fluctuation in the across-wind moments decreases for higher fitness lift cross-sections.

$$M_{yref} = \frac{1}{2}\rho V_h^{2} B_y H^{2}, M_{xref} = \frac{1}{2}\rho V_h^{2} D_x H^{2}$$ Equation 4-3

where V_h is the mean velocity at the building height, ρ is the air density which is taken equal to 1.25 kg/m^3, B_y is the building width (normal to wind direction) and D_x is the building depth (along wind direction)

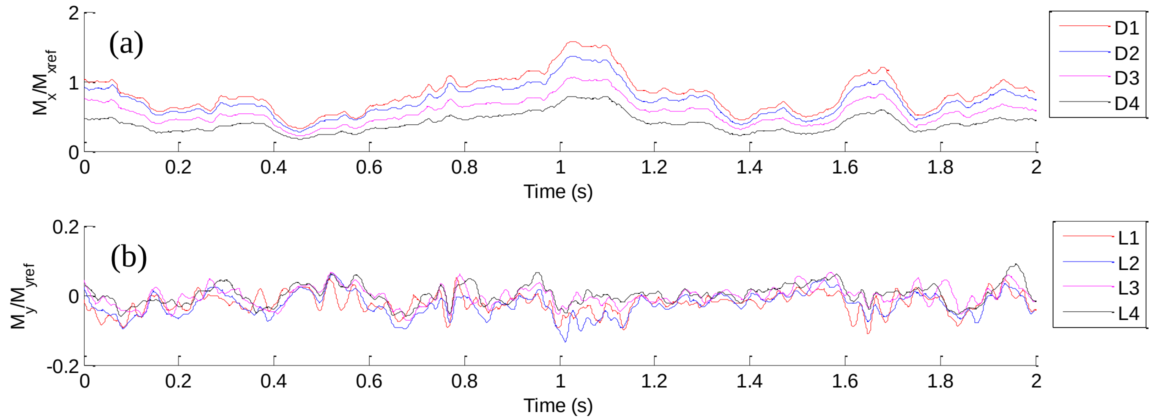

Figure 4-21 Base moment time histories around (a) x-axis (along-wind) of cross-sections from drag optimization and (b) around y-axis (across-wind) of cross-sections from lift optimization

Figure 4-22 shows the smoothed Power Spectral Density (PSD) plots, which illustrates the energy distribution corresponding to each frequency. The PSD plots are computed for the optimal shapes and the other near optimal cross-sections from both optimization examples. As shown in this figure, the aerodynamic improvement can be observed for the optimal shape compared to the near optimal ones. For the lift optimization example, it is also noticed that, the optimal cross-sections (L4) has a broader peak than the near optimal cross-sections, which reflects the reduction in the energy associated with the vortex shedding frequency.

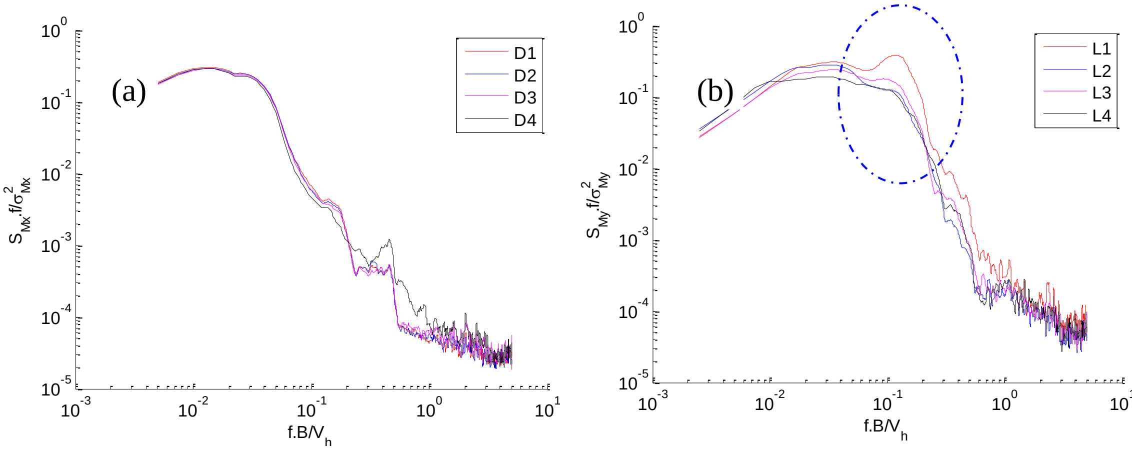

Figure 4-22 Base moments spectra (a) around x-axis (along-wind) of cross-sections from drag optimization and (b) around y-axis (across-wind) of cross-sections from lift optimization

PSD are used to evaluate the dynamic responses for different cross-sections using the method described by Kijewski and Kareem [51] and Chen and Kareem [52]. Table 4-3 summarizes the dynamic properties used in evaluating the dynamic responses. It is assumed that no coupling occurs between the modes of the responses. In cases where there is a significant coupling between modes of the responses, more accurate approaches can be utilized for evaluating the dynamic responses, such as the approaches described in Chen and Huang [53] and Cui and Caracoglia [54]. For each shape, the center of mass and rigidity of the building are assumed to coincide. Building responses are evaluated at the center of mass of each floor. Equation 4-4 is utilized to evaluate the peak responses.

$$R_{peak} = R_{mean} + g_f * R_{rms} \quad \text{Equation 4-4}$$

where R is the building response and g_f is a peak factor that is taken equal to 3.5.

For the drag optimization example, the peak top displacement, acceleration and the base moment are plotted in Figure 4-23 in the along-wind direction. The optimal cross-section (D4) shows lower values of dynamic responses than other near optimal cross-sections by 29%. Similarly, for the lift optimization, Figure 4-24 plots the peak top displacement, acceleration and the base moment in the across-wind direction. The figure indicates up to 52% reduction in the dynamic responses of the optimal cross-section (L4) compared to near optimal cross-sections. This reduction in wind-induced motion and forces will result in a considerable savings in the required building materials, damping systems and consequently the building cost.

Table 4-3 Dynamic properties of the examined building

Property	Value
Height *H*, Width B_y, Depth D_x	120, 20, 20 m
Natural Frequency	0.15 (along-wind), 0.15 (across-wind), 0.3 (torsional)
Damping ratio	1% for all modes
Mass per unit volume m_s	160 kg/m^3

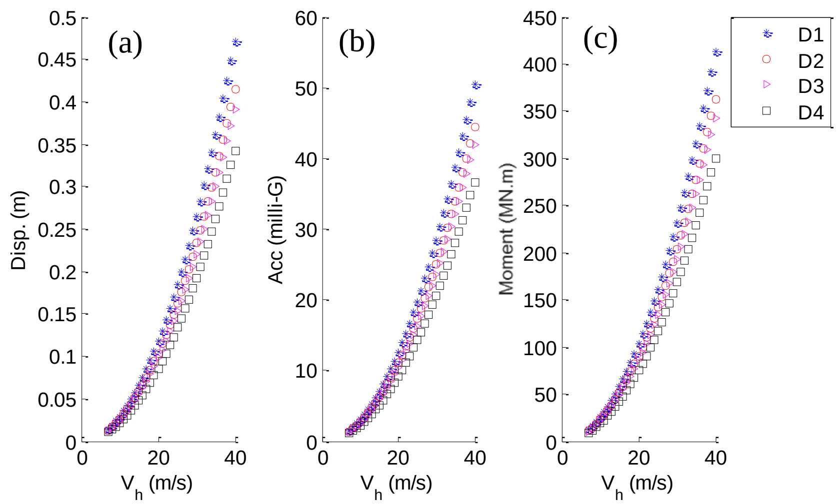

Figure 4-23 (a) Peak top floor displacement, (b) acceleration and (c) base moments in the along-wind direction of cross-sections from drag optimization

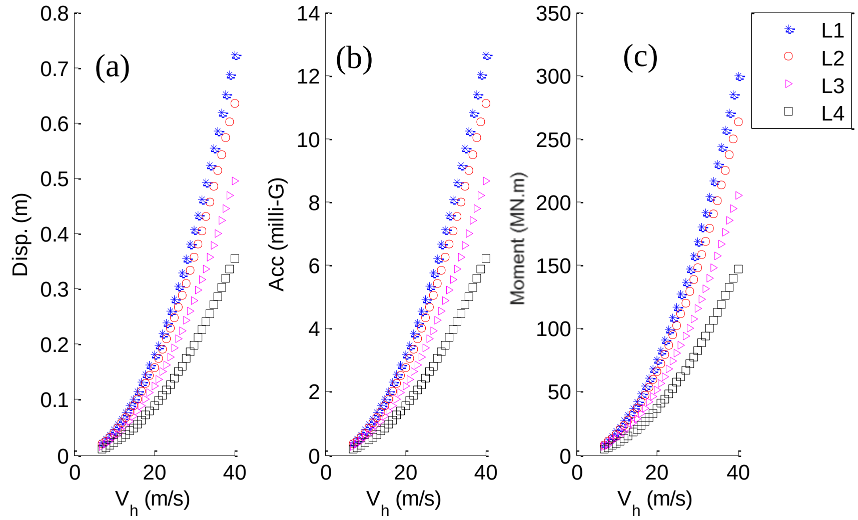

Figure 4-24 (a) Peak top floor displacement, (b) acceleration and (c) base moments in the across-wind direction of cross-sections from lift optimization

4.5 Conclusions

The current study introduces a robust aerodynamic optimization procedure that combines Genetic Algorithm, Large Eddy Simulation and Artificial Neural Network models. During the optimization procedure, ANN model is used to evaluate the objective function once trained with the aerodynamic data generated through 3D LES analyses of a 2D flow. Two optimization examples are presented to demonstrate the proposed optimization procedure aiming at reducing the drag and lift forces, respectively. A final verification is carried out through 3D LES analyses of ABL flow interaction with the optimal and the near optimal building cross-sections. Aerodynamic properties of the near optimal shapes are compared to other cross-sections the following conclusions are deduced:

1. Comparison of the aerodynamic behavior of the optimal building shape to the other near optimal ones using 3D LES of both 2D flow and ABL flows shows a similar trend. Thus, low-dimensional flow analyses could be sufficient to indicate the relative performance of the shapes with a more time-efficient analyses (i.e. around 150 times faster than ABL flow analyses).

2. The surrogate ANN model is capable of capturing complex variations in the objective function and fitting the training database with a correlation coefficient of 0.979, and its use accelerates the optimization process significantly.

3. For the drag optimization example, the mean drag coefficient ($\overline{C_D}$) is lowered by 30% for the optimal shape compared to the sharp edge corner. For the lift optimization example, the standard deviation of the lift coefficient ($C_L{}'$) is reduced by 24% for the optimal corner as compared to the sharp edge one.

4. The optimal cross-section, in the drag optimization problem, shows lower dynamic responses compared to other near optimal shapes by 29%. Whereas, the lift optimization results in a 52% reduction in the dynamic responses compared to other near optimal shapes.

5. In general, the aerodynamic optimization efficiency coupled with the encouraging development in computational capacity is expected to encourage architects, urban planners and engineers to seek for more optimal solutions while designing building for climate.

4.6 References

[1] Vickery BJ. Fluctuating lift and drag on a long cylinder of square cross-section in a smooth and in a turbulent stream. Journal of Fluid Mechanics 1966; 25, 481-494

[2] Lee BE. The effect of turbulence on the surface pressure field of a square prism. Journal of Fluid Mechanics 1975; 69, 321-352.

[3] Okajima A. Strouhal numbers of rectangular cylinders. Journal of Fluid Mechanics 1982; 123, 379 - 398.

[4] Igarashi T. Characteristics of the flow around a square prism. Bulletin of JSME 27, 1984; 1858-1865.

[5] Nakamura Y, Ohya Y. The effects of turbulence on the mean flow past two-dimensional rectangular cylinders. Journal of Fluid Mechanics 1984; 149, 255-273.

[6] Merrick R, Bitsuamlak, GT. Shape effects on the wind-induced response of high-rise buildings. Journal of Wind Engineering 2009; 6 (2), 1-18.

[7] Kwok KCS. Effects of building shape on wind-induced response of tall buildings. Journal of Wind Engineering and Industrial Aerodynamics 1988; 28, 381-90.

[8] Kareem A, Kijewski T, Tamura Y. Mitigation of motions of tall buildings with specific examples of recent applications. Wind and structures 1999; 2(3), 201-251.

[9] Tamura T, Miyagi T. The effect of turbulence on aerodynamic forces on a square cylinder with various corner shapes. Journal of Wind Engineering and Industrial Aerodynamics 1999; 83, 135-145.

[10] Carassale L, Freda A, Marrè-Brunenghi M. Experimental investigation on the aerodynamic behavior of square cylinders with rounded corners. Journal of Fluids and Structures 2014; 44, 195-204.

[11] Kawai H. Effects of corner modifications on aeroelastic instabilities of tall buildings. Journal of Wind Engineering and Industrial Aerodynamics 1998; 74-76, 719-29.

[12] Gu M, Quan Y. Across-wind loads of typical tall buildings, Journal of Wind Engineering and Industrial Aerodynamics 2004; 92, 1147-65.

[13] Tse KT, Hitchcock PA, Kwok KCS, Thepmongkorn S, Chan CM. Economic perspectives of aerodynamic treatments of square tall buildings. Journal of Wind Engineering and Industrial Aerodynamics 2009; 97(9), 455-467.

[14] Kwok KCS, Bailey PA. Aerodynamic devices for tall building and structures. Journal of Engineering Mechanics, ASCE 1987; 111(4), 349-65.

[15] Kwok KCS, Wilhelm PA, Wilkie BG. Effect of edge configuration on wind-induced response of tall buildings. Engineering Structures 1988; 10, 135-140.

[16] Tamura T, Miyagi T, Kitagishi T. Numerical prediction of unsteady pressures on a square cylinder with various corner shapes, Journal of Wind Engineering and Industrial Aerodynamics 1998; 74-76, 1, 531-542.

[17] Tanaka H, Tamura Y, Ohtake K, Nakai, M, Chul Kim Y. Experimental investigation of aerodynamic forces and wind pressures acting on tall buildings with various unconventional configurations, Journal of Wind Engineering and Industrial Aerodynamics 2012; 107-108, 179-191.

[18] Elshaer A, Bitsuamlak GT, El Damatty A. Wind Load Reductions due to Building Corner Modifications. 22nd Annual Conference of the CFD Society of Canada 2014; Toronto, Canada.

[19] Bernardini E, Spence S, Wei D, Kareem A. Aerodynamic shape optimization of civil structures: A CFD-enabled Kriging-based approach, Journal of Wind Engineering and Industrial Aerodynamics 2015; 144, 154-164.

[20] Kareem A, Bernardini E, Spence SMJ. Control of the Wind Induced Response of Structures. Springer, Tokyo, Japan 2013, 377-410 (Chapter14).

[21] Kareem A, Spence SMJ, Bernardini E, Bobby S, Wei D. Using computational fluid dynamics to optimize tall building design. CTBUHJ. (III) 2013; 38-42.

[22] Kareem A, Bobby S, Spence SMJ, Bernardini E. Optimizing the form of tall buildings to urban environments. In: CTBUH 2014 International Conference 2014.

[23] Nozawa K, Tamura T. Large eddy simulation of the flow around a low-rise building immersed in a rough-wall turbulent boundary layer. Journal of Wind Engineering and Industrial Aerodynamics 2002; 90, 1151-1162

[24] Dagnew A, Bitsuamlak GT. Computational evaluation of wind loads on buildings: a review, Wind and Structures 2013; 16(6), 629-660.

[25] Dagnew A, Bitsuamlak GT. Computational evaluation of wind loads on standard tall building using a large eddy simulation, Wind & Structures 2014; 18(5), 567-598.

[26] Aboshosha H, El Damatty A, Bitsuamlak GT. LES of wind in the built-environment: Inflow and roughness induced by fractal surfaces. Sustainable Cities and Society 2015; 19, 46-60.

[27] Elshaer A, Aboshosha H, Bitsuamlak GT, El Damatty A. LES evaluation of wind-induced responses for an isolated and a surrounded tall building. Engineering Structures 2016; 115, 179-195.

[28] Hajra B, Bitsuamlak G, Aboshosha H, Elshaer A. Large eddy simulation of wind induced loads on a low rise building with complex roof geometry. Canadian Society of Civil Engineers 2016; London, Canada.

[29] Aboshosha H, Elshaer A, Bitsuamlak GT, El Damatty A. Consistent inflow turbulence generator for LES evaluation of wind-induced responses for tall buildings. Journal of Wind Engineering and Industrial Aerodynamics 2015; 142, 198-216.

[30] Bitsuamlak BT, Stathopoulos T, Bédard C. Effect of topography on design wind load combined numerical and neural network approach. Journal of Computing in Civil Engineering, ASCE 2007; 21 (6), 384-392.

[31] Elshaer A, Bitsuamlak GT, El Damatty A. Aerodynamic shape optimization for corners of tall buildings using CFD. 14th International Conference on Wind Engineering 2015; Porto Alegre, Brazil.

[32] Elshaer A, Bitsuamlak GT, El Damatty A. Vibration control of tall buildings using aerodynamic optimization. 25th Canadian Congress of Applied Mechanics 2015; London, Canada.

[33] Jung S, Ghaboussi J, Kwon S. Estimation of Aeroelastic Parameters of Bridge Decks Using Neural Networks. Journal of Engineering Mechanics 2004; 130 (11), 1356-1364.

[34] Teng W, Kareem A. Modeling hysteretic nonlinear behavior of bridge aerodynamics via cellular automata nested neural network. Journal of Wind Engineering and Industrial Aerodynamics 2011; 99. 378-388.

[35] Lee C, Kim J, Babcock D, Goodman R. Application of neural networks to turbulence control for drag reduction. Physics of Fluids 1997; 9(6), 1740-1747.

[36] Mengistu T, Ghaly W. Aerodynamic optimization of turbomachinery blades using evolutionary methods and ANN-based surrogate models. Optimization and Engineering 2008; 9(3), 239-255.

[37] Zhou L, Haghighat F. Optimization of ventilation system design and operation in office environment, Part I: Methodology, Building and Environment 2009; 44, 4.

[38] El Ansary A, El Damatty A, Nassef A. Optimum Shape and Design of Cooling Towers. World Academy of Science. Engineering and Technology 2011; 9, 4-13.

[39] Goldberg D. Genetic Algorithms in search. Optimization and Machine Learning. Addison-Wesley Publishing Company, Inc. 1989, New York.

[40] Davis L. Handbook of Genetic Algorithms, Van Nostrand Reinhold 1991; New York.

[41] STAR CCM+, v.10.06, CD-ADAPCO Product, www.cd-adapco.com/products, 2016.

[42] SHARCNET is a consortium of colleges, universities and research institutes operating a network of high-performance computer clusters across south western, central and northern Ontario, 2016. [Online]. Available: www.sharcnet.ca.

[43] Franke J, Hellsten A, Schlünzen H, Carissimo B. COST. Best practice guideline for the CFD simulation of flows in the urban environment 2007; 732. Hamburg: University of Hamburg.

[44] Smagorinsky J. General circulation experiments with the primitive equations, I. the basic experiment. Monthly Weather Review 1963; 91, 99-164.

[45] Germano M, Piomelli U, Moin P, Cabot W. A dynamic subgrid-scale eddy viscosity model. Physics of Fluids 1991; 3(7), 1760-1765.

[46] Engineering Sciences Data Unit (ESDU) 85320. Characteristics of atmospheric turbulence near the ground. Part II: single point data for strong winds 2001.

[47] Murakami S. Overview of turbulence models applied in CWE-1997. Journal of Wind Engineering and Industrial Aerodynamics 1998; 74-76, 1-24.

[48] Tominaga Y, Mochida A, Yoshiec R, Kataokad H, Nozu T, Yoshikawa M, Shirasawa T. AIJ guidelines for practical applications of CFD to pedestrian wind environment around buildings. Journal of Wind Engineering and Industrial Aerodynamics 2008; 96(10-11), 1749-1761.

[49] Zhou Y, Kijewski T Kareem A. Aerodynamic Loads on Tall Buildings: Interactive Database. Journal of Structural Engineering: ASCE 2003; 3, 394-404.

[50] Michalewicz Z, Fogell D. How to solve it: modern heuristics. Springer Science & Business Media 2013.

[51] Kijewski T, Kareem A. Dynamic wind effects: a comparative study of provisions in codes and standards with wind tunnel data. Wind and Structures 1998; 1(1), 77-109.

[52] Chen X, Kareem A. Dynamic wind effects on buildings with 3-D coupled modes: application of HFFB measurements. Journal of Engineering Mechanics 2005; ASCE, 131(11), 1115-1125.

[53] Chen X, Huang G. Evaluation of peak resultant response for wind-excited tall buildings. Engineering Structures 2009; 31(4):858-68.

[54] Cui W, Caracoglia L. Simulation and analysis of intervention costs due to wind-induced damage on tall buildings. Engineering Structures 2015; 87:183-197.

Chapter 5

5 Aerodynamic shape optimization of tall buildings using twisting and corner modifications

5.1 Introduction

Wind-induced loads and vibrations are major aspects in the design of tall buildings. The wind-structure interaction induced responses are affected by several factors including the upcoming wind, surrounding conditions, structural properties of the building and its outer shape. Precise selection of the outer shape details of a building can result in a significant reduction in forces and motions caused by wind. Improving the aerodynamic performance of a tall building can be achieved by local and global shape mitigations. Local shape mitigations, such as corner mitigations, have a considerable effect on structural and architectural design, while global shape mitigations have a minor effect on structural and architectural design. Those mitigations were previously studied in various boundary layer wind tunnel (BLWT) tests (e.g. Kwok 1998, Tanaka et al. 2012, Carassale et al. 2014) and numerical studies using Computational Fluid Dynamics (CFD), such as Tamura et al. 1998 and Elshaer et al. 2014. Although very important improvement on wind performance was reported in these studies, they fail short in estimating the optimal building shape within predefined geometric parameters controlling the outer shape of a building. Thus, more aerodynamic improvement can be reached by integrating an optimization technique to the mitigation studies. This was reported by Kareem et al. 2013, Bernardini et al. 2015 and Elshaer et al. (2015a, b).

An aerodynamic optimization procedure (AOP) was recently developed by the authors based on training an Artificial Neural Network (ANN) model using a CFD database for random shapes having different design variables to evaluate the objective function values. The design variables represent the geometric parameters controlling the outer shape of the building, while the objective function values represent the target aerodynamic properties to be improved in the optimization process such as drag or lift. The ANN model is utilized as a surrogate model for objective function evaluation. Using the ANN model in the AOP (i) significantly reduces the computational time, (ii) eliminates the need for the direct integration of CFD solver within the AOP and (iii) eases the utilization of available experimental BLWT results in conjunction with the CFD database. The developed approach considered the wind directionality by examining all possible angles of attack during the AOP. In the current research, the aerodynamic properties are obtained using 3D LES analysis of an atmospheric boundary layer (ABL) flow to capture the complex flow structures associated with the turbulent ABL flow interaction with the tall building.

5.2 Aerodynamic optimization procedure (AOP) framework

The AOP procedure begins by defining the objective function, which is the aerodynamic property targeted to be minimized or maximized. The value of the objective function for each case depends on the building geometry, which is controlled by the optimization design variables. Then, the optimization algorithm (genetic algorithm) is used to find the optimal combination of design variables that reduces the wind loads on the building. Optimization procedure requires multiple evaluations for the objective functions during the iterative procedure of the optimization. The evaluation of the objective function is conducted using the ANN model that had been previously trained using CFD simulations. After predicting the optimal building shape, a verification step is carried out by comparing the optimal solution to lower fitness shapes using wind tunnel testing or high accuracy CFD simulations. The proposed procedure was previously examined by the authors on local corner modifications (Elshaer et al. 2015). Figure 5-1 summarizes the framework of the proposed AOP.

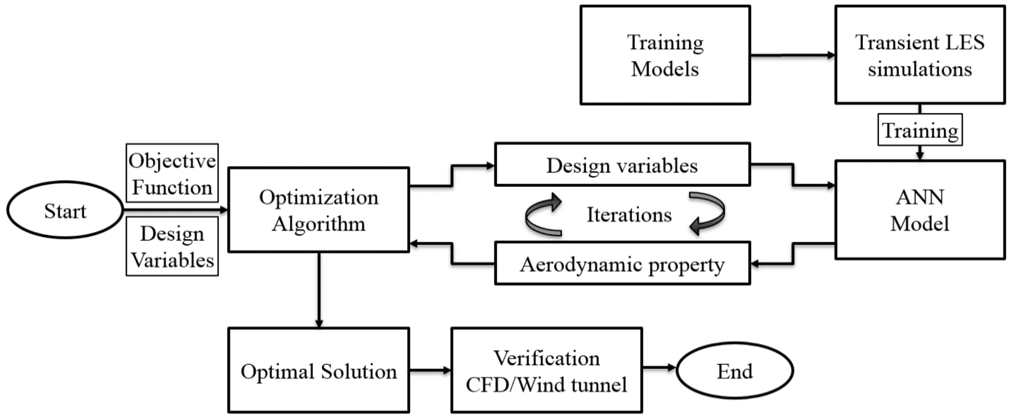

Figure 5-1 Framework of the aerodynamic optimization procedure (AOP)

5.3 Illustration example

An illustrative example is conducted to examine the efficiency of the proposed framework in reducing the along-wind base moment through corner modifications and helical twisting of a typical tall building. The objective function is set to be the normalized moment coefficient in the along-wind direction, which is computed using Equation 5-1. Different wind angles of attack are taken into consideration. The critical wind angle of attack is utilized to evaluate the objective function value. The basic building cross-section is chosen to be a square of 50 mm side length similar to previous wind tunnel studies from the literature (Tamura et al. 1998, Kawai 1998, Tamura and Miyagi 1999). The design variables (r_1, r_2 and θ) are defined to control the building shape, as shown in Figure 5-2. In order to keep the building shape in an accepted architectural shape, lower and upper bound are set for each design variable. In the present study, the lower bounds are set to be 0.005, 0.005 and 0 for r_1, r_2 and θ, respectively. While the upper bounds are set to be 0.01, 0.01 and 360, respectively.

$$C_{My,N} = \frac{M_y}{\frac{1}{2}\rho v_{ref}^2 B H^2} \quad \text{Equation 5-1}$$

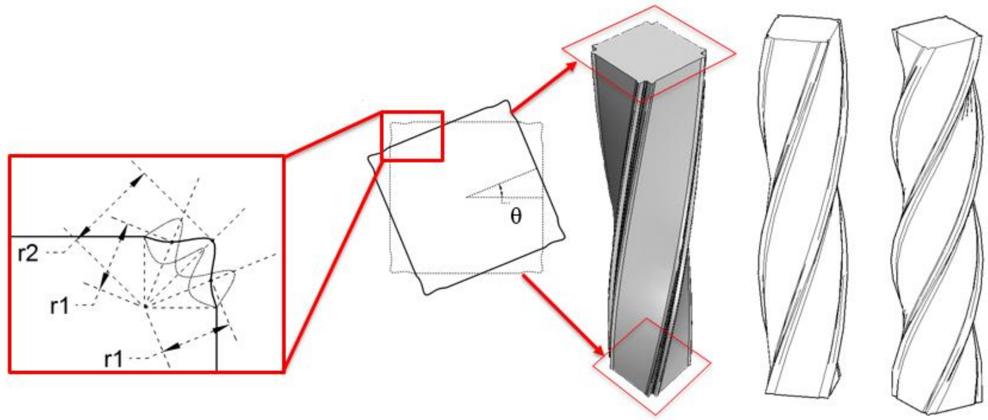

Figure 5-2 Geometric parameters (length in meters and angle in degree)

5.3.1 CFD model properties

3D LES analyses are conducted randomly selected shapes to act as seed for training the ANN. The length and time scales used are 1:400 and 1:100, respectively, with a mean wind velocity of 10 m/s at the building height. Computational domain dimensions are chosen based on the recommendation of Frank 2006 and Dagnew and Bitsuamlak 2013. The generated wind velocity and turbulence profiles are following ESDU 2011 assuming open terrain exposure. Figure 5-3 shows the velocity, the turbulence intensity and the turbulence length scale profiles used in the LES. The sides and the top of the computational domain are assigned as symmetry plane boundary condition, while the bottom of the computational domain and all building faces are defined as no-slip walls.

Polyhedral control volumes are used to discretize the computational domain. A number of 15 parallel grids to the study building surfaces with stretching factor of 1.05 is utilized satisfying the recommendations by Murakami 1997, and Tominaga et al. 2008. Figure 5-4 shows the utilized grid in the LES for the current study.

The simulations are conducted using a commercial CFD package (STAR-CCM+ v.10.06) employing LES with dynamic sub-grid scale model by Smagornisky 1963 and Germano et al. 1991. Each simulation is resolved for 1,500 time steps representing 0.75 seconds in model-scale (i.e. 1.25 minutes in full-scale). SharcNet high performance computer facility at the Western University is utilized for conducting the numerical simulations. The computational time required for each simulation is 3 hours on 128 processors. After running the LES analyses, the time history for the base moment in the along-wind direction is extracted. Figure 5-5 shows a sample from the extracted time histories. These time histories are utilized to train the ANN model for the objective function evaluation.

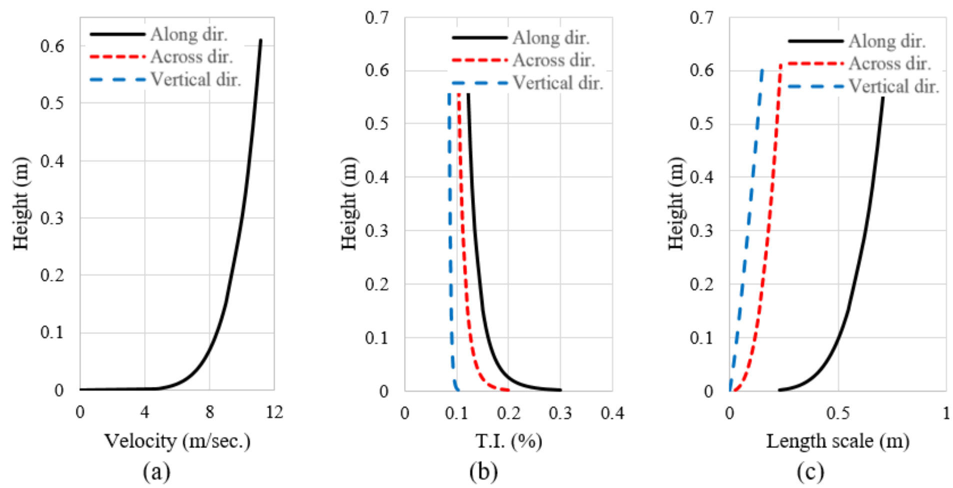

Figure 5-3 (a) velocity, (b) turbulence intensity and (c) turbulence length scale profiles used for inflow generation using CDRFG technique

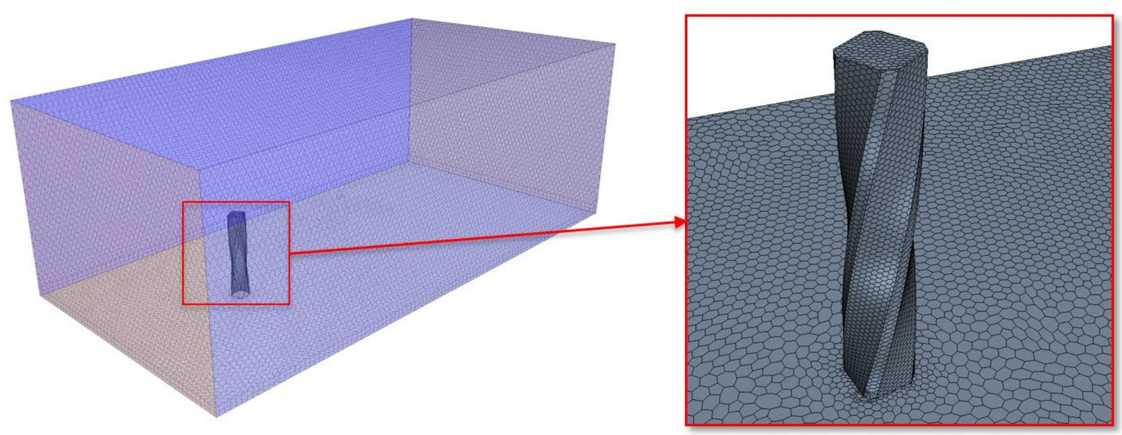

Figure 5-4 Grid resolution utilized for the LES analysis

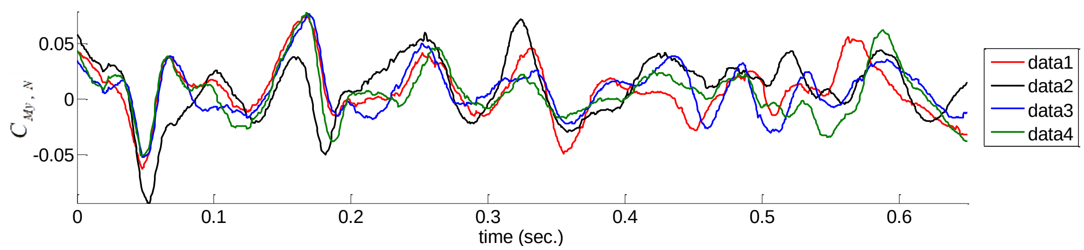

Figure 5-5 Normalized moment coefficient time history in the along-wind direction for sample of shapes

5.3.2 Artificial neural network (ANN) properties

The ANN model is trained with 475 samples forming different building shapes. The aerodynamic database is formed from different combinations of the design variables (i.e. r1, r2 and θ), wind angle of attack (AOA) and the corresponding objective function values obtained from the LES analyses. 70% of the samples are used to train the ANN, while 30% are used to validate and test the ANN model. The ANN estimates the objective functions with sufficient accuracy, as shown in Figure 5-6. Figure 5-6a shows the regression plot of the ANN model indicating a regression coefficient of 0.967, while Figure 5-6b the error distribution, where error does not exceed 7% in 92% of the samples. This endorses the reliability of the ANN for mapping highly irregular relation that exist in the present function provided that a large number of training samples covering wide search domain (through a random approach of selecting these samples) is used.

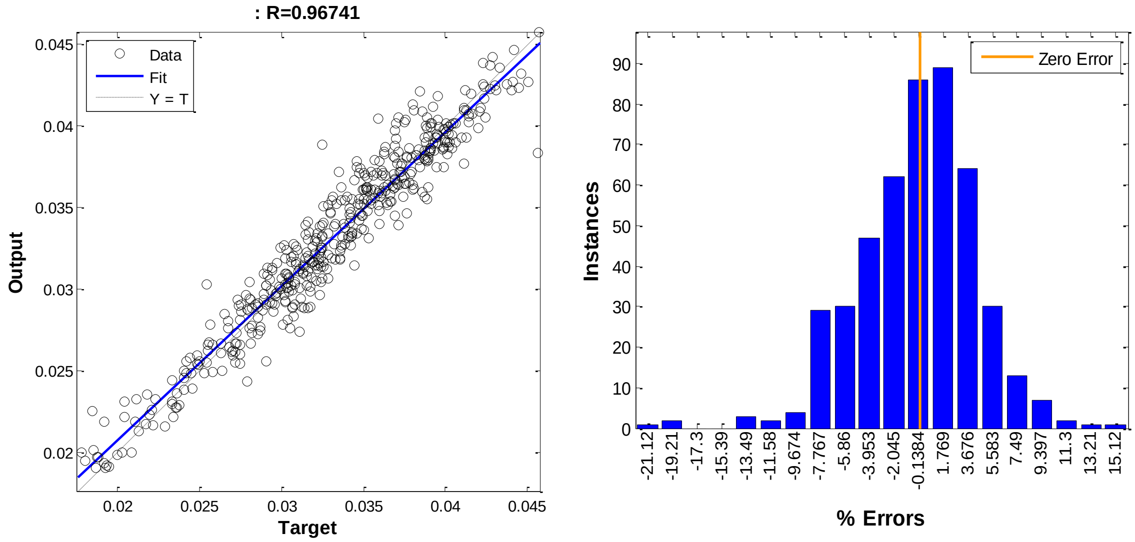

(a) (b)

Figure 5-6 a) Error distribution and b) Regression plot for the ANN

5.3.3 Genetic algorithm (GA) properties

As mentioned earlier, a real coded genetic algorithm is adopted for optimization where the design variables are coded as real numbers. The optimization procedure starts by randomly selecting 40 candidates to form the initial population. Different types of crossover and mutation operators are applied to this population to produce new generations. The GA technique requires precise selection of crossover and mutation operators. Crossover operators combine high fitness parents to produce better offsprings in order to improve the solution over generations. Three types of crossover operators are utilized, which are arithmetic, uniform and heuristic. In contrast, mutation operators alter the design variables of low fitness candidates to produce offsprings that search unexplored areas of the search space to avoid trapping in a local minimum. Three types of mutation operators are used, which are uniform, non-uniform and boundary. Details of the operators can be found in Michalewicz and Fogel (2011). The required number of generations is found to be 50 where no improvement is obtained by increasing the number of generations.

5.4 Optimization results

After running the optimization analysis, best fitness curve is obtained, which shows the aerodynamic improvement gained over optimization generations, as shown in Figure 5-7. The optimal solution is obtained when no significant improvement is found between successive generations. The optimization procedure is repeated four times to confirm convergence to the same optimal solution thus avoiding being trapped in a local minimum. The figure shows the shape and design variables for the resulted optimal solution. It is found that the optimal solution reduced the along-wind base moment by more than 45% compared to unmitigated square building shape.

A comparison is conducted between the optimal building shape and the basic square building to elaborate the aerodynamic improvement achieved from the AOP. As shown in Figure 5-8a, the wake zone developed in the optimal shape is significantly smaller than the one from the rectangular building, which indicates the lowering in the along-wind moments. Moreover, the magnitudes of the pressure coefficient on the optimal solution is lower than that of the basic building shape. This also shows the effect of the attained aerodynamic improvement throughout the AOP. Finally, in Figure 5-8b, the time history for the along-wind base moment for the optimal solution shows lower values than that of the rectangular building.

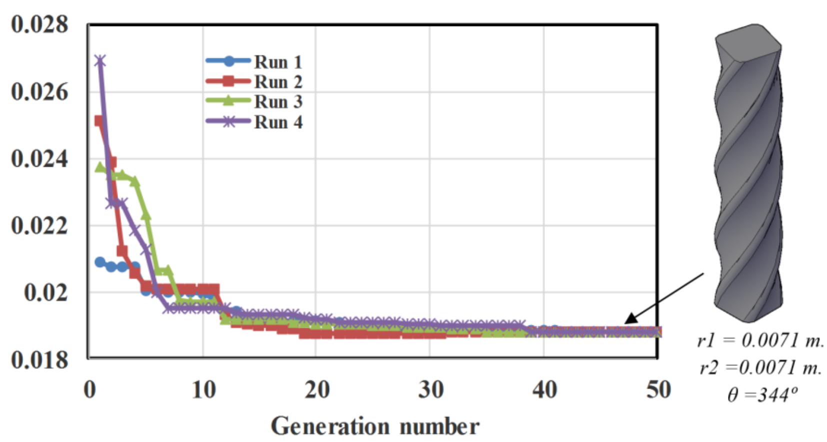

Figure 5-7 Fitness curves for the optimization example

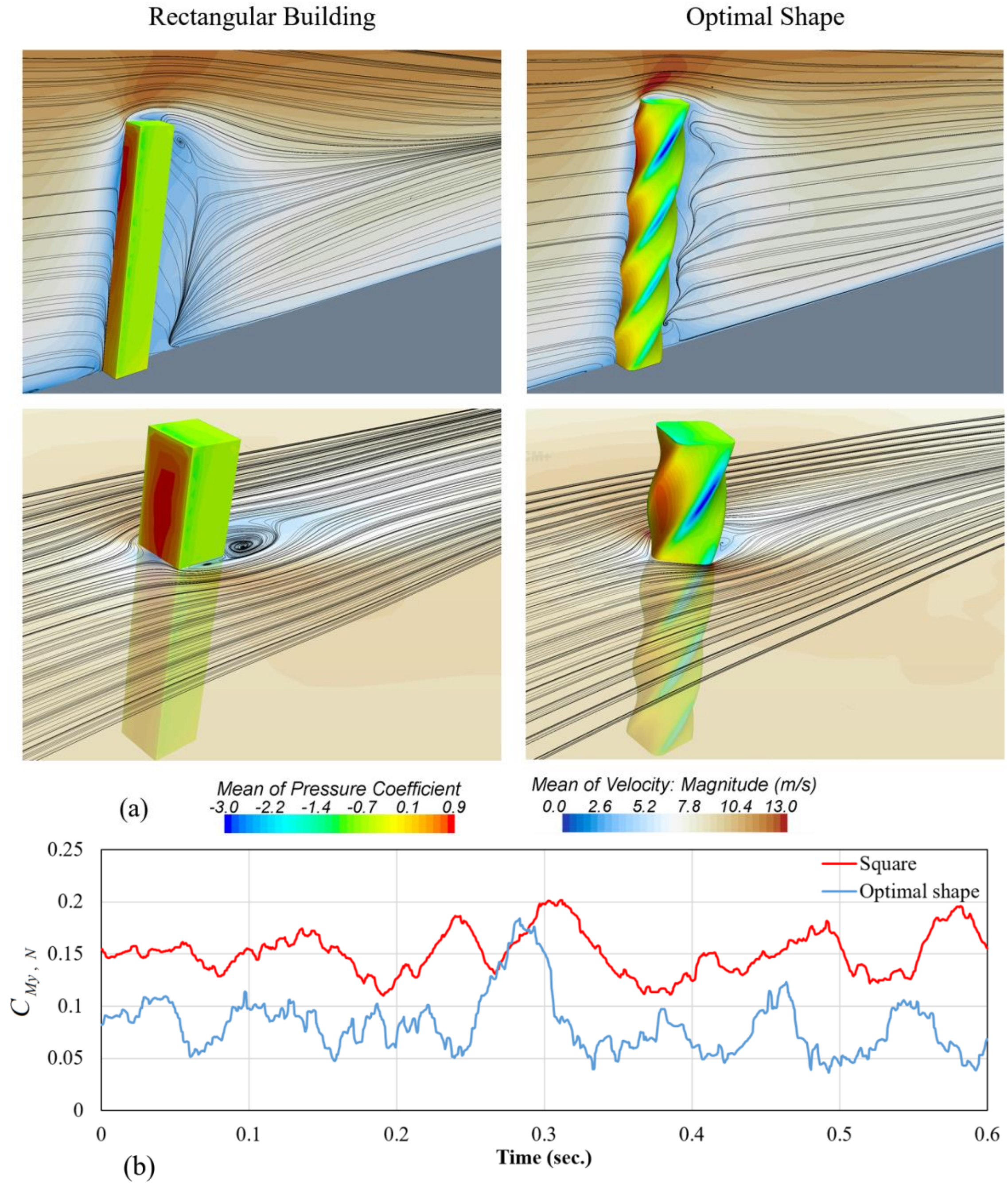

Figure 5-8 (a) Mean velocity and pressure coefficient contour (b) Normalized moment coefficient in the along-wind direction for the square and optimal cross-sections

5.5 Conclusion

In the current study, an aerodynamic optimization procedure is developed for reducing wind loads and motions. The procedure integrates genetic algorithm, Computational Fluid Dynamics (CFD) and Artificial Neural Network (ANN) in an automated procedure for estimating the optimal building shape. An illustration problem is presented reduction of the along-wind base moment by introducing corner mitigations and helical twisting of a tall building. The objective function is reduced by more than 45% compared to square cross-section. It was found that using ANN in the optimization procedure eliminates the need for sequential iterative computationally demanding CFD analyses, which will consequently reduce the required computational time.

5.6 References

Bernardini, E., Spence, S., Wei, D., Kareem, A., 2015. Aerodynamic shape optimization of civil structures: A CFD-enabled Kriging-based approach. Journal of Wind Engineering and Industrial Aerodynamics 144, 154-164.

Carassale L., Freda A., Marrè-Brunenghi M., 2014. Experimental investigation on the aerodynamic behavior of square cylinders with rounded corners. Journal of Fluids and Structures, 44, 195-204.

Dagnew A, Bitsuamlak G.T. Computational evaluation of wind loads on buildings: a review, Wind and Structures 2013; 16(6), 629-660.

Elshaer, A., Bitsuamlak, G.T., El Damatty, A., 2014. Wind Load Reductions due to Building Corner Modifications. 22nd Annual Conference of the CFD Society of Canada. Toronto, Canada.

Elshaer, A., Bitsuamlak, G.T., El Damatty, A., 2015a. Aerodynamic shape optimization for corners of tall buildings using CFD. 14th International Conference on Wind Engineering. Porto Alegre, Brazil.

Elshaer, A., Bitsuamlak, G.T., El Damatty, A., 2015b. Vibration control of tall buildings using aerodynamic optimization. 25th Canadian Congress of Applied Mechanics, London, Canada.

Franke J. Recommendations of the COST action C14 on the use of CFD in predicting pedestrian wind environment. The forth international Symposium on Computational Wind engineering 2006; Yokohama, Japan. 529-523.

Germano, M., Piomelli, U., Moin, P., Cabot, W. A dynamic subgrid-scale eddy viscosity model. Physics of Fluids 1991; 3(7), 1760-1765.

Kareem, A., Spence, J., Bernardini, E., Bobby, S., Wei, D., 2013. Using computational fluid dynamics to optimize tall building design. CTBUHJ. (III), 38-42.

Kawai, H., 1998. Effects of corner modifications on aeroelastic instabilities of tall buildings. Journal of Wind Engineering and Industrial Aerodynamics 74-76, 719-29.

Kwok, S., 1988. Effects of building shape on wind-induced response of tall buildings. Journal of Wind Engineering and Industrial Aerodynamics 28, 381-90.

SHARCNET is a consortium of colleges, universities and research institutes operating a network of high-performance computer clusters across south western, central and northern Ontario," 2016. [Online]. Available: www.sharcnet.ca.

Smagorinsky J., General circulation experiments with the primitive equations, I. the basic experiment. Monthly Weather Review 1963; 91, 99-164.

STAR CCM+, v.10.06, CD-ADAPCO Product, www.cd-adapco.com/products, 2016.

Tamura T., Miyagi T., Kitagishi T., 1998. Numerical prediction of unsteady pressures on a square cylinder with various corner shapes. Journal of Wind Engineering and Industrial Aerodynamics.74-76, 531-542.

Tamura, T., Miyagi, T., 1999. The effect of turbulence on aerodynamic forces on a square cylinder with various corner shapes. Journal of Wind Engineering and Industrial Aerodynamics 83, 135-145.

Tanaka H., Tamura Y., Ohtake K., Nakai M., Chul Kim Y., 2012. Experimental investigation of aerodynamic forces and wind pressures acting on tall buildings with various unconventional configurations. Journal of Wind Engineering and Industrial Aerodynamics vol. 107-108, 179-191.

Tominaga Y, Mochida A, Yoshiec R, Kataokad H, Nozu T, Yoshikawa M, Shirasawa T. AIJ guidelines for practical applications of CFD to pedestrian wind environment around buildings. Journal of Wind Engineering and Industrial Aerodynamics 2008; 96(10-11), 1749-1761.

Chapter 6

6 Multi-objective optimization of tall building vents for wind-induced loads reduction

6.1 Introduction

Over the past century, the majority of populations have moved to live in urban regions rather than rural ones. For instance, urban regions used to be home to 37% of the total population in Canada, while now they are home to more than 81% [1]. This fact is exponentially increasing the value of land in major cities, which encourages the construction of taller and slenderer tall buildings. Buildings of high aspect ratios (height to width ratios) are usually more vulnerable to lateral loads such as wind because they govern the design of most lateral load resisting systems (shear walls, frames, etc.). Moreover, due to wind, tall buildings may vibrate and cause serious “uncomfortable” or even “fearful” experience for people [2]. Controlling the wind-induced loads and vibrations can be achieved through three approaches that include: (1) utilizing sufficient structural components and external damping systems, (2) introducing aerodynamic mitigations for the building outer shape, or (3) combining the previous two approaches by improving both structural components and aerodynamic performances of the building. The first approach aims to sacrifice additional resources (e.g. higher strength for structural elements and damping systems) to avoid changing the building outer shape. The second approach saves these expenses by reducing the applied wind load through aerodynamic mitigation. It should be noted that, in many cases, meeting the strength and serviceability requirements cannot be satisfied unless both structural and aerodynamic improvements are used (third approach). This is why almost all recently-built super tall buildings introduce aerodynamic mitigations to their outer shape design either locally (at the corner shapes) or globally (along the height of the building) [3] to the design of the outer shape.

“Local Shape Mitigation” of tall buildings focuses on changing the corner shapes to enhance the aerodynamic performance. The main advantage of this type of mitigation is that they have limited effect on the architectural and structural concept of the structure. Various corner shapes have been investigated in previous literature including rounded corners (Tamura and Miyagi [4]; Carassale et al. [5]), chamfered corners (Tamura et al. [6]; Gu and Quan [7]), recessed corners (Kawai [8]; Tse et al. [9]), and finned corners (Kwok and Bailey [10]; Kwok et al. [11]). Detailed literature for the local mitigation is provided in Elshaer et al. [3]. In contrast, “Global Shape Mitigation” has a considerable effect on the architectural and structural design because the mitigations extend to be along the whole height and width of the building rather than being localized at the corners. This scale of mitigation can provide better enhancement to the aerodynamic performance than the local mitigations due to the wider variety of changes that can be applied. For instance, Davenport [12] reported that tapering tall buildings along their height can spread the vortex-shedding over a broader range of frequencies, thus reducing the across-wind responses. Helical twisting of tall buildings is considered an efficient approach to reduce across-wind forces because the resultant of the wind force will vary in direction along the height of the building that will also decrease the across-wind responses (Tanaka et al. [13]; Xie [14]). Another effective way to disturb the intensity of the vortex shedding is providing one or more vents, which will be the focus of the current work. This mitigation allows the air flow to pass through openings, which weaken the development of vortex shedding, which will reduce the across-wind forces and responses (Tanaka et al. [13]; Miyashita et al. [15]; Dutton and Isyumou [16]). In addition, having openings in the building façade will reduce drag forces due to the reduction in the building projected area. Figure 6-1 shows different types of global mitigation that were previously investigated. It can be noticed that the majority of previous studies compare different types of mitigations based on a single set of dimensions for each mitigations family. However, each family (of a specific shape mitigation) can produce a wide range of aerodynamic performances based on the selection of a different combinations of mitigation dimensions. Consequently, a wider search space (i.e. more building shape alternatives) can be explored by integrating an optimization algorithm to the aerodynamic assessment procedure (Kareem [17]).

The iterative procedure of optimization requires multiple evaluations for the aerodynamic performance, which requires an affordable numerical model, such as computational fluid dynamics (CFD), to avoid the costly wind tunnel experiments (Bernardini et al. [18]; Elshaer et al. [19]). A high order CFD model is essential to properly simulate the atmospheric boundary layer (ABL) turbulence and its interaction with structures. These complex interactions can be accurately captured through large eddy simulation (LES) models as reported by Nozawa and Tamura [20], Huang and Li [21], Aboshosha et al. [22], Huang et al. [23], and Elshaer et al. [24]. LES can be directly used in the optimization procedure for evaluating the aerodynamic performance of different shapes, which will require a high-level computational capacity. Alternatively, a surrogate analytical model can be utilized to estimate the aerodynamic behaviour after being trained using a database of different shapes and their corresponding aerodynamic behaviour (Elshaer et al. [3]; Kareem et al. [17]; Bernardini et al. [18]). The current study adopts a recently developed aerodynamic optimization procedure (AOP), which couples the genetic algorithm with the artificial neural network (ANN) model trained by a database resulted from CFD analysis in an automated process. The AOP considers the wind directionality effect by examining all values of wind angle of attack (AOA) for each building shape. The latter procedure was previously employed to conduct single-objective optimization for building corners using three-dimensional large eddy simulations (3D-LES) of a 2D flow [3,19,25]. Since the current optimization problem examines building openings, which is a global mitigation, this requires a 3D-LES of an atmospheric boundary layer (ABL) flow to capture the aerodynamic improvement due to that type of mitigation [26].

Building on these benchmarks, the current study conducts a multi-objective optimization (i.e. minimizing base moments in both of the two orthogonal directions) for a tall building with three through openings. The AOP is adopted to identify the Pareto Front (PF), which is the set of optimal shapes that achieves the best fitness (improving the aerodynamic performance) among the whole search space. The main advantage of defining the PF is having the flexibility of choosing from a set of optimal building shapes rather than obtaining only one optimal shape in the single-objective optimization. This paper is divided into five sections, in section 1 (this section), presents an introduction and literature review on building aerodynamic mitigations and optimization procedures. For the sake of completeness, section 2 briefly summarizes the main steps required for conducting the AOP. Section 3 describes the case study and the different optimization problems presented in the current work. In Section 4, the optimization results and discussions for two single-objective optimization problems are provided and a validation is made for the basic model with previous boundary layer wind tunnel (BLWT) tests and other numerical studies from literature. While Section 5 shows the results and discussions for a multi-objective optimization problem.

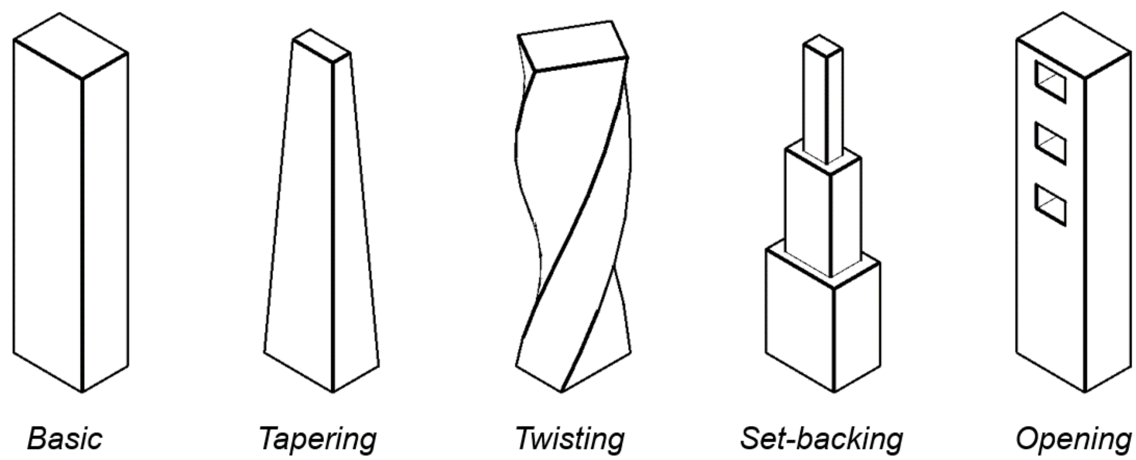

Figure 6-1 Examples of global mitigations of tall building

6.2 Aerodynamic Optimization Procedure (AOP)

The framework of the AOP starts by defining (i) the objective function, which is the aerodynamic property targeted to be minimized or maximized; and (ii) design variables, which are the geometric parameters controlling the shape of the aerodynamic mitigation. In case of multi-objective optimization problems, more than one objective function needs to be defined. Upper and lower bounds are usually defined for the design variables to ensure that the resulting optimal shape(s) fits in the architectural and structural concept of the building. Then, random combinations of the design variables and wind AOA are generated (i.e. training samples). The corresponding objective function(s) are evaluated for each training sample to form a training database for the ANN model. The training ANN process will continue by increasing the number of training samples until satisfactory accuracy for estimating the objective function(s) is achieved [3]. Adoption of ANN in objective function(s) evaluation attained many advantages for the AOP, including (i) significantly lowering the computational cost, (ii) eliminating the need for the direct integration of the CFD within the optimization process (i.e. CFD can be used offline to train the surrogate model), (iii) allowing the use of any available BLWT database in conjunction with the CFD database; and (iv) mapping a highly nonlinear relationship between the design variables and the objective function(s) if trained properly (Bitsuamlak et al. [27]).

After that, the optimization algorithm (e.g. genetic algorithm) is utilized to find the optimal building shape(s) that optimize the objective function(s). The optimization process requires multiple evaluations of the objective function(s) that are conducted using the computationally affordable ANN model. Finally, the optimal building shape(s) are obtained when no further improvement in the objective function(s) is achieved by increasing the number of optimization iterations (i.e. generations). The proposed procedure was previously examined by the authors for local corner modifications (Elshaer et al. [3]) and for helical twisting modifications (Elshaer et al. [26]). Figure 6-2 summarizes the framework of the proposed AOP.

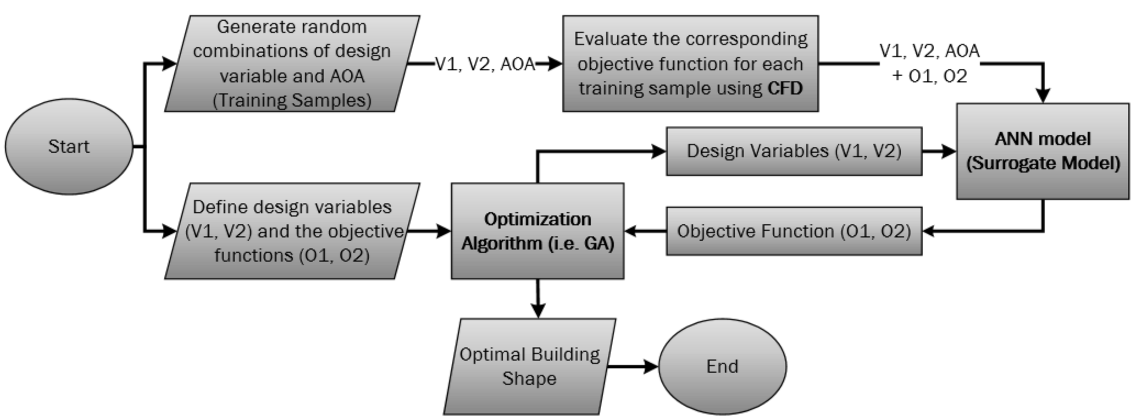

Figure 6-2 flowchart of the aerodynamic optimization procedure (AOP)

6.3 Demonstration Optimization problems

In the current study, the efficiency of the AOP is examined in the current work through three optimization problems. *Problem (1)* and *problem (2)* are single-objective problems aims to reduce the building peak base moment coefficients (C_{Mx} and C_{My}), respectively. While *problem (3)* is a multi-objective problem, where both base moments are reduced simultaneously. The objective functions are set to be the two principal base moment coefficients, which are computed using Equation 6-1. The wind directionality is taken into consideration by defining the value for the objective functions as the ones corresponding to the most critical wind AOA. The basic building geometry is chosen to be that of the Commonwealth Advisory Aeronautical Council (CAARC) standard building, which was widely studied in many numerical and experimental researches [24,28–30]. As mentioned earlier, the mitigation type in the current study is introducing three vents to the tall building, where the design variables are the aspect ratio of the openings (i.e. $v_1 = a/b$) and the spacing between each two successive vents ($v_2 = d/H * 100$). The definition of the geometric parameters and the base moment directions are summarized in Figure 6-3. So as to keep the generated shapes within the accepted architectural limits, v_1 and v_2 are bounded by *0.25* and *3%* as lower bounds; and *4.0%* and *13%* as upper bounds, respectively. In addition, the total volume of the three openings is maintained to be equal to *10%* of the building volume. After generating random combinations of the design variables (v_1 and v_2), the corresponding objective functions (C_{Mx} and C_{My}) will be evaluated using CFD analyses, which is described in subsection 6.3.1. The database formed of the randomly selected design variables (v_1, v_2) and different AOA with the corresponding computed objective functions will be utilized to train the ANN model, as described in subsection 6.3.2. when the ANN model reaches a reliable accuracy for estimating the design variables, the optimization algorithm will then use the trained ANN model to obtain the optimal building shape(s). Subsection 6.3.36.3.3 describes the details of the genetic algorithm adopted in the current study.

$$\widehat{C}_{Mx} = \overline{C}_{Mx} + g_f * C'_{Mx}$$
$$\widehat{C}_{Mx} = \overline{C}_{Mx} + g_f * C'_{Mx}$$
$$C_{Mx} = \frac{M_x}{\frac{1}{2}\rho v_{ref}^2 DH^2}$$
$$C_{My} = \frac{M_y}{\frac{1}{2}\rho v_{ref}^2 BH^2}$$

Equation 6-1

where C_{Mx} and C_{Mx} are the peak base moment coefficients about x and y directions, respectively; $\overline{C}_{Mx}$ and $\overline{C}_{My}$ are the mean base moment coefficients about x and y directions, respectively; C'_{Mx} and C'_{My} are the fluctuating base moment coefficients about x and y directions, respectively; g_f is a peak factor that is taken equal to 3.5; M_x and M_y are the moment about x and y axes, respectively, ρ is the air density, v_{ref} is the reference velocity at the building height, D is the building width, B is the building depth; and H is the building height

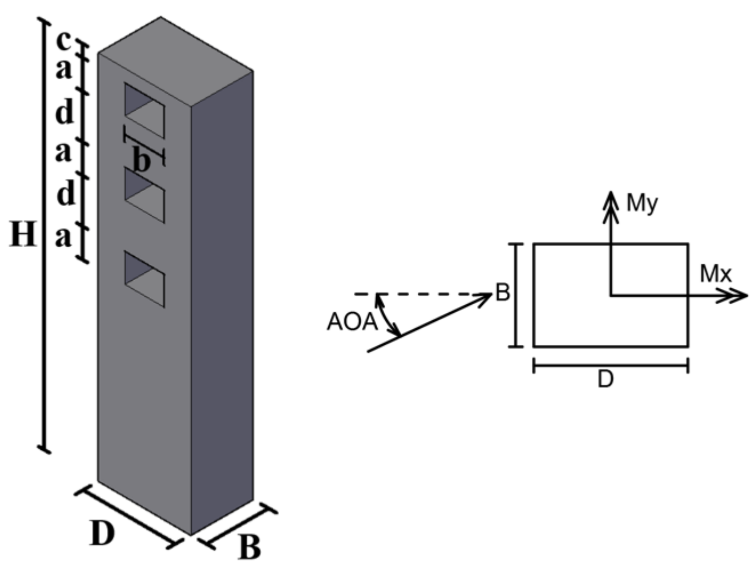

Figure 6-3 Geometric parameters and base moment directions of the study building

6.3.1 LES properties of an ABL flow

In the current study, three-dimensional large eddy simulations (3D-LES) are utilized to evaluate the objective functions for 200 training models with length and time scales of 1:400 and 1:100, respectively. Computational domain dimensions and mesh discretization are chosen based on the recommendation of Franke et al. [31]; and Dagnew and Bitsuamlak [32]. The sides and the top of the computational domain are assigned as symmetry plane boundary conditions, while the bottom of the computational domain and all building faces are defined as no-slip walls. Figure 6-4summarizes the boundary conditions and computational domain dimensions used in the CFD analysis. The inflow boundary condition generates a wind flow field assuming an open terrain exposure, which follows the ESDU [33]. Figure 6-5 shows the adopted mean velocity, the turbulence intensity and the turbulence length scale profiles. The computational domain is discretized to polyhedral control volumes, where the sizes of the meshes are divided into two zones based on the flow structures required to be captured. As shown in Figure 6-6, the flow turbulence in highly complex (i.e. high vorticity values) near the study building, thus finer mesh is used at the locations of high velocity gradients. *Zone 1* is located away from the building of interest where the grid size is maximum (i.e. *H/30*). *Zone 2* is located close to the building of interest where finer grid size is utilized to capture important flow details of in the wake zone and the zone around the study building (i.e. *H/70*). Fifteen prism layers (i.e. surface following grids) that are parallel to the study building surfaces with stretching factor of 1.05 are utilized satisfying the recommendations by Franke et al. [31] Murakami [34] and Tominaga et al. [35]. Figure 6-7 shows the utilized grid in the current study. The simulations are conducted using a commercial CFD package (STAR-CCM+ v.10.06 [36]) employing LES with dynamic sub-grid scale model by Smagornisky [37] and Germano et al. [38]. Each simulation is resolved for 1,500 time steps representing 0.75 seconds in model-scale (i.e. 1.25 minutes in full-scale). The computational time required for each simulation is 4 hours on 8 processors. SharcNet high performance computer (HPC) facility at the Western University is utilized for conducting the numerical simulations. After running the LES analyses, the time history of the base moment coefficients (C_{Mx} and C_{My}

) are extracted, as shown in Figure 6-8. Figure 6-9 shows the peak base moment coefficients (C_{Mx} and C_{Mx}) for all the training models.

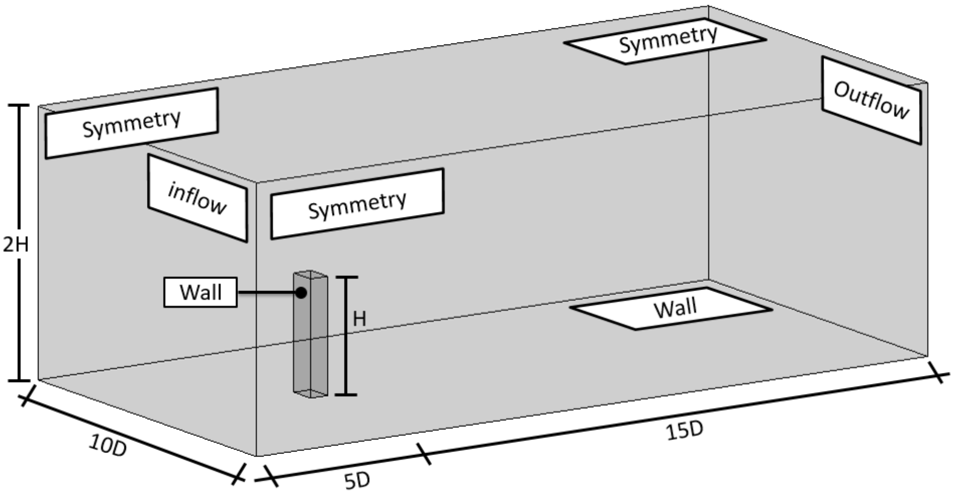

Figure 6-4 Computational domain dimensions and boundary conditions

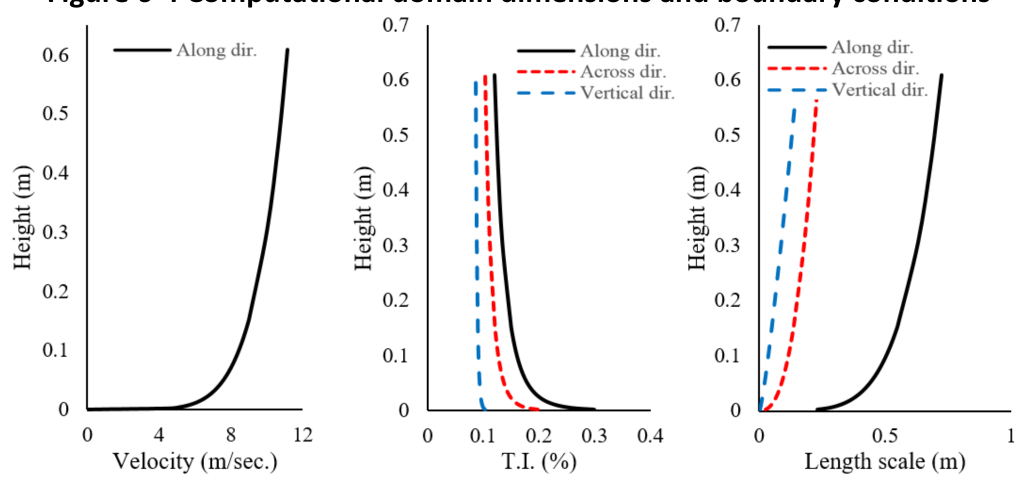

Figure 6-5 (a) mean velocity, (b) turbulence intensity and (c) turbulence length scale profiles used for inflow boundary condition

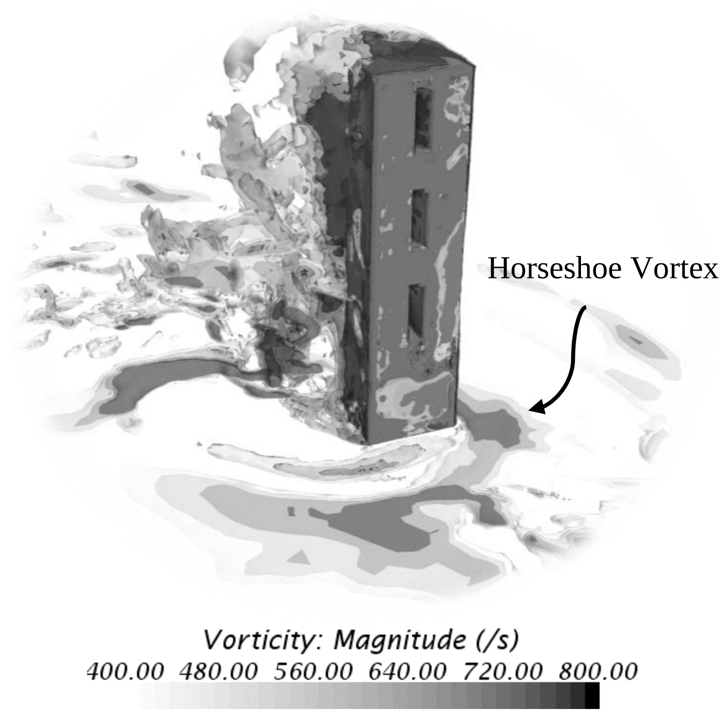

Figure 6-6 Vorticity visualization for a training model

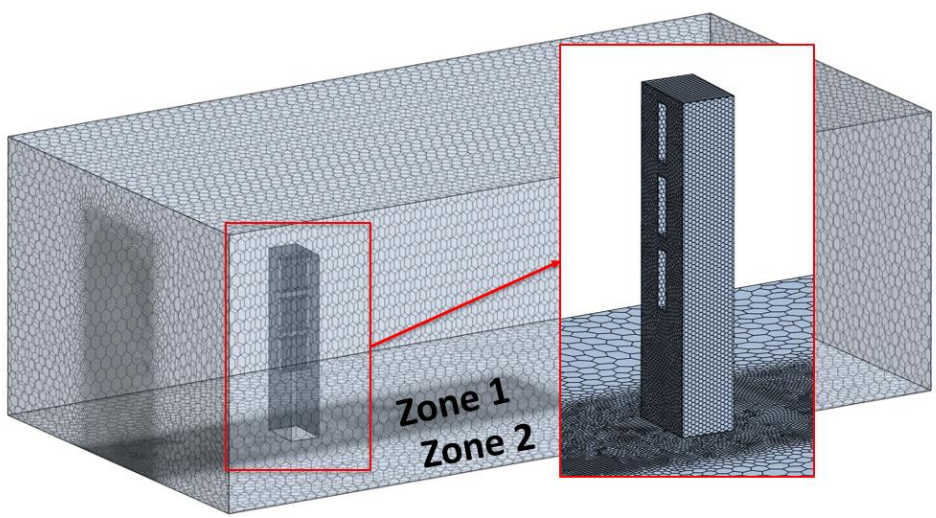

Figure 6-7 Grid resolution utilized for the ABL flow simulations

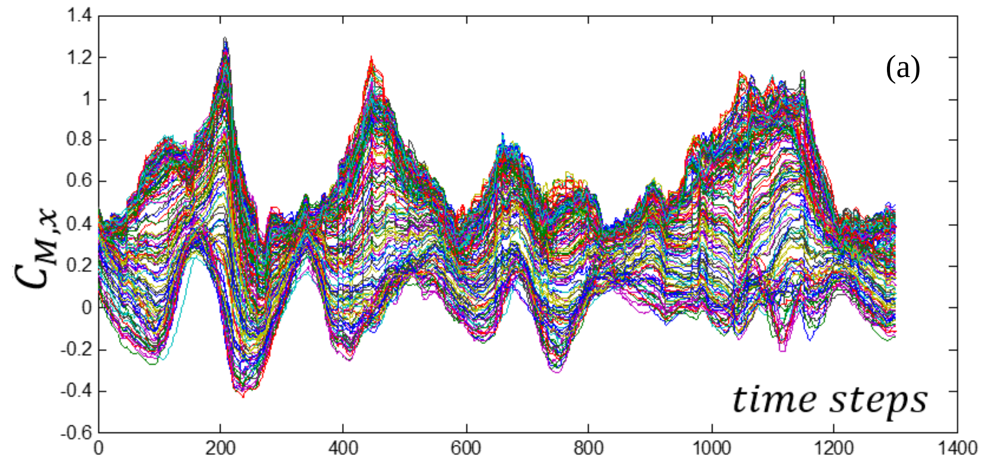

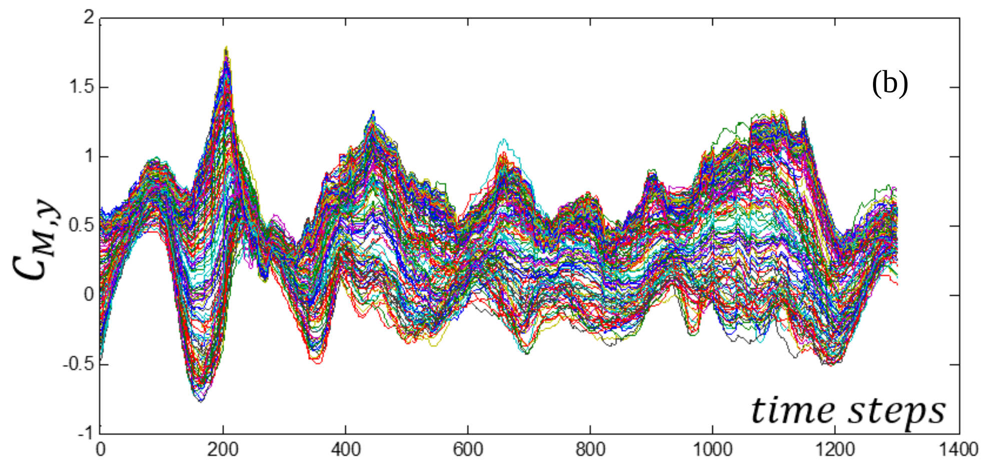

Figure 6-8 Time histories of moment coefficient about (a) x- and (b) y-axis for different geometric samples

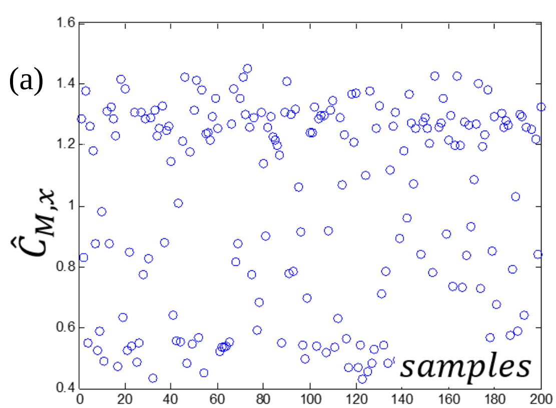

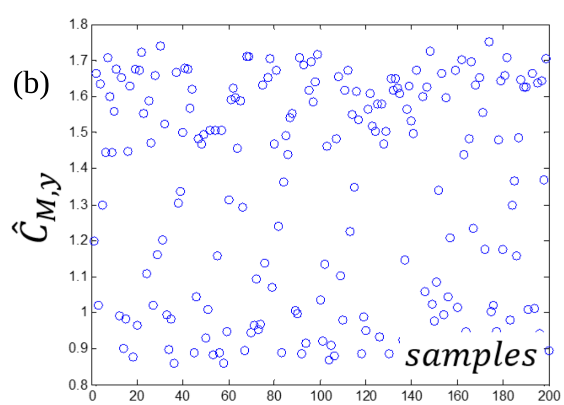

Figure 6-9 Peak moment coefficient about (a) x- and (b) y-axis for different geometric samples

6.3.2 ANN model properties

ANN model is selected as a surrogate model for objective functions estimation over other analytical models due to its proven high accuracy in mapping similar complex functions [3,27]. In order to accurately capture the variability of the objective functions with the design variables and AOA, the training samples are selected randomly (combinations of v_1, v_2 and AOA), as shown in Figure 6-10. ANN model is trained using the 200 training samples and their corresponding objective functions, with 70% of the samples being used for training, while 30% are used to validate and test the ANN model. Figure 6-11 shows the regression plots of the ANN model indicating a correlation coefficient of 0.998 and 0.993 for the $C_{M,x}$ and $C_{M,y}$, respectively. The error in estimating the objective function is less than 4% in 91% of the training and testing samples, as shown in Figure 6-12. This endorses the reliability of the ANN for mapping highly irregular relation that exist in the present function provided that a large number of training samples covering wide search domain (through a random approach of selecting these samples) is used.

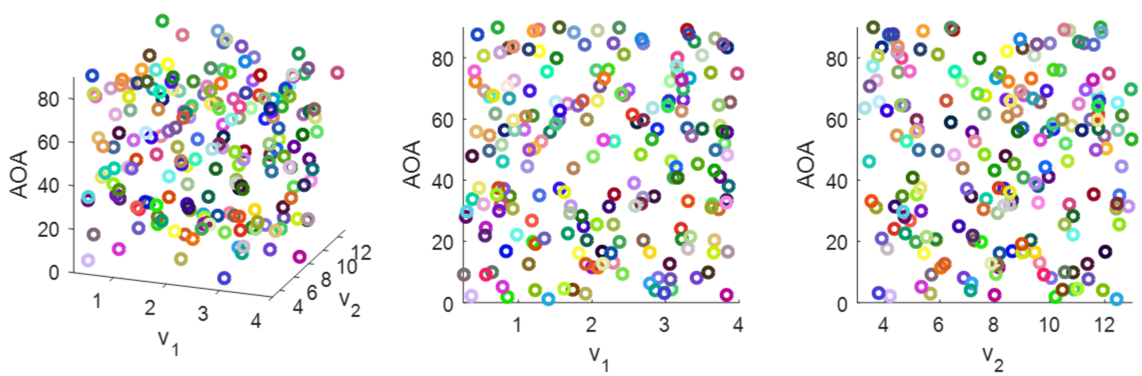

Figure 6-10 Randomly selected training samples for Artificial Neural Network model

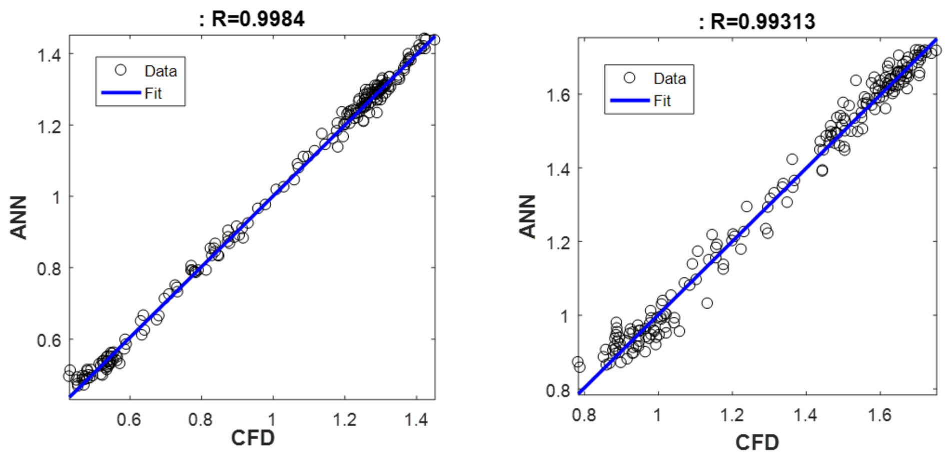

Figure 6-11 Regression plot for the ANN model estimating (a) $C_{M,x}$ and (b) $C_{M,y}$

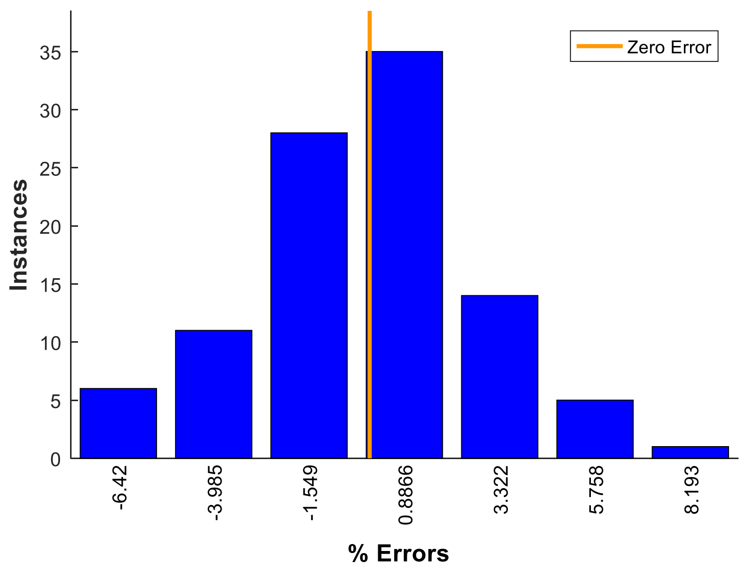

Figure 6-12 Error distribution of the ANN model

6.3.3 GA details

The genetic algorithm (GA) is adopted in the current study as the optimization technique, where design variables are coded as real numbers. The GA is reported to be efficient in estimating the optimal solutions in similar complex engineering optimization problems by Zhou and Haghighat [39] and El Ansary et al. [40]. A more detailed discussion on GA can be found in Goldberg [41] and Davis [42]. The optimization process starts by forming the initial population candidates, which are 40 different combinations of the design variables.

The corresponding objective functions are evaluated for each candidate to enable the ranking of candidates based on their fitness (i.e. the candidates of lower objective function values are considered of higher fitness). Then, the crossover and mutation operators are applied to the current candidates to produce new offsprings forming the next “Generation”. Crossover operators combine high fitness parents that target to produce higher fitness offsprings, while mutation operators are applied on low fitness candidates that investigate unexplored areas of the search space to avoid being trapped in a local minimum. Three types of crossover operators are utilized, which are arithmetic, uniform and heuristic, while other three types of mutation operators are used, which are uniform, non-uniform and boundary. Details of the operators can be found in Michalewicz and Fogel [43]. The process of applying the operators and producing new generations will continue until no significant improvements are obtained over the generations. The highest fitting candidate in the last generation will be considered the optimal solution. In the current study, 40 generations are produced until reaching the optimal building shape.

6.4 Single-objective optimization

The current section discusses *Problem (1)* and *problem (2)*, which optimize for only one objective function, either $C_{M,x}$ and $C_{M,y}$, respectively. This type of optimization (single-objective optimization) is preferred when a certain aerodynamic property is governing the design or hard to be fulfilled. In this case, the optimization problem aims to improve the performance of a tall building in order to reduce the aerodynamic effect of that critical objective function. The aerodynamic improvement can be then recognized from the optimization fitness curve, which shows the objective function values of the best fitness candidate in each generation versus the number of optimization cycles (generations). The optimization process stops when no further improvement achieved from increasing the number of generations. It is usually recommended to repeat the optimization process for multiple times to ensure reaching the global optimal building shape rather than being trapped in a local extreme value. Figure 6-13a and b shows the fitness curves for the $C_{M,x}$

and $C_{M,y}$ problems, respectively. The optimization process is repeated four times for each problem to ensure the conversion towards the global optimal shape. For *Problem (1),* the optimal shape is found to be of $C_{M,x}$ equals to 1.235 which is 47% lower than that of the basic CAARC building without the venting mitigation. Whereas the optimal building shape in *Problem (2),* is found to be of $C_{M,y}$ equals to 1.516, which is lower than that of the basic CAARC building by 42%. **Error! Reference source not found.** shows the surface plot of t he objective functions for each of the optimization problems evaluated using the ANN model. As shown from the figure, the optimization algorithm is capable of locating the optimal shape for each of the two problems without being trapped in other local extreme values. The figure also shows the shape and the design variables corresponding to each of the two optimal shapes. A further study is conducted by comparing the basic CAARC building to the optimal shapes. shows the mean velocity contour of the wind flow and the mean pressure coefficient (C_p) for the optimal and basic shapes. It can be visually noticed that the basic shape appears to be aerodynamically bluffer than the optimized shapes. This can be recognized from the difference in wake sizes and the magnitudes of the C_p values between the basic and optimal shapes.

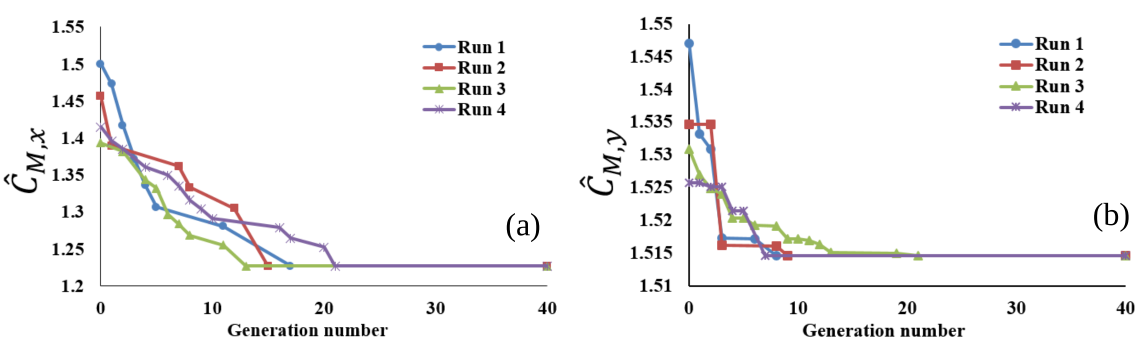

Figure 6-13 Fitness curves for the (a) $C_{M,x}$ and (b) $C_{M,y}$ optimization

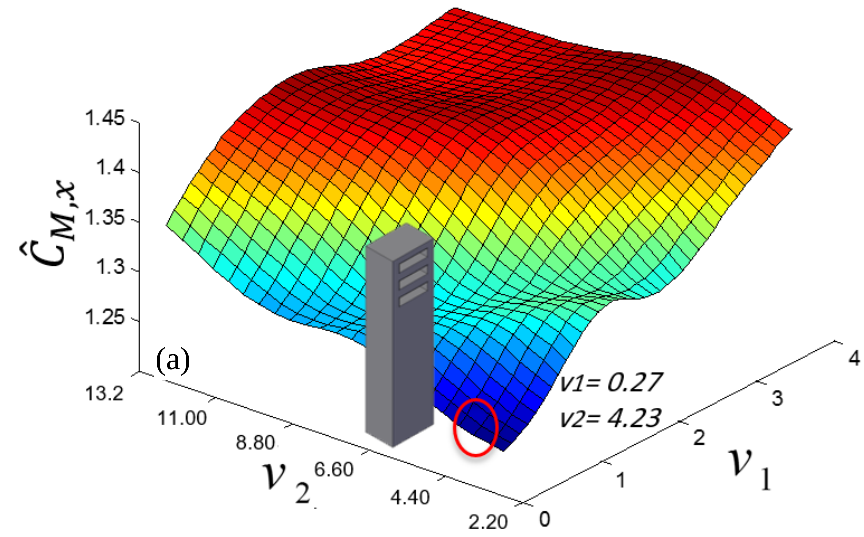

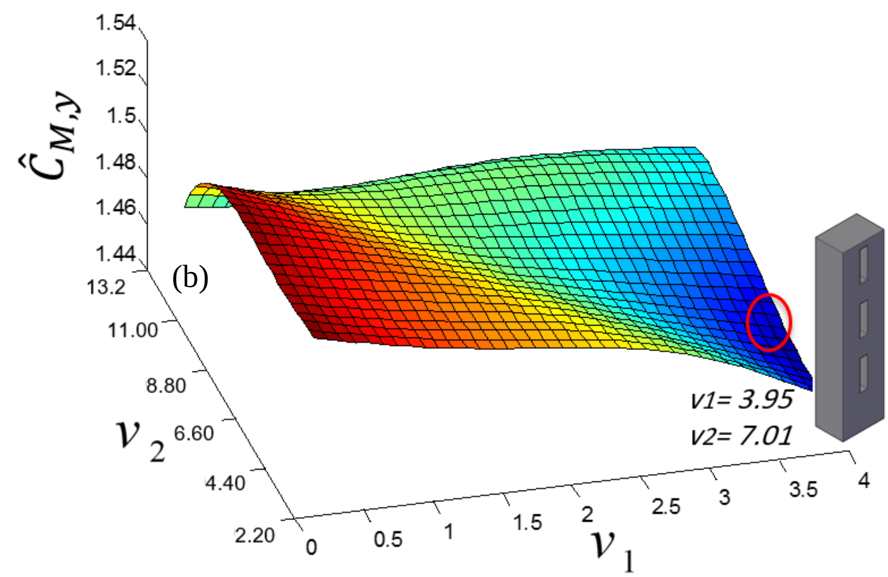

Figure 6-14 Surface plot for the ANN model of the peak moment coefficient about x-axis

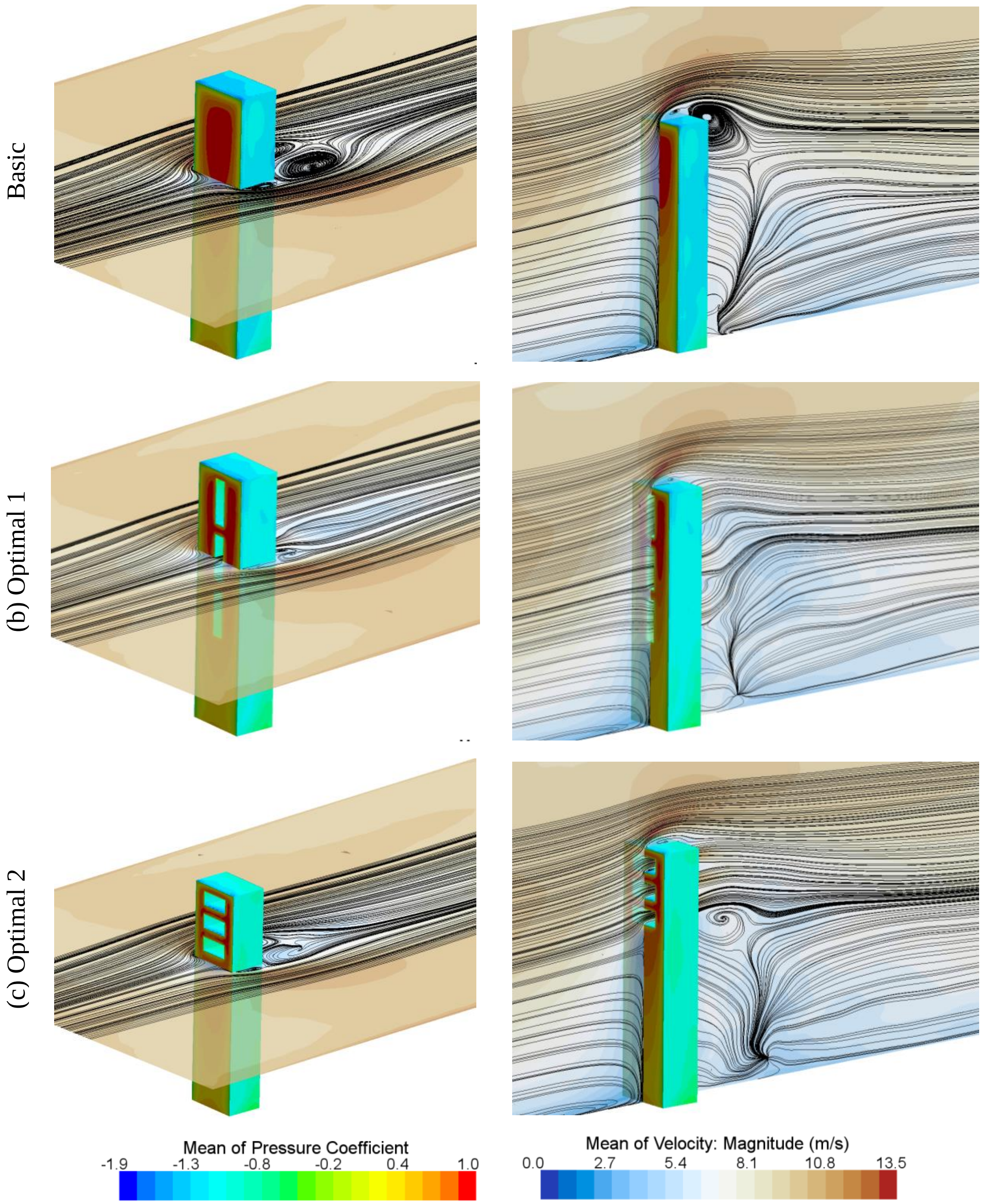

Figure 6-15 Mean wind field and Cp distribution for the (a) basic, (b) optimal 1; and (c) optimal 2 building shapes

6.5 Multi-objective optimization

This section investigates *Problem (3)*, which is a multi-objective optimization problem that aims to optimize both $C_{M,x}$ and $C_{M,y}$ simultaneously. Since no objective can be improved without sacrificing the other objective, this requires the definition of the Pareto front, which is the set of optimal solutions that shows the best trade-off between the objective functions. Thus, providing a set of optimal shapes provide a better chance for architects to involve adequacy and serviceability considerations in the selection of the outer shape of the building. After running the optimization process for 500 generations it is found that the spread of the solutions is almost constant for 200 generations. The Pareto front is chosen to be defined using 18 candidates, as shown in Figure 6-16. The figure also shows the shape and the design variables of four optimal shapes located on the Pareto front.

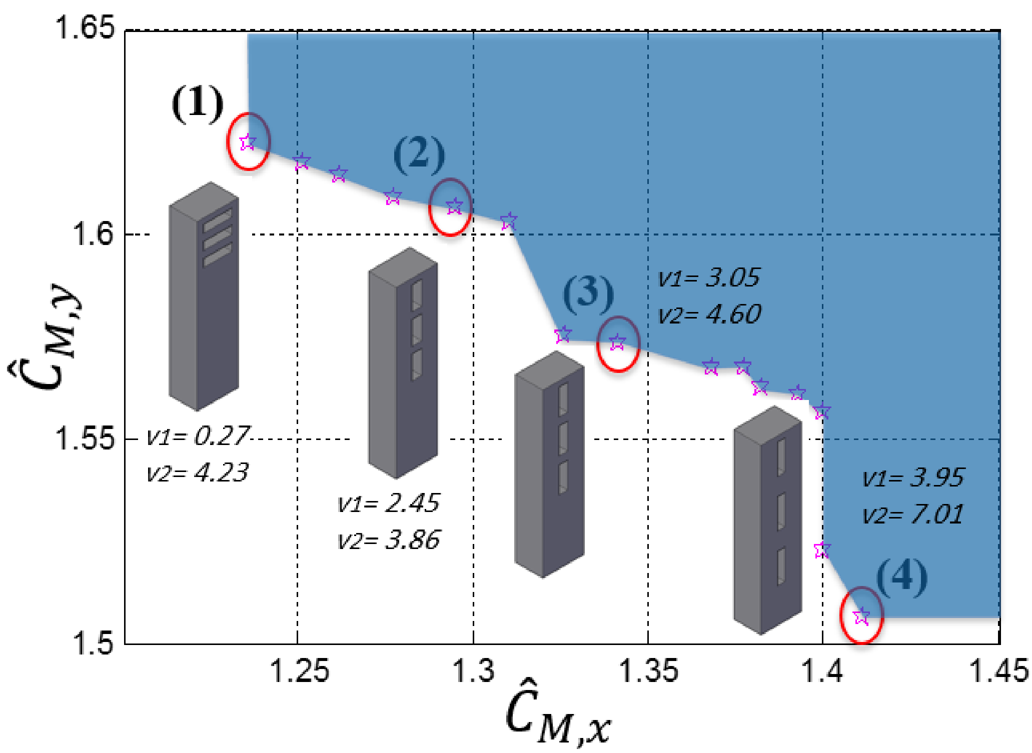

Figure 6-16 Pareto front optimal shapes and the corresponding objective function values

6.6 Conclusions

The current study investigates the effect of introducing three vents to a standard tall building called the Commonwealth Advisory Aeronautical Research Council (CAARC) building. An aerodynamic optimization procedure is adopted, which couples the Genetic Algorithm (GA), Large Eddy Simulation (LES) and Artificial Neural Network (ANN) models. The ANN model is utilized to estimate the objective function values (aerodynamic properties) after being trained using a database of different combinations of design variables (geometry parameters), wind angle of attack and the corresponding objective function values. Two single-objective optimization problems are conducted to reduce the peak base moment coefficients in addition to a multi-objective optimization problem to simultaneously reduce both peak base moment coefficients. The contributions of the current study can be summarized as follows:

- Introducing vents to a tall building is considered an effective approach in reducing base moments in both the orthogonal directions as a result of weakening the development of vortex shedding and reducing the projected area of the building.

- Three dimensional LES models of an atmospheric boundary layer flow are required to capture the aerodynamic improvement gained due to global mitigations such as building vents.

- Using ANN as a surrogate model is considered an effective analytical approach to capture complex variations in the objective function with an error less than 4% in 91% of the training samples, in addition to significant acceleration in the optimization procedure.

- Single-objective optimization problems resulted in 47% and 42% reduction in the peak base moment coefficient about the x and y axes, respectively.

- The continuous flow information provided by LES enabled visual comparison between the basic (unmitigated) building shape and the optimal ones.

- Conducting multi-objective aerodynamic optimization problem provides a set of optimal solitons (Pareto Front), which will allow architects to involve adequacy and serviceability considerations in the selection of the outer shape of the building.

- On the whole, the improvement in wind numerical simulations and aerodynamic optimization procedures enhanced with the advancements in computational power is expected to encourage urban designers and architects to pursue optimal climate responsive solutions and designs.

6.7 References

[1] Statistics Canada, 2011: Census of Population. n.d. http://www.statcan.gc.ca/tables-tableaux/sum-som/l01/cst01/demo62a-eng.htm (accessed February 4, 2011).

[2] Kwok KCS, Burton MD, Abdelrazaq AK. Wind-Induced Motion of Tall Buildings. Int J High-Rise Build 2015;4:1–8.

[3] Elshaer A, Bitsuamlak G, El Damatty A. Enhancing wind performance of tall buildings using corner aerodynamic optimization. Eng Struct 2016.

[4] Tamura T, Miyagi T. The effect of turbulence on aerodynamic forces on a square cylinder with various corner shapes 1999;83:135–45.

[5] Carassale L, Freda A, Marrè-brunenghi M. Experimental investigation on the aerodynamic behavior of square cylinders with rounded corners. J Fluids Struct 2014;44:195–204.

[6] Tamura T, Miyagi T, Kitagishi T. Numerical prediction of unsteady pressures on a square cylinder with various corner shapes 1998;76:531–42.

[7] Gu MÃ, Quan Y. Across-wind loads of typical tall buildings 2004;92:1147–65.

[8] Kawai H. Effect of corner modifications on aeroelastic instabilities of tall buildings. J Wind Eng Ind Aerodyn 1998;74–76:719–29.

[9] Tse KT, Hitchcock PA, Kwok KCS, Thepmongkorn S, Chan CM. Economic perspectives of aerodynamic treatments of square tall buildings. J Wind Eng Ind Aerodyn 2009;97:455–67.

[10] Kwok BKCS, Bailey PA. Aerodynamic devices for tall buildings and structures 2006;113:349–65.

[11] Kwok KCS, Wilhelm PA, Wilkie BG. Effect of edge configuration on wind-induced response of tall buildings. Eng Struct 1988;10:135–40.

[12] Davenport AG. The Response of Supertall Buildings to Wind. Second Century of the Skyscraper. Counc Tall Build Urban Habitat 1988.

[13] Tanaka H, Tamura Y, Ohtake K, Nakai M, Chul Y. Journal of Wind Engineering Experimental investigation of aerodynamic forces and wind pressures acting on tall buildings with various unconventional configurations. Jnl Wind Eng Ind Aerodyn 2012;107–108:179–91.

[14] Xie J. Aerodynamic optimization of super-tall buildings and its effectiveness assessment. J Wind Eng Ind Aerodyn 2014;130:88–98.

[15] Miyashita K, Katagiri J, Nakamura O, Ohkuma T, Tamura Y, Itoh M, et al. Wind-induced response of high-rise buildings Effects of corner cuts or openings in square buildings. J Wind Eng Ind Aerodyn 1993;50:319–28.

[16] Dutton R, Isyumov N. Reduction of tall building motion by aerodynamic treatments. J Wind Eng Ind Aerodyn 1990;36:739–47.

[17] Kareem A, Spence S, Bernardini E, Bobby S, Wei D. Using computational fluid dynamics to optimize tall building design. Counc Tall Build Urban Habitat 2013.

[18] Bernardini E, Spence SMJ, Wei D, Kareem A. Aerodynamic shape optimization of civil structures: A CFD-enabled Kriging-based approach. J Wind Eng Ind Aerodyn 2015;144:154–64.

[19] Elshaer A, Bitsuamlak G, El Damatty A. Aerodynamic shape optimization for corners of tall buildings using CFD. 14th Int. Conf. Wind Eng., 2015.

[20] Nozawa K, Tamura T. Large eddy simulation of the flow around a low-rise building immersed in a rough-wall turbulent boundary layer. J Wind Eng Ind Aerodyn 2002;90:1151–62.

[21] Huang SH, Li QS, Wu JR. Large eddy simulation of wind effects on a super-tall building. J Wind Eng Ind Aerodyn 2010;98:557–80.

[22] Aboshosha H, Elshaer A, Bitsuamlak GT, El Damatty A. Consistent inflow turbulence generator for LES evaluation of wind-induced responses for tall buildings. J Wind Eng Ind Aerodyn 2015;142:198–216. doi:10.1016/j.jweia.2015.04.004.

[23] Huang SH, Li QS, Wu JR. A general inflow turbulence generator for large eddy simulation. J Wind Eng Ind Aerodyn 2010;98:600–17.

[24] Elshaer A, Aboshosha H, Bitsuamlak G, El Damatty A, Dagnew A. LES evaluation of wind-induced responses for an isolated and a surrounded tall building. Eng Struct 2016;115:179–95. doi:10.1016/j.engstruct.2016.02.026.

[25] Elshaer A, Bitsuamlak G, El Damatty A. Vibration control of tall buildings using aerodynamic optimization. 25th Can. Congr. Appl. Mech., London, Ontario, Canada: 2015.

[26] Elshaer A, Bitsuamlak G, El Damatty A. Aerodynamic shape optimization of tall buildings using twisting and corner modifications. 8th Int. Colloq. Bluff Body Aerodyn. Appl. Boston, USA, 2016.

[27] Bitsuamlak G, Stathopoulos T, Bedard C. Effects of upstream two-dimensional hills on design wind loads: a computational approach. Wind Struct 2006;9:37–58.

[28] Wardlaw RL, Moss GF. A standard tall building model for the comparison of simulated natural winds in wind tunnels. Rep CC-662 Tech 1970;25.

[29] Melbourne WH. Comparison of measurements on the CAARC standard tall building model in simulated model wind flows. J Wind Eng Ind Aerodyn 1980;6:73–88.

[30] Braun AL, Awruch AM. Aerodynamic and aeroelastic analyses on the CAARC standard tall building model using numerical simulation. Comput Struct 2009;87:564–81.

[31] Franke J, Hellsten A, Schlünzen H, Carissimo B. Best Practice Guideline for the CFD Simulation of Flows in the Urban Environment. COST Action 732: Quality Assurance and Improvement of Microscale Meteorological Models (2007). Hamburg, Ger n.d.

[32] Dagnew A, Bitsuamlak GT. Computational evaluation of wind loads on buildings: a review. Wind Struct 2013;16:629–60.

[33] Engineering Sciences Data Unit (ESDU) . Characteristics of atmospheric turbulence near the ground. Part II: single point data for strong winds. 85320th ed. 2001.

[34] Murakami S. Overview of turbulence models applied in CWE–1997. J Wind Eng Ind Aerodyn 1998;74:1–24.

[35] Tominaga Y, Mochida A, Yoshie R, Kataoka H, Nozu T, Yoshikawa M, et al. AIJ guidelines for practical applications of CFD to pedestrian wind environment around buildings. J Wind Eng Ind Aerodyn 2008;96:1749–61.

[36] STAR CCM+ 2016.

[37] Smagorinsky J. General circulation experiments with the primitive equations. 1963.

[38] Germano M, Piomelli U, Moin P, Cabot WH. A dynamic subgrid-scale eddy viscosity model. Phys Fluids 1991;A 3(7):1760–1765.

[39] Zhou L, Haghighat F. Optimization of ventilation system design and operation in office environment, Part I: Methodology. Build Environ 2009;44:651–6.

[40] Ansary AM El, El Damatty A, Nassef AO. Optimum Shape and Design of Cooling Towers 2011;5:655–64.

[41] Goolberg DE. Genetic Algorithms in Search, Optimization, and Machine Learning. Addion Wesley 1989;1989:102.

[42] Davis L. Handbook of Genetic Algorithms, Van Nostrand Reinhold, New York, 1991. Search PubMed n.d.

[43] Michalewicz Z, Fogel DB. How to solve it: modern heuristics. Springer Science & Business Media; 2013.

Chapter 7

7 Conclusions and Recommendations

7.1 Summary

This thesis introduces a robust Aerodynamic Optimization Procedure (AOP) that combines Genetic Algorithm, Computational Fluid Dynamics and Artificial Neural Network model as a surrogate model for aerodynamic assessment of tall buildings. The proposed procedure is adopted to optimize different types of building mitigations including corner chamfering, helical twisting and through openings. A verification is carried out to ensure the conversion towards the optimal building shape by comparing the wind performance produced by the optimal and other near optimal building shapes. The AOP is adopted to conduct both single- and multi-objective optimization problems. Large Eddy Simulation (LES) models are utilized to accurately capture the atmospheric boundary layer wind flow interaction with tall buildings. Moreover, a new inflow generation technique called the Consistent Discrete Random Flow Generation (CDRFG) technique is developed for LES wind simulation. The accuracy of numerical wind load evaluation is assessed by comparing pressure distributions and building responses with results obtained from previous boundary layer wind tunnel (BLWT) tests and other numerical simulations. The technique is examined for a standalone tall building and for a tall building located in a realistic city center configuration.

7.2 Main Contributions

The main conclusions pertaining to the aerodynamic optimization procedure in chapters two, three and four:

- The adoption of ANN in objective function evaluation attained many advantages for the AOP, including (i) significantly lowering the computational cost, (ii) eliminating the need for the direct integration of CFD within the optimization process (i.e. CFD can be used offline to train the surrogate model), (iii) allowing the use of any available BLWT database in conjunction with the CFD database; and (iv) mapping a highly nonlinear relationship between the design variables and the objective function if trained properly

- Comparison of the aerodynamic behavior of the optimal building shape to the other near optimal ones using 3D LES of both 2D flow and ABL flows shows a similar trend. Thus, low-dimensional flow analyses can be sufficient to indicate the relative performance of the shapes with a more time-efficient analyses (i.e. around 150 times faster than ABL flow analyses).
- Three dimensional LES models of an atmospheric boundary layer flow are required to capture the aerodynamic improvement gained due to global mitigations such as building vents.
- Conducting multi-objective aerodynamic optimization problem provides a set of optimal solutions (Pareto Front), which will allow architects to involve adequacy and serviceability considerations in the selection of the outer shape of the building.
- The continuous flow information provided by LES enabled visual comparisons between the basic (unmitigated) building shape and the optimal ones.
- Local (corner) aerodynamic mitigation of tall buildings can result in significant reduction in both along- and across- wind loads, which results in reducing the overall building response, vibration and cost.
- Global aerodynamic mitigation by using helical twisting and vents introduction to a tall building are considered effective approaches in reducing base moments in

both orthogonal directions as a result of weakening the development of vortex shedding.

The main conclusions pertaining to the utilization of CDRFG inflow technique for standalone and surrounded configurations in chapters five and six:

- The employed LES model while using CDRFG technique to simulate the inflow field leads to more accurate estimation for the wind pressure distributions on a tall building and its responses. Since, this model supports parallel computation, it allows for a time-efficient evaluation of the building aerodynamic behavior.

- Wind induced pressure obtained from the current LES model for the isolated building configuration are in a very good agreement with the pressures measured in the BLWT. Mean and fluctuating pressures distributions obtained from the current LES model has a better agreement with the BLWT results compared to previous numerical models
- Base moment spectra and building responses obtained from the current LES model (for both isolated and complex surrounding configurations) well agree with the spectra and responses obtained from wind tunnel. Average difference between LES and WT responses is found to be less than 6% for both configurations.

7.3 Recommendations for future work

The current thesis discusses several topics related to aerodynamic optimization and wind load evaluation for tall buildings. For future research, the following investigations are suggested:

- Including location effect and meteorological data in the aerodynamic optimization procedure to account for different inflow characteristics for each wind direction.

- Considering the aeroelastic effect and building motion during extreme wind events, which expected to be critical for highly flexible structures.

- Extend the optimization process to include the structural elements and the dynamic properties of tall buildings leading to better utilization of the available resources and materials.

Appendices A

Building dynamic responses

Modal forces F_i can be calculated from the base moments M_i using Equation A1.

$$\begin{Bmatrix} F_x \\ F_y \\ F_\theta \end{Bmatrix} = \begin{bmatrix} 1/h & 0 & 0 \\ 0 & 1/h & 0 \\ 0 & 0 & 0.7 \end{bmatrix} . \begin{Bmatrix} M_y \\ M_x \\ M_t \end{Bmatrix}$$ **Equation A1**

where h is the building height

The rms displacement response in the generalized coordinate corresponding to a vibration mode i is calculated using the integral in Equation A2, where $\left|H_i^2\right|$ is called the mechanical admittance function and is expressed by Equation A3.

$$\mathring{x}_i^{\,*} = \int_0^\infty \left|H^2\right| . SF_i \, .df$$ **Equation A2**

$$\left|H_i^2\right| = \frac{1}{K_i^2\left(\left(1-\frac{f^2}{f_s^2}\right)^2 + 4\zeta^2\frac{f^2}{f_s^2}\right)}$$ **Equation A3**

where $\mathring{x}_i\,*$ is the rms generalized displacement; $\left|H_i^2\right|$ is the mechanical admittance function for the mode i; SF_i is the force spectra for mode i.

Mean, $\bar{x}_i^{\,*}$, background, $\mathring{x}_{i\,Bg}^{\,*}$, and resonant component, $\mathring{x}_{i\,res}$, of the generalized displacement are calculated using to Equation A4.

$$\bar{x}_i^{\,*} = \frac{\bar{F}_i}{K_i}, \; \mathring{x}_{i\,Bg}^{\,*} = \frac{\sigma_{Fi}}{K_i}, \; \mathring{x}_{i\,res} = \sqrt{\mathring{x}_i^{\,*2} - \mathring{x}_{i\,Bg}^{\;2}}$$ **Equation A4**

where σ_{Fi} is the rms modal force of the mode i

Peak displacement, $\hat{x}_{itop}$, and acceleration $\ddot{\hat{x}}_{itop}$ at the building top are calculated as function of the generalized displacement according to Equations A5.

Equation A5

$$\hat{x}_{itop} = \bar{x}_i^{\,*} + g_f \,\tilde{x}_i^{\,*}$$

$$\ddot{\hat{x}}_{itop} = g_f \,.\left(2\pi f_i\right)^2 .\tilde{x}_{i\,res}^{\,*}$$

Peak equivalent static base moments, $\hat{M}_{bi}$, are calculated from Equation A6, where $\bar{M}_{bi}$ is the mean base moment and $\tilde{M}_{bi}$ is the rms base moment which can be calculated using Equations A7, where g_f is the peak factor and it is taken here equal to 3.5.

Equation A6

$$\hat{M}_{bi} = \bar{M}_{bi} + g_f \,\tilde{M}_{bi}$$

Equation A7

$$\tilde{M}_{bi} = \left(2\pi f_i\right)^2 \frac{m}{3} H_s^{\,2} \tilde{x}_i^{\,*} \quad \text{(along and across wind)}$$

$$\tilde{M}_{b\theta} = \left(2\pi f_\theta\right)^2 \frac{I}{2} H_s \tilde{x}_\theta^{\,*} \quad \text{(torsional direction)}$$

where m, I are the mass and inertia per unit height which equals to $m_s.B_s.D_s$ and $m_s.B_s.D_s.(B_s^2+D_s^2)/12$, respectively.

Curriculum Vitae

Name:	Ahmed Elshaer
Post-secondary Education and Degrees:	Cairo University Giza, Egypt 2005-2010 B.Sc.
	Cairo University Giza, Egypt 2010-2013 M.Sc.
	The University of Western Ontario London, Ontario, Canada 2013-2017 Ph.D.
Honors and Awards:	Alan Davenport Award of Excellence, Boundary Layer Wind Tunnel Laboratory, Western University, Nov. 2016.
	Received the Queen Elizabeth II Graduate Scholarship in Science and Technology (OGS/QEII), May 2016.
	Alan G. Davenport Memorial Scholarship, Boundary Layer Wind Tunnel Laboratory, Western University, May 2016.
	Nominated for OGS (Ontario Graduate Scholarship), May 2015.
	Precast Concrete Institute (PCI) Contest Winner, 2014-2016.
	Egypt award of Excellence in Engineering, 2005-2010.
Related Work Experience	Research and Teaching Assistant The University of Western Ontario 2013-2017
	Assistant Lecturer and Research Assistant Cairo University Giza, Egypt 2011-2013

Publications:

Elshaer, A., Aboshosha, H., Bitsuamlak, G., El Damatty, A., Dagnew, A., 2016. LES evaluation for wind-induced responses of a tall building with isolated and surrounded configurations. *Engineering Structures*; 115, 179-195.

Aboshosha, H., Elshaer, A., Bitsuamlak, G., El Damatty, A., 2015. Consistent inflow turbulence generator for LES evaluation of wind-induced responses for tall buildings. *Journal of Wind Engineering and Industrial Aerodynamics*. 142, 198-216.

Elshaer, A., Mostafa, H., Salem, H., 2016. Progressive collapse assessment of multistory framed Reinforced concrete structures subjected to seismic actions According to UFC guidelines for alternative path method. *KSCE journal of civil engineering*; 21(1).

Elshaer, A., Bitsuamlak, G., El Damatty, A., Enhancing wind performance of tall buildings using corner aerodynamic optimization. *Engineering Structures; 136, 133-148.*

Elshaer, A., Bitsuamlak, G., El Damatty, A., 2016. Aerodynamic shape optimization of tall buildings using twisting and corner modifications. 8th International Colloquium on Bluff Body Aerodynamics and Applications, Boston, USA.

Elshaer, A., Bitsuamlak, G., El Damatty, A., 2016. Aerodynamic optimization to reduce wind loads on tall buildings, Canadian Society of Civil Engineers, London, Canada.

Elshaer, A., Aboshosha, H., Bitsuamlak, G., El Damatty, A., 2016. Numerical evaluation of wind loads on a tall building located in a city center, Canadian Society of Civil Engineers, London, Canada.

Hajra, B., Bitsuamlak, G., Aboshosha, H., Elshaer, A., 2016. Large eddy simulation of wind induced loads on a low rise building with complex roof geometry. Canadian Society of Civil Engineers, London, Canada.

Elshaer, A., Bitsuamlak, G., El Damatty, A., 2015. Aerodynamic shape optimization for corners of tall buildings using CFD. 14th International Conference on Wind Engineering. Porto Alegre, Brazil.

Elshaer, A., Bitsuamlak, G., El Damatty, A., 2015. Vibration control of tall buildings using aerodynamic optimization. 25th Canadian Congress of Applied Mechanics. London, ON, Canada.

Elshaer, A., Bitsuamlak, G., El Damatty, A., 2014. Wind Load Reductions due to Building Corner Modifications. In: proceeding of 22nd Annual Conference of the CFD society of Canada. Toronto, ON, Canada.